A Coherence Function Approach to Image Simulation

Vom Fachbereich Physik
der Technischen Universität Darmstadt

zur Erlangung des Grades
eines Doktors der Naturwissenschaften
(Dr. rer. nat.)

genehmigte

Dissertation

von

Dipl.–Phys. Heiko Müller

aus Kassel

Referent: Prof. Dr. H. Rose
Korreferent: Prof. Dr. H. Wipf

Tag der Einreichung: 18. April 2000
Tag der Prüfung: 07. Juni 2000

Darmstadt 2000
D 17

Preface

This thesis originates from the participation at a joint research project of several universities and institutes concerned with ‘Quantitative high–resolution electron microscopy in the materials sciences’. Within this framework we have investigated the possibility to extent the theory of image simulation in electron microscopy to inelastic electron scattering.

This generalization necessitates a sufficiently accurate characterization of the partially coherent conditions which govern the image formation with inelastically scattered electrons. As a result of our work we have implemented an appropriate generalization of the conventional multislice method. The resulting software package is termed YaMS (**Y**et **a**nother **M**ulti**S**lice) and accounts for thermal diffuse scattering and inelastic scattering due to electronic excitations and partially coherent illumination. The software can be used for the calculation of TEM, STEM and CBED images and diffraction patterns for periodic and non–periodic specimens. It has already been applied to imaging problems in the materials sciences and in structural biology. The new method is based on the propagation of the mutual coherence function of the wave field of the imaging electrons.

For a detailed description of the software implementation of the coherence function multislice method we must refer the reader to the YaMS manual [1].

Contents

Chapter 1

Introduction

The propagation of electrons is governed by the Schrödinger wave equation. Owing to this wave property the scattering of electrons differs appreciably from that of classical solid particles. Specifically the interference between different partial waves affects the intensity distribution of an electron micrograph and prevents a straightforward interpretation in many cases. Without such an interference the formation of an image would not be possible. The description of image formation in an electron microscope must, therefore, account for the possibility of interference which is determined by the degree of coherence of the electron wave field. Interference effects must be considered in order to correctly extract the information about the spatial structure of an object from the image. The image intensity depends on the partial coherence of the electron wave field. This partial coherence is caused by the finite energy width and the extension of the effective electron source, by parasitic incoherent perturbations, and by unavoidable inelastic scattering processes within the object. Inelastic scattering generally decreases the degree of coherence. Even for energy–filtered high–resolution imaging inelastic scattering effects are important, because electrons which have suffered a very small energy loss cannot be separated from the unscattered or elastically scattered electrons by a conventional energy filter [2]. Thermal diffuse scattering, for example, produces very small energy losses below 0.1 eV and contributes appreciably to the intensity for high scattering angles [3].

The interaction of the imaging electrons with the atoms of the object has to be described in terms of quantum theory [4, 5, 6]. Due to the quantum nature of the interaction process, we must distinguish carefully between elastic scattering and inelastic scattering. For elastic scattering the quantum state of the object remains unchanged. In this case it suffices to assume a static scattering potential without any internal degrees of freedom. The state of the object is changed in the case of an inelastic scattering process. This change is accompanied by a transfer of energy between the scattered electron and the object. In the case of phonon excitation the amount of transferred energy is very small.

The intensity recorded by an electron micrograph does not directly represent the object. The signal produced by the scattered electrons on the detector does not yield any information about the final object state after the scattering process. This fact has severe consequences for the theory of image formation with elastically and inelastically scattered electrons. The different energy eigenstates of the object are mutually orthogonal. Hence partial waves belonging to scattering processes resulting in different final object states cannot interfere with each other. They contribute to the image signal in an incoherent manner. This incoherence is due to the change of the object state and not due to different energy losses of the scattered electrons. In the presence of degenerated final object states inelastic scattering processes with the same energy losses may result in different object eigenstates. Since it is always possible to choose an orthogonal basis of the multi–dimensional subspace of the final eigenfunctions the corresponding partial waves of the scattered electron must be considered incoherent [7]. The situation becomes much more involved in the case of multiple scattering. The plane partial waves of an inelastically scattered electron, which has excited a distinct object transition, are mutually coherent and can interfere with each other after subsequent elastic scattering. This mechanism shows that the inelastically scattered wave contains high–resolution spatial information about the object [8, 9, 10].

The interaction between electrons and matter is rather strong due to the intense Coulomb interaction. This causes some well established approximation methods, like the first–order Born approximation or even the phase object approximation, to fail in most cases for electron imaging [11]. With a few exceptions, e.g. thin amorphous foils consisting of light elements such as biological specimens, electron imaging is dominated by plural scattering events. Owing to these dynamical effects the theoretical treatment of electron scattering is more involved than that of x–ray or neutron scattering. On the other hand, the strong sensitivity of electrons to the electric fields of the atoms makes electron scattering a powerful high–resolution imaging method [12, 13]. These advantages become even more important if we consider the possibilities of energy–resolved analytical electron microscopy [2].

The direct interpretation of high–resolution electron micrographs is a very difficult task and can occasionally lead to erroneous conclusions about the atomic structure of the object. This happens since in an electron microscope the recorded intensity does not directly represent the structure of the object owing to the non–linear characteristic of the electron–specimen interaction and of the image formation. Hence the simulation of electron micrographs has proven a valuable tool for image interpretation and structure determination in the materials sciences and in structural biology. Such calculations enable a reliable interpretation of electron micrographs providing nearly atomic resolution. Additionally, image simulation helps to determine optimal imaging conditions and to assess the potentials of novel instruments and imaging techniques.

A number of different methods have been proposed to calculate the propagation of the incident electron wave through the object. For periodic objects with small unit cells

the Bloch wave method [14, 15, 16] provides very exact predictions for the contribution of the elastically scattered electrons to the image and to the diffraction pattern. Unfortunately, most objects like interface structures, grain boundaries, dislocations, or ice–embedded macromolecules are non–periodic. For these objects the multislice method, invented by Cowley and Moody [17], is much better suited. From a mathematical point of view this very general approach to image simulation is a famous application of Trotter's product formula method [18] for the solution of parabolic partial differential equations. A very similar technique has been used by Feynman for the foundation of his path integral approach to non–relativistic quantum theory [19].

During the last 15 years different software implementations of the multislice method have been published and applied to many practical problems in electron microscopy. The software packages EMS by Stadelman [20], NCEMSS by O'Keefe and Kilaas [21], and TEMSIM by Kirkland [11] are widely used in the electron microscopical community. The underlying physical theory and mathematical methods of all these implementations are very similar and, accordingly, they provide almost equivalent results.

The conventional theory of image formation assumes completely coherent imaging conditions. The image simulation packages mentioned above provide the possibility to account approximately for partial coherent illumination by the transmission cross coefficient introduced by Ishizuka [22]. The scattering process itself is treated completely coherent. Only in the ideal and unrealistic case of coherent illumination and purely elastic scattering the representation of the imaging electron by a stationary wave function is possible. Nevertheless, the conventional multislice method uses this approach for the calculation of images and diffraction patterns of realistic objects. Hence, the results can only be considered as correct as long as the influence of inelastic interaction between the imaging electrons and the object is neglected. Unfortunately, this approximation is only reasonable for very thin objects within the frame of validity of the linear theory of image formation. Since the resolution of modern electron microscopes will improve considerably during the next years owing to the use of electron optical correctors and monochromators [23, 24] a reinvestigation of the general problem of image simulation is required. Additionally, it is expected that a more quantitative interpretation of electron micrographs will gain importance. The term Quantitative High–Resolution Electron Microscopy (QHREM) has already been invented [25]. Especially this quantification will require a more accurate theory of image simulation accounting correctly for inelastic scattering and partial coherence.

It will be shown that a reformulation of the theory of image formation with inelastically scattered electrons in the electron microscope, pioneered by Rose [26], employing the mutual coherence function is possible. This approach is motivated by the investigations of Rose [8] and Kohl and Rose [7]. From a theoretical point of view the optical theorem of quantum mechanical scattering theory provides much insight into the fundamental principles of image formation in the electron microscope. This theorem illustrates

how inelastic scattering influences the signal recorded by an electron detector in a real microscope.

After discussing some fundamental principles of elastic and inelastic electron scattering in chapter 2, we will investigate the relation between the validity of the optical theorem and the conservation of the probability current in electron microscopy. Even in the case of inelastic scattering a generalized version of the optical theorem is a direct consequence of the particle conservation during the scattering process. This conservation theorem has the effect that the second–order Born approximation of the elastic scattering amplitude is influenced by the inelastic scattering processes. It will become evident that any image simulation procedure, which accounts for the mutual interference between the scattered partial waves, for partial coherence, and for inelastic scattering should fulfill the generalized optical theorem in order to provide a consistent approximation of the process of image formation in electron microscopy. Unfortunately, this is not the case for the conventional multislice method with an absorption potential widely used for the calculation of electron micrographs. In a review article by van Dyck, the incorporation of the inelastic scattering contribution into the multislice method has been termed one of the open problems of the theory of HREM image simulation [27]. Because of the validity of the generalized optical theorem this problem cannot be solved by the introduction of an absorption potential which separates the inelastically scattered electrons from the elastically scattered electrons, not even for zero–loss filtered images because of the unavoidable influence of thermal diffuse scattering.

To resolve this deficiency an image simulation method based on the mutual coherence function of the electron wave field is proposed. The mutual coherence function is well known in light optics and was first introduced into electron optics by Hawkes [28] and Rose [26]. The coherence function approach to image simulation does fulfill the optical theorem and, therefore, provides a consistent approximation of the scattering and imaging process for arbitrary objects under partially coherent illumination conditions. The coherence function method will be discussed in chapter 4. This will show that the propagation of the mutual coherence function through the object can be described by the mutual object spectrum in Fourier space or equivalently by the mutual object transparency in real space. Both functions are completely determined by the scattering amplitudes of the object with respect to all possible object excitations. The quadratic part of the mutual object spectrum is related to the mixed dynamic form factor in first–order Born approximation. The mixed dynamic form factor has been used successfully by Kohl and Rose [7] to describe imaging with inelastically scattered electrons for sufficiently thin objects. The mutual object spectrum extends this method to the imaging of thick objects, where the first–order Born approximation can no longer be applied.

Unfortunately, it is not possible to calculate the mutual object transparency for any realistic object explicitely. Nevertheless, within the frame of validity of Glauber's high–energy approximation [6] an approximation of the mutual object transparency can be

obtained. This was first done by Rose in the case of thin objects [8]. This approach will be extended in chapter 5 to more realistic objects and an iterative representation of the mutual object transparency for thick objects, where dynamical scattering effects become important, will be derived. The resulting method is called the coherence function multislice method because it resembles the principle of the conventional multislice method. However, the coherence function multislice does not violate the optical theorem as the conventional multislice method does if inelastic scattering and partial coherence are taken into account.

The most striking difference between the conventional multislice method and the coherence function approach is that the new method intrinsically depends on four spatial coordinates whereas the conventional multislice method is two–dimensional. It will be shown that no trivial decomposition of the mutual object transparency into a product of two mutually independent factors exists. This important fact has already been pointed out by Kohl and Rose [7].

The numerical evaluation of the coherence function method necessitates further approximations. We discuss a non–trivial decomposition of the mutual object transparency in chapter 5. By means of this method the unduly large numerical expenditure of the four–dimensional formalism can be reduced to a two–dimensional method well suited for practical computations. The key idea behind this considerable simplification is the fact that any hermitian function can be decomposed into a sum of mutually independent product terms.

To describe the process of image formation in electron imaging the simulation has to consider the influence of the illumination system and of the imaging system of the electron microscope. This ensures that the information limit of the microscope is taken into account correctly. Both the illumination system and the imaging system can be considered by the coherence function multislice method easily, as it is outlined in chapter 5. Finally, the feasibility of the coherence function approach is demonstrated by some numerical examples and by a comparison of the simulations with experimentally obtained diffraction patterns.

Chapter 2

Fundamentals of electron scattering

A quantum–mechanical system is associated with a complex–valued wave function Ψ depending on all internal degrees of freedom of the isolated system and on time. This wave function is called the probability amplitude of the system because the probability density to find the system in a certain state at a given time is the square of the absolute value of the corresponding probability amplitude. The time evolution of this wave function is governed by the Schrödinger equation

$$i\hbar\,\partial_t\,\Psi = \hat{\mathbf{H}}\,\Psi\ . \tag{2.1}$$

The self–adjoint differential operator $\hat{\mathbf{H}}$ on the right–hand side of equation (2.1) is the Hamilton operator of the entire system. Hence the Hamiltonian considers the scattered electron and all atoms of the specimen. The total wave function $\Psi = \Psi(\mathbf{r}, \mathbf{R}, t)$ depends on the position of the scattered electron $\mathbf{r}$ and on all internal degrees of freedom $\mathbf{R}$ of the object. Here the multidimensional vector $\mathbf{R} = (\mathbf{R}_0, \ldots, \mathbf{R}_l)^t$ comprises the positions $\mathbf{R}_i$, $i = 0, \ldots, l$, of all constituent particles of the object. Since the object state may change during the scattering process, we cannot rewrite the total wave function Ψ as a simple product of an object wave function and an electron wave function. This behaviour is an important property of interacting quantum systems. The Hamiltonian of the entire system adopts the form

$$\hat{\mathbf{H}} = \hat{\mathbf{H}}_E + \hat{\mathbf{H}}_O + W(\mathbf{r}, \mathbf{R})\ . \tag{2.2}$$

In this equation the operators $\hat{\mathbf{H}}_E$ and $\hat{\mathbf{H}}_O$ denote the Hamiltonians of the scattered electron and of the object, respectively. The interaction between the incident electron and the object is governed by the interaction potential $W = W(\mathbf{r}, \mathbf{R})$. The Hamiltonian of the object acts only on the coordinates of the vector $\mathbf{R}$, whereas the Hamiltonian of the electron acts solely on the position vector $\mathbf{r}$. Nevertheless, equation (2.1) does not separate with respect to the coordinates of the object and the scattered electron because the interaction potential depends on $\mathbf{r}$ and $\mathbf{R}$ simultaneously. Although inelastic interaction is taken into account and the object state may be altered during the

scattering process, the total Hamiltonian (2.2) of the system does not depend on time. Accordingly, the Schrödinger equation can be separated with respect to space and time by means of the Bernoulli product ansatz.

2.1 Relativistic kinematics

The relativistic energy conservation connects the momentum $\mathbf{p}$ of the electron with the acceleration voltage U via the relations

$$(\gamma - 1)\ mc^2 = eU\ , \quad \gamma^2 = 1 + \frac{\mathbf{p}^2}{m^2c^2}\ , \tag{2.3}$$

where c is the velocity of light, m the rest mass, and e the charge of an electron, respectively. This gauge of the electric potential assumes that the accelerated electron is initially at rest at the tip of the cathode. To account for the finite energy width of a real electron gun we must consider an ensemble of electrons accelerated by slightly different acceleration voltages.

By employing the expression (2.3) together with the de Broglie relation, we obtain

$$p = \hbar k = \frac{h}{\lambda} = \sqrt{2emU\ \left(1 + \frac{eU}{2mc^2}\right)}\ . \tag{2.4}$$

Hence the electron wave length λ is determined by the acceleration voltage. In transmission electron microscopy the acceleration voltage U is in the range of 100 kV to 1.2 MV. Therefore, the wave length of the electron is shorter than 3.70 pm. This relativistically corrected result differs from the non–relativistic value by about 4.8 percent. In the laboratory system the mass of the electron seems to be increased by about 19.6 percent for an acceleration voltage of $U = 100$ kV. In order to provide atomic resolution, uncorrected electron microscopes must operate at high–voltages of about 1.2 MV because of the large aberrations of charged particle lenses. With modern transmission microscopes equipped with a corrector which compensates for the spherical aberration of the objective lens [23] atomic resolution can be obtained even with voltages between 200 and 300 kV. For the acceleration voltage $U = 1.2$ MV the relativistic correction of the wave length is approximately 47 percent and the mass of the accelerated electron is about 3.3 times higher than its rest mass. This result demonstrates that relativistic kinematics must be considered in electron imaging theory for high acceleration voltages. In figure 2.1 the fundamental kinematical relations for relativistic electrons are plotted. The wave length falls off rapidly for moderate acceleration voltages and approaches the Compton wave length $\lambda_C = h/mc \approx 2.43$ pm at about $U_C = 212$ kV. For energies $eU > mc^2$ the wave length is approximately inversely proportional to the acceleration voltage.

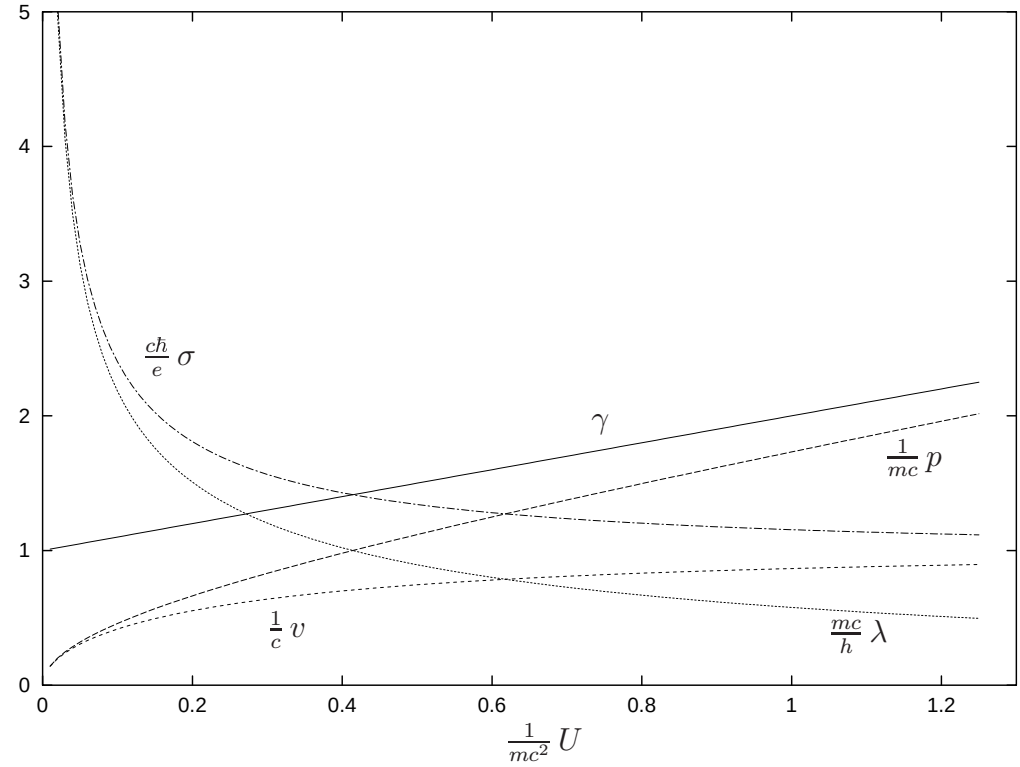

Figure 2.1: *Relativistic kinematics of an accelerated electron. The relativistic mass increase γ, the momentum p, the velocity v, and the wave length λ are appropriately normalized and plotted versus the normalized acceleration voltage U/mc^2. Additionally the normalized interaction constant σ_i governing the interaction between the electron and the object potential is shown.*

In free space the propagation of the electron wave function is rather simple. In the absence of an electromagnetic field the Schrödinger equation (2.1) reduces to

$$i\hbar\,\partial_t\,\psi = -\frac{\hbar^2}{2m}\,\Delta\,\psi\;. \tag{2.5}$$

The simplest possible solution for a single quantum–mechanical particle fulfilling this equation is a plane wave

$$\psi(\mathbf{r},t) = \exp i(\mathbf{kr} - \omega t) \tag{2.6}$$

propagating in the direction $\mathbf{k}/k$. To account correctly for the relativistic behaviour of the high–energy electrons we have to employ the relativistically corrected dispersion relation

$$\frac{\hbar^2\mathbf{k}^2}{2m} = \hbar\omega\left(1 + \frac{\hbar\omega}{2mc^2}\right)\;. \tag{2.7}$$

This equation relates the relativistically modified beam energy [29]

$$eU^* = eU\left(1 + \frac{eU}{2mc^2}\right) \tag{2.8}$$

to the momentum or, equivalently, to the wave vector $\mathbf{k}$ of the corresponding plane wave. As long as the spin of the scattered electron and the magnetic interaction between the scattered electron and the object are neglected the calculations based on the Schrödinger equation with the modified dispersion relation (2.7) yield correct results even in presence of an object. In this case the electric interaction potential $\varphi_O = \varphi_O(\mathbf{r})$ must be multiplied by an additional factor $\gamma = 1 + \frac{eU}{mc^2}$ in order to account for the reduced velocity of the electrons due to the relativistic increase of the electron mass. In appendix A this procedure will be justified more rigorously.

Generally the form of the electron wave is affected by the microscopic electric fields of the object's atoms

$$\Psi = \Psi(\mathbf{r}, \mathbf{R}) \exp(-i\frac{Et}{\hbar}) \tag{2.9}$$

but the time dependent exponential factor is retained in the general solution. Then E denotes the total energy of the entire system. The factorization in equation (2.9) results from the time independence of the Hamiltonian (2.2) of the total system. As a consequence the total energy of the system

$$E = E_0 + mc^2\sqrt{1 + \frac{\hbar^2 k_0^2}{m^2c^2}} = E_n + mc^2\sqrt{1 + \frac{\hbar^2 k_n^2}{m^2c^2}}\,, \tag{2.10}$$

for $n = 0, 1, \ldots$, is conserved. Here E_0 and E_n denote the energy of the object before and after the scattering process, respectively. Accordingly, k_0 and k_n are the corresponding wave numbers of the interacting electron in front of and behind the object. For elastic scattering the object remains in the initial state. Since in this case no energy is transfered, we find from equation (2.10) that the wave number does not change as long as we only consider the final and initial states of the scattering process.

2.2 Scattering equation

Within the range of the object potential the kinetic energy of an elastically scattered electron is not conserved. Only the sum of the potential energy and of the kinetic energy is constant and in presence of electromagnetic fields the wave vector of the electron becomes a function of its position. Therefore, the electron wave suffers an additional phase shift after traveling a short distance through the object. For weak potentials this phase shift is proportional to the strength of the object potential integrated along the trajectory of the electron. Given that the electric potential of the object

$\varphi_O = \varphi_O(\mathbf{r})$ is small compared to the kinetic energy of the incident electron, we can expand the momentum–energy relation (2.4) in a Taylor series with respect to a small deviation of the kinetic energy. This yields the first–order relation

$$\frac{1}{\lambda(U+\varphi_O)} = \frac{1}{\lambda(U)} + \sigma_i \varphi_O + \dots \;, \quad \sigma_i = \frac{1}{U\lambda(U)} \frac{1+\frac{eU}{mc^2}}{2+\frac{eU}{mc^2}} \;. \tag{2.11}$$

The interaction constant σ_i is a useful measure of the strength of the elastic interaction between the imaging electrons and the object. Figure 2.1 shows the dependence of the interaction constant on the acceleration voltage. The interaction constant decreases rapidly for moderate acceleration voltages and it is nearly constant for energies above the Compton limit. The divergence for very small acceleration voltages has no physical meaning because then the first–order approximation (2.11) is not valid anymore.

To further develop the quantum theory of elastic and inelastic scattering we assume that the dynamics of the object are completely understood. The analysis of the possible quantum states of an object consisting of many atoms is a very demanding task of solid state physics especially if bulk matter effects have to be included into the calculations [30]. For most purposes it suffices to employ simple quantum–mechanical models of the object dynamics which approximately account for the possible object transitions. We employ the set $\phi_n = \phi_n(\mathbf{R})$, $n = 0, 1, \dots$ of object eigenfunctions which satisfy the Schrödinger equation for the isolated object

$$\hat{\mathbf{H}}_O \, \phi_n = E_n \, \phi_n \;. \tag{2.12}$$

These eigenfunctions are mutually orthogonal and, moreover, satisfy the completeness relation

$$\int \phi_m^*(\mathbf{R}) \, \phi_n(\mathbf{R}) \, d^l\mathbf{R} = \delta_{mn} \;, \quad m, n = 0, 1, \dots \;, \tag{2.13}$$

where the integration extends over the total configuration space of the object and δ_{mn} denotes the Kronecker symbol. This property allows us to expand the spatial part of the wave function $\Psi = \Psi(\mathbf{r}, \mathbf{R})$ in a series with respect to the eigenstates of the object

$$\Psi(\mathbf{r}, \mathbf{R}) = \sum_{n=0}^{\infty} \psi_n(\mathbf{r}) \phi_n(\mathbf{R}) \;. \tag{2.14}$$

The coefficients $\psi_n(\mathbf{r})$, $n = 0, 1, \dots$, describe the projections of the total wave function $\Psi(\mathbf{r})$ onto the eigenstates of the object. The influence of the object on the scattered electron is completely described by the matrix elements

$$U_{nm}(\mathbf{r}) = \frac{2m\gamma}{\hbar^2} \int \phi_n^*(\mathbf{R}) \, W(\mathbf{r}, \mathbf{R}) \, \phi_m(\mathbf{R}) \, d^l\mathbf{R} \tag{2.15}$$

of the interaction potential. These matrix elements only depend on the position vector of the scattered electron and the factor γ accounts for the relativistic correction of the scattering potential discussed in appendix A.

For reasons of simplicity we assume that the object is in the ground state ϕ_0 prior to the scattering process. Moreover, we approximate the incident wave by a plane wave. The total initial wave function has the form

$$\Psi_i(\mathbf{r}, \mathbf{R}, t) = \exp(i\mathbf{k}_0\mathbf{r})\ \phi_0(\mathbf{R})\ \exp\left(-i\frac{Et}{\hbar}\right)\ . \tag{2.16}$$

The scattering process may excite the object from its ground state ϕ_0 to a certain excited state ϕ_n or, as in the case of elastic scattering, leave the object state unchanged. Each final state satisfies the Schrödinger equation (2.1) with the Hamiltonian (2.2). In general the final wave function of the scattered electron will be a superposition of partial waves $\psi_m = \psi_m(\mathbf{r})$, $m = 0, 1, \ldots$, belonging to different final object states. To find the differential equation for each final object state we substitute the expansion (2.14) into the Schrödinger equation (2.1), multiply with all different eigenfunctions ϕ_m, and integrate over the space of configuration of the object. By employing the relations (2.2), (2.12) and (2.13), we eventually obtain the set of equations [31]

$$\left\{\Delta + \mathbf{k}_n^2\right\}\ \psi_n = \sum_{m=0}^{\infty} U_{nm}\ \psi_m\ , \quad n = 0, 1, \ldots\ . \tag{2.17}$$

The indices m and n enumerate the eigenstates of the object. The matrix elements U_{mn} measure the probability amplitude for a transition of the object from state ϕ_m to state ϕ_n. This probability depends only on the internal structure of the object.

The choice of the initial object state is arbitrary. It may differ from the ground state. Equation (2.17) also describes the scattering at any excited state ϕ_n, $n \neq 0$, because its derivation does not depend on the special choice made in (2.16) for the initial object state. For a system in thermal equilibrium we do not know the initial object state precisely but we know the probability P_m that the object initially is in state ϕ_m with the energy eigenvalue E_m. Since the set of object states is complete, the relation

$$\sum_{n=0}^{\infty} P_m = 1 \tag{2.18}$$

holds true. In order to determine the probabilities P_m, we assume that the object is in thermal contact with a heat reservoir with temperature T_H. In this case the specimen is a subsystem of a much bigger system. Since the energy of the object fluctuates, the probability to find the system in the m–th state is proportional to the Boltzmann factor

$$P_m = \frac{1}{Z}\ \exp\left(-\frac{E_m}{k_B T_H}\right)\ , \quad Z = \sum_{n=0}^{\infty} \exp\left(-\frac{E_n}{k_B T_H}\right)\ . \tag{2.19}$$

Here k_B denotes Boltzmann's constant and Z is the canonical partition sum. This probability distribution can be used to describe the image formation in electron microscopy

with a sufficient degree of accuracy as long as object heating and object damage are negligibly small. A system that can be characterized appropriately by time independent probabilities P_m is called a stationary system. Since each scattering process is connected to a real or virtual fluctuation of the object state, the state of the object is not static. Nevertheless, it can be considered as stationary during the time of observation.

2.3 Lippmann–Schwinger equation

The system of coupled partial differential equations (2.17) describes elastic and inelastic scattering. The case of purely elastic scattering is obtained if the interaction potential $W(\mathbf{r}, \mathbf{R})$ depends only on $\mathbf{r}$. Then the interaction matrix (2.15) is diagonal $U_{mn} = 0$ for $m \neq n$. In the case of a distinct initial state (2.16) the system (2.17) reduces to the single equation

$$\left\{\Delta + \mathbf{k}_0^2\right\}\ \psi_0 = \psi_0\ U_{00}(\mathbf{r})\ . \tag{2.20}$$

This is the well known Schrödinger equation for scattering at a static potential $U = U_{00}$. It can be transformed into an integral equation if we employ the free–space Green function

$$G(\mathbf{r}, \mathbf{r}') = -\frac{1}{4\pi}\ \frac{\exp\left(ik_0|\mathbf{r} - \mathbf{r}'|\right)}{|\mathbf{r} - \mathbf{r}'|}\ , \tag{2.21}$$

which represents the solution of equation (2.20) for a point scatterer located at $\mathbf{r}' \neq \mathbf{r}$. The resulting integral equation for the wave function of the scattered electron

$$\psi(\mathbf{r}) = \exp\left(i\mathbf{k}_0\mathbf{r}\right) - \frac{1}{4\pi}\int U_{00}(\mathbf{r}')\ \psi(\mathbf{r}')\ \frac{\exp\left(ik|\mathbf{r}' - \mathbf{r}|\right)}{|\mathbf{r}' - \mathbf{r}|}d^3\mathbf{r}' \tag{2.22}$$

is known as the Lippmann–Schwinger integral equation [32].

This equation can be generalized in order to consider inelastic scattering processes as well. By applying the Green function approach (2.21) to each of the differential equations (2.17), we find

$$\psi_n(\mathbf{r}) = \exp\left(i\mathbf{k}_0\mathbf{r}\right)\ \delta_{n0} - \frac{1}{4\pi}\sum_{m=0}^{\infty}\int \psi_m(\mathbf{r}')\ U_{nm}(\mathbf{r}')\ \frac{\exp\left(ik_n|\mathbf{r}' - \mathbf{r}|\right)}{|\mathbf{r}' - \mathbf{r}|}d^3\mathbf{r}'\ ,$$

where we have assumed that the object is initially in the state ϕ_0. The set of coupled integral equations (2.3) together with the expansion of the total wave function (2.14) completely describe both elastic and inelastic scattering of an electron by an arbitrary object.

Chapter 3

Properties of the scattering amplitude

To describe image formation in an electron microscope we have to know the scattered electron wave at a great distance from the object. If the distance is large compared with the size of the imaged object the electron wave can be written as a superposition of spherical waves modulated by complex–valued scattering amplitudes

$$\Psi(\mathbf{r},\mathbf{R}) = \exp(i\mathbf{k}_i\mathbf{r})\ \phi_0(\mathbf{R}) + \sum_{n=0}^{\infty} f_{n0}(\mathbf{k}_n,\mathbf{k}_i)\frac{\exp(ik_nr)}{r}\ \phi_n(\mathbf{R})\ , \quad |\mathbf{k}_i| = k_0\ , \tag{3.1}$$

where a distinct scattering amplitude $f_{n0}(\mathbf{k}_n,\mathbf{k}_i)$ corresponds to each final object state ϕ_n. The scattering amplitude depends on the initial and final object state and on the directions $\mathbf{k}_i/k_0$ and $\mathbf{k}_n/k_n$ of the incident and of the scattered electron, respectively. Hence the scattering characteristic depends on the energy loss and on the type of the corresponding object excitation.

The scattering amplitudes are connected with the matrix elements of the corresponding scattering processes via the relation

$$f_{n0}(\mathbf{k}_n,\mathbf{k}_i) = -\frac{1}{4\pi}\sum_{m=0}^{\infty}\int U_{nm}(\mathbf{r}')\exp\left(-i\mathbf{k}_n\mathbf{r}'\right)\psi_m(\mathbf{r}')d^3\mathbf{r}'\ . \tag{3.2}$$

To derive this representation from the Lippmann–Schwinger integral equation (2.3) we employ the asymptotic approximation for the spherical wave

$$\frac{\exp\left(ik_n\left|\mathbf{r}-\mathbf{r}'\right|\right)}{\left|\mathbf{r}-\mathbf{r}'\right|} \approx \frac{\exp\left(ik_nr\right)}{r}\ \exp\left(-ik_n\frac{\mathbf{r}\cdot\mathbf{r}'}{r}\right) \tag{3.3}$$

far away from the scatterer located at $\mathbf{r}'$. Substituting this approximation into (2.3) and comparing the result with the definition of the scattering amplitudes (3.1) yields the relation (3.2) stated above. If the scattering potential vanishes outside an area with

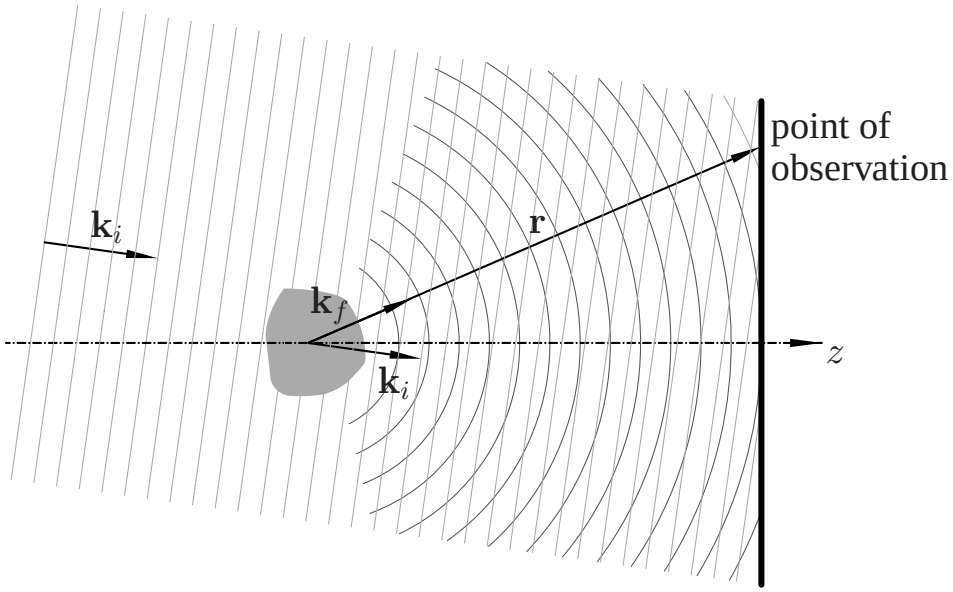

Figure 3.1: *Schematic illustration of the definition of the scattering amplitude* $f = f(\mathbf{k}_f, \mathbf{k}_i)$. *The origin of the coordinate system coincides with the center of the object region. The incident plane wave propagates in the direction* $\mathbf{k}_i$ *and the final wave vector* $\mathbf{k}_f$ *is defined by the position vector* $\mathbf{r}$ *of the point of observation at a great distance from the object. The angle enclosed by* $\mathbf{k}_i$ *and* $\mathbf{k}_f$ *is called the scattering angle.*

diameter a around the origin of the coordinate system the approximation (3.3) is valid for $r \gg a^2/\lambda$. This region is called the Fraunhofer domain [33].

The set of equations (3.2) leads to an implicit representation of the elastic and the inelastic scattering amplitudes because the scattered partial waves reappear on the right hand side of each equation. Therefore, the scattering problem must already be solved in order to evaluate the integral expressions of the scattering amplitudes. Fortunately, equation (3.2) shows that each scattering amplitude depends only on the wave function in the close vicinity of the object, where the matrix elements of interaction $U_{mn} = U_{mn}(\mathbf{r})$ are non–vanishing. Owing to this particular property the scattering amplitudes can be calculated efficiently by iteration methods.

In standard scattering experiments only the modulus of the scattering amplitude is measured and the phase information of the scattered wave is completely lost. Electron microscopy, however, utilizes this phase information because the image is an interference pattern formed by the unscattered and the scattered partial waves. Therefore, it is possible to gain high–resolution spatial information about the internal structure of the object by electron microscopical techniques. Unfortunately, the relation between the object potential and the scattering amplitude is highly non–linear for most objects. This complication poses a serious obstacle for direct structure retrieval by means of electron microscopy.

In mathematical terms a scattering experiment corresponds to a map of a given object potential $V = V(\mathbf{r})$ onto a scattering amplitude $f(\mathbf{k}_f, \mathbf{k}_i)$ as far as only elastic scattering is considered. As long as we only know the scattering amplitude for one k value the mapping is not unambiguously invertible. The scattering amplitude is complex–valued and depends on two directions in physical space, whereas the scattering potential is a real function of a three–dimensional vector. The functions f admissible as scattering amplitudes constitute an extremely restricted subset of all possible complex–valued functions of the form $f = f(\mathbf{k}_f, \mathbf{k}_i)$. The data contained in the scattering amplitude, hence, must be highly redundant. Therefore, it is obvious that no simple approach to the inverse scattering problem exists. In the short wave length limit $k \to \infty$ the object potential can be determined unambiguously by the scattering amplitude. Unfortunately, this result has no practical relevance, because we cannot measure the scattering amplitude in the short wave length limit, where all information is contained in the forward scattering direction even if the object would remain undamaged. Although the potential is uniquely determined by the short wave length limit of the scattering amplitude, the result obtained by solving the inverse scattering problem is very sensitive to small errors in the data very close to the forward scattering direction where all information is contained. This difficulty illustrates the intricate problems that show up if one tries to retrieve the structure of the imaged object by applying inverse scattering procedures [34].

The scattering amplitude satisfies distinct symmetry relations even if the object potential possesses no internal symmetries. In light optics the reciprocity relation for the scattering amplitude states that the position of the light source and the detector are interchangeable in a diffraction experiment. Let us assume a light amplitude $u(S)$ at the source point S and a light amplitude $u(P)$ at the image point P. If we put a source at position P and measure the resulting amplitude at position S then according to the reciprocity theorem of light optics the light amplitude will be $u(P)$ [35]. This reciprocity also holds for elastic electron scattering which implies that the roles of the incident and the scattered electron can be interchanged without altering the scattering amplitude of the static scattering potential.

$$f_{mm}(\mathbf{k}_f, \mathbf{k}_i) = f_{mm}(-\mathbf{k}_i, -\mathbf{k}_f) \ , \quad m = 0, 1, \dots \ . \tag{3.4}$$

To apply the reciprocity for inelastic scattering we must consider that the interchange of the initial and final scattering state does not only refer to the direction and wave number of the scattered electron but also to the initial and final state of the object. During an inelastic scattering process the object state is changed from Φ_m to Φ_n with an energy $E_{nm} = E_n - E_m$ transferred from the electron to the object. The reciprocal scattering event changes the state of the object back from Φ_n to Φ_m and the energy difference E_{mn} is transferred in the opposite direction from the object to the electron. Hence for electrostatic interaction the generalized reciprocity relation

$$f_{nm}(\mathbf{k}_n, \mathbf{k}_m) = f_{mn}(-\mathbf{k}_m, -\mathbf{k}_n) \tag{3.5}$$

is valid for elastic and inelastic scattering [4, 7]. This relation reveals that the meaning of reciprocity becomes only slightly more involved if inelastic scattering is taken into account. For the reversed scattering process the object must be prepared initially into a specific excited state. This state must be identical with the final object state of the initial scattering process. Although this situation can hardly be achieved in an experiment, for a stationary object in thermal equilibrium it is of practical importance. In this case all possible excitation processes happen with a certain probability during the time of exposure. Hence the situation becomes approximately symmetric again due to the thermal average. Therefore, also in the case of inelastic scattering the reciprocity theorem is very useful.

3.1 Generalized optical theorem

In an ideal scattering experiment the total current must be conserved. This requirement is a consequence of the conservation of the number of particles during the interaction process if we neglect absorption effects and relativistic pair generation for very high energies above $2\,mc^2$. For standard transmission electron microscopy the influence of these effects is negligibly small. The probability current density is given by the symmetric expectation value of the momentum operator

$$\mathbf{j}(\mathbf{r}) = \frac{\hbar}{2im} \int \left[\Psi^* \frac{\partial}{\partial \mathbf{r}} \Psi - \Psi \frac{\partial}{\partial \mathbf{r}} \Psi^* \right] d\mathbf{R}^l \tag{3.6}$$

with respect to the total wave function $\Psi = \Psi(\mathbf{r}, \mathbf{R}, t)$. The conservation of the probability current implies $\operatorname{div} \mathbf{j} = 0$ in the entire space. We can transform this relation into an integral equation by applying the Gaussian theorem. The resulting integral

$$\frac{\hbar}{2im} \int_S r^2 \int \left[\Psi^* \frac{\partial}{\partial r} \Psi - \Psi \frac{\partial}{\partial r} \Psi^* \right] d\mathbf{R}^l \, d^2\Omega = 0 \tag{3.7}$$

over the unit sphere S vanishes. Assuming that our object is initially illuminated by a superposition of two plane waves with wave vectors $|\mathbf{k}| = |\mathbf{k}'| = k_0$

$$\Psi_i(\mathbf{r}, \mathbf{R}) = \left(c_1 \exp\left(i\mathbf{k}\mathbf{r}\right) + c_2 \exp\left(i\mathbf{k}'\mathbf{r}\right) \right) \phi_0(\mathbf{R}) \,, \quad c_1, c_2 \in \mathbb{C} \,, \tag{3.8}$$

we get, after some rearrangements from (3.6), (3.1), and (2.13) for large $r \to \infty$ in the Fraunhofer domain (3.3) the asymptotic expression

$$\lim_{r\to\infty} \frac{\hbar}{2im} \left[|c_1|^2 J(\mathbf{k}, \mathbf{k}) + c_1^* c_2 J(\mathbf{k}, \mathbf{k}') + c_1 c_2^* J(\mathbf{k}', \mathbf{k}) + |c_2|^2 J(\mathbf{k}', \mathbf{k}') \right] = 0 \,, \tag{3.9}$$

where the function J is defined by a sum of four integrals

$$\begin{aligned} J(\mathbf{k},\mathbf{k}') &= ir\int_S \mathbf{r}(\mathbf{k}+\mathbf{k}')\exp\left(-i(\mathbf{k}-\mathbf{k}')\mathbf{r}\right)\,d^2\Omega \\ &- \int f_{00}(\boldsymbol{\theta},\mathbf{k})\exp\left(ik_0r-i\mathbf{k}'\mathbf{r}\right)\left(1-i\mathbf{k}'\mathbf{r}-ik_0r\right)d^2\Omega \\ &+ \int f_{00}^*(\boldsymbol{\theta},\mathbf{k}')\exp\left(-ik_0r+i\mathbf{k}\mathbf{r}\right)\left(1+i\mathbf{k}'\mathbf{r}+ik_0r\right)d^2\Omega \\ &+ \sum_{n=0}^{\infty}\int f_{n0}(\boldsymbol{\theta},\mathbf{k})f_{n0}^*(\boldsymbol{\theta},\mathbf{k}')\left(ik_n-\frac{1}{r}+ik_n+\frac{1}{r}\right)d^2\Omega\,. \end{aligned} \tag{3.10}$$

The integration must be performed with respect to the direction vector $\boldsymbol{\theta}=\mathbf{r}/r$. After a rather lengthy calculation outlined in appendix B we eventually find

$$\lim_{r\to\infty} J(\mathbf{k},\mathbf{k}') = -4\pi\left(f_{00}(\mathbf{k},\mathbf{k}')-f_{00}^*(\mathbf{k}',\mathbf{k})\right)-\sum_{n=0}^{\infty}2ik_n\int f_{n0}(\mathbf{k},\boldsymbol{\theta})f_{n0}^*(\mathbf{k}',\boldsymbol{\theta})\,d^2\Omega\,. \tag{3.11}$$

The integration over the solid angle comprises all directions $\boldsymbol{\theta}$ of the final scattering vectors $\mathbf{k}_n$ for $n=0,1,\ldots$.

The condition (3.9) must be fulfilled for arbitrary pairs of complex constants c_1 and c_2. This is only the case if the function J vanishes identically in the asymptotic limit yielding

$$\frac{1}{2i}\left\{f_{00}(\mathbf{k},\mathbf{k}')-f_{00}^*(\mathbf{k}',\mathbf{k})\right\}=\sum_{n=0}^{\infty}\frac{k_n}{4\pi}\int f_{n0}(\mathbf{k},\boldsymbol{\theta})f_{n0}^*(\mathbf{k}',\boldsymbol{\theta})\,d^2\Omega\,. \tag{3.12}$$

This fundamental property of the scattering amplitude is known as the generalized optical theorem [6]. It is a consequence of the unitarity of the mapping from the initial states onto the final states of the scattering process. The generalized optical theorem is valid for elastic and inelastic scattering. In the special case $\mathbf{k}=\mathbf{k}'$ the relation (3.12) reduces to the well known optical theorem of scattering theory

$$\begin{aligned} \frac{1}{2i}\left\{f_{00}(\mathbf{k},\mathbf{k})-f_{00}^*(\mathbf{k},\mathbf{k})\right\} &= \sum_{n=0}^{\infty}\frac{k_n}{4\pi}\int f_{n0}(\mathbf{k},\boldsymbol{\theta})f_{n0}^*(\mathbf{k},\boldsymbol{\theta})\,d^2\Omega \\ &= \frac{k_0}{4\pi}\left(\sigma_{\mathrm{el}}+\sigma_{\mathrm{in}}\right)\,. \end{aligned} \tag{3.13}$$

The left–hand side is the imaginary part of the elastic scattering amplitude in forward direction, while the right–hand side is proportional to the total elastic and inelastic scattering cross section. Hence the elastic scattering amplitude contains information about all possible excitations of the object. The second relation on the right–hand side

of (3.13) is obtained by considering the definition of the differential scattering cross sections

$$\frac{d\sigma_n}{d\Omega} = \frac{k_n}{k_0}|f_{n0}(\mathbf{k}_f, \mathbf{k}_i)|^2 \,, \quad n = 0, 1, \ldots \tag{3.14}$$

for elastic ($n = 0$) and inelastic ($n \neq 0$) scattering. It should be noted that the differential scattering cross section generally depends on the initial $\mathbf{k}_i$ and the final $\mathbf{k}_f$ scattering direction. Only in a few special cases it is a function of the transferred momentum $\hbar\,(\mathbf{k}_f - \mathbf{k}_i)$.

The elastic scattering amplitude can be written as a sum of a symmetric and an anti–symmetric contribution

$$f_{00}(\mathbf{k}_f, \mathbf{k}_i) = F_s(\mathbf{k}_f, \mathbf{k}_i) + iF_a(\mathbf{k}_f, \mathbf{k}_i) \tag{3.15}$$

with $F_s(\mathbf{k}_f, \mathbf{k}_i) = F_s^*(\mathbf{k}_i, \mathbf{k}_f)$ and $F_a(\mathbf{k}_f, \mathbf{k}_i) = -F_a^*(\mathbf{k}_i, \mathbf{k}_f)$. In particular this decomposition shows that the generalized optical theorem (3.12) connects the anti–symmetric part of the elastic scattering amplitude to the quadratic terms of the elastic and inelastic scattering amplitudes. Because the generalized optical theorem is a direct consequence of the conservation of the number of particles any reliable approximation method employed for the calculation of electron micrographs must consider the contributions of second order in the scattering amplitude in order to correctly describe the non-linear behaviour to the image intensity.

3.2 First–order Born approximation

The system of coupled integral equations (2.3) can be solved in principle by employing the method of successive approximation. In the case of a weak scattering potential it suffices to perform the first step of the iteration. We substitute the wave function ψ on the right hand side of equation (2.3) by the zeroth–order approximation $\psi_m^{(0)} = \delta_{m0} \exp(i\mathbf{k}_0\mathbf{r})$ which represents the undisturbed incident wave. From the resulting first–order approximation of the scattered electron wave

$$\psi_m^{(1)}(\mathbf{r}) = \exp(i\mathbf{k}_0\mathbf{r})\ \delta_{m0} - \frac{1}{4\pi}\int \exp(i\mathbf{k}_0\mathbf{r}')\ U_{m0}(\mathbf{r}')\frac{\exp(ik_m|\mathbf{r}-\mathbf{r}'|)}{|\mathbf{r}-\mathbf{r}'|}\,d^3\mathbf{r}' \tag{3.16}$$

we find the first–order approximation of the scattering amplitude by evaluating the integral in the Fraunhofer domain. Inserting the Fraunhofer approximation (3.3) into equation (3.16) and comparing the result with equation (3.1), we obtain the first–order Born approximation for the elastic ($m = 0$) and inelastic ($m \neq 0$) scattering amplitudes

$$f_m^{(1)}(\mathbf{k}_m, \mathbf{k}_0) = f_{m0}^B(\mathbf{k}_m - \mathbf{k}_0) = -\frac{1}{4\pi}\int U_{m0}(\mathbf{r}')\exp(-i(\mathbf{k}_m - \mathbf{k}_0)\mathbf{r}')\,d^3\mathbf{r}' \,. \tag{3.17}$$

Thus, in first–order approximation the scattering amplitudes are proportional to the three–dimensional Fourier transformation of the corresponding matrix elements of the scattering potential U_{m0}. In this approximation the scattering amplitudes depend linearly on the object potential. Therefore, the kinematic theory of scattering, which is based on the first–order Born approximation, is a straight forward and compared to the more general dynamic approach a much simpler theory. Unfortunately, its range of validity in electron microscopy is limited to thin amorphous objects. The Born approximation of the scattering amplitude (3.17) is the first–order term of the expansion of the scattering amplitude into a von–Neumann series. The first–order Born approximation yields reasonable results for the scattering of fast electrons at single atoms with low atomic numbers. However, this approximation fails if we consider the scattering at an assembly of atoms because this approximation does not account for *shadowing effects* caused by multiple scattering. In the case of a spherically symmetric atomic potential the first–order Born approximation of the scattering amplitude is real–valued for all scattering angles whereas the exact scattering amplitude is always complex–valued. Accordingly, the first–order Born approximation does not account for the phase shift which depends on the scattering angle. Hence, the interference between the partial waves originating from different atoms of the assembly is not considered correctly. This explains why the kinematical theory of electron diffraction may fail even for relatively thin specimens. Especially in high–resolution imaging this inaccuracy is appreciably large because the high–angle contributions are strongly affected by the large phase shifts produced by the electrons which penetrate deeply into the atomic potential.

3.3 Higher–order contributions

In order to calculate higher–order Born approximations of the scattering amplitude it is advantageous to employ the Fourier representation of the Green function

$$\lim_{\varepsilon\to 0}\frac{1}{(2\pi)^3}\int\frac{1}{k^2-K^2+i\varepsilon}\,\exp\left(i\mathbf{Kr}\right)\,d^3\mathbf{K}=-\frac{1}{4\pi}\frac{\exp\left(ikr\right)}{r}\,. \tag{3.18}$$

The integration on the left hand side must be performed carefully because the small parameter ϵ must approach zero from positive values to account for the fact that the Green function corresponds to an outgoing spherical wave. Using the preceeding form of the Green function, we can formally calculate the higher–order Born approximation of the scattering amplitude by successive iteration. Starting from equation (2.3) and

comparing it with (3.2), we eventually find the $(n+1)$th–order expansion term as

$$f_m^{(n+1)}(\mathbf{k}_m,\mathbf{k}_0) = \left(\frac{-1}{2\pi^2}\right)^n \sum_{l_1=0}^{\infty}\cdots\sum_{l_n=0}^{\infty}\int\cdots\int \frac{f^B_{l_1 0}(\mathbf{k}'_1-\mathbf{k}_0)}{k_{l_1}^2-k_1'^2}\cdots \times \frac{f^B_{l_n l_{n-1}}(\mathbf{k}'_n-\mathbf{k}'_{n-1})}{k_{l_n}^2-k_n'^2}\, f^B_{m l_n}(\mathbf{k}_m-\mathbf{k}'_n)\, d^3\mathbf{k}'_1\ldots d^3\mathbf{k}'_n\ . \tag{3.19}$$

Although this expression is rather involved, its structure is quite simple. The higher–order terms in (3.19) can be understood as the contributions of multiple scattering. Each integral in the expression (3.19) must be evaluated analogously to the integral (3.18) in order to correctly fulfill the boundary conditions of the scattering problem.

The first–order Born approximation of the elastic scattering amplitude satisfies the symmetry relation $f^B_{00}(\mathbf{K}) = f^{B*}_{00}(-\mathbf{K})$. Hence this function is real–valued for scattering in forward direction $\mathbf{K}=0$. Accordingly, the first–order Born approximation violates the optical theorem (3.13). However, the generalized optical theorem (3.12) can be utilized to determine the anti–symmetric part of the elastic scattering amplitude in second–order Born approximation which depends quadratically on the scattering potential. To be consistent in the approximation, we expand the scattering amplitudes on both sides of (3.12) with respect to the strength of the scattering potential and we drop all terms of third and higher order [8]. The result

$$\frac{1}{2i}\left\{f_0^{(2)}(\mathbf{k}_0,\mathbf{k}'_0)-f_0^{(2)*}(\mathbf{k}'_0,\mathbf{k}_0)\right\} = \sum_{n=0}^{\infty}\frac{k_n}{4\pi}\int f^B_{n0}(\mathbf{k}_0-\mathbf{k}) f^{B*}_{n0}(\mathbf{k}'_0-\mathbf{k})\, d^2\Omega \tag{3.20}$$

can also be obtained from the general representation (3.19) of the Born approximation. In second order we find

$$f_0^{(2)}(\mathbf{k}_0,\mathbf{k}'_0) = -\frac{1}{2\pi^2}\lim_{\varepsilon\to 0}\sum_{n=0}^{\infty}\int \frac{1}{k_n^2-\mathbf{k}^2+i\varepsilon}\, f^B_{n0}(\mathbf{k}_0-\mathbf{k})\, f^{B*}_{n0}(\mathbf{k}'_0-\mathbf{k})\, d^3\mathbf{k}\ . \tag{3.21}$$

Using the representation of Dirac's delta function by a limit of Lorentzian functions

$$\lim_{\varepsilon\to 0}\left[\frac{1}{k_n^2-k^2-i\varepsilon}-\frac{1}{k_n^2-k^2+i\varepsilon}\right] = \lim_{\varepsilon\to 0}\frac{2i\varepsilon}{(k_n^2-k^2)^2+\varepsilon^2} = 2\pi i\delta(k_n^2-k^2)\ , \tag{3.22}$$

the $\mathbf{k}$–integration is confined to the surface of a sphere with the radius $k=k_n$. Then the result coincides with the right–hand side of (3.20). The remaining symmetric part of the second–order Born approximation (3.21) has the form

$$\frac{1}{2}\left\{f_0^{(2)}(\mathbf{k}_0,\mathbf{k}'_0)+f_0^{(2)*}(\mathbf{k}'_0,\mathbf{k}_0)\right\} = \frac{1}{2\pi^2}\sum_{n=0}^{\infty}P\int \frac{f^B_{n0}(\mathbf{k}-\mathbf{k}_0) f^{B*}_{n0}(\mathbf{k}-\mathbf{k}'_0)}{k_n^2-\mathbf{k}^2}\, d^3\mathbf{k}\ . \tag{3.23}$$

For the evaluation of the volume integral in the last expression the Cauchy principal value must be taken with respect to the integration over the variable $\mathbf{k}$, as indicated by the letter P in front of the integral sign [8] .

The different structures of the expressions (3.20) and (3.23) allow a illustrative interpretation of the contribution of the second–order Born approximation to the scattering amplitude. Both expressions describe the contributions of the double scattering processes to the elastic scattering amplitude. For elastic scattering the initial and final momentum states have equal modulus $|\mathbf{k}_i| = |\mathbf{k}_f|$. Since the intermediate states are not observable energy conservation is not required for these *virtual* states. The anti–symmetric part (3.20) of the second–order Born approximation accounts only for the *real* intermediate states on the energy shell. The symmetric part (3.23) additionally comprises the scattering events off the energy shell. In the case of purely elastic scattering all internal degrees of freedom are frozen in and do not contribute. In this case the contribution of the second–order Born approximation reduces to elastic double scattering. The effect of inelastic scattering on the elastic scattering amplitudes appears in second–order Born approximation. The optical theorem optimally illustrates the interrelation existing between the elastic and inelastic scattering processes.

3.4 Single atom scattering

The first–order Born approximation yields analytical expressions for the scattering amplitudes and for the scattering cross sections of elastic and inelastic scattering at some simple potentials. Therefore, we should not expect a very precise agreement between the analytical results and the experimental observations. Nevertheless, the resulting simple formulas can serve as first approximations since they describe the overall properties of the scattering amplitudes rather well.

The well–known Wentzel–Yukawa potential

$$U(\mathbf{r}) = -\frac{2\gamma Z}{a_H}\,\frac{\exp\left(-\frac{|\mathbf{r}|}{R}\right)}{|\mathbf{r}|} \tag{3.24}$$

represents a good approximation for the potential of a single atom if we disregard the effects resulting from the shell structure of the electron density. The screening radius R is a measure for the shielding of the nucleus by the electron cloud; $a_H = 4\pi\varepsilon_0\hbar^2/me^2$ denotes the Bohr radius and Z the atomic number, respectively. The shielding radius is a free parameter which can be used to match the Wentzel–Yukawa potential with more accurate models [36]. The statistical Thomas–Fermi atomic model [4] yields $R = \frac{a_H}{2}\left(\frac{3\pi}{4}\right)^{2/3} Z^{-1/3}$. Another reasonable choice is $R^2 = \langle r^2 \rangle/6$, where $\langle r^2 \rangle$ denotes the mean square radius of the electron cloud of the scattering atom. The scattering amplitudes calculated from the Wentzel–Yukawa potential are rather realistic for small scattering angles because the exponential decrease of the Wentzel–Yukawa potential

is fairly accurate. Employing this model, we obtain from (3.17) the elastic scattering amplitude

$$f_{00}^{B}(\mathbf{k}_0' - \mathbf{k}_0') = \frac{2\gamma Z R^2}{a_H} \, \frac{1}{R^2|\mathbf{k}_0 - \mathbf{k}_0'|^2 + 1} \tag{3.25}$$

in first Born approximation. Since in high–resolution electron microscopes the acceleration voltage U is higher than 60 kV the shielding radius fulfills the relation $R \gg \lambda$ and we can employ the small–angle approximation for the scattering vector

$$|\mathbf{k}_0 - \mathbf{k}_0'| = 2k_0 \sin(\theta/2) \approx k_0\theta \, , \tag{3.26}$$

where $\theta \ll 1$ denotes the angle enclosed by the initial $\mathbf{k}_0$ and final $\mathbf{k}_0'$ scattering direction. The error introduced by this approximation is very small, the relative error depends quadratically on θ and is below 1.0 per cent as long as the scattering angle is smaller than $\theta < 488$ mrad. Hence the elastic differential cross section adopts the form

$$\frac{d\sigma_{\text{el}}^{B}}{d\Omega} = |f_{00}^{B}(\theta)|^2 = \left(\frac{2\gamma Z R^2}{a_H}\right)^2 \frac{\theta_0^4}{\left(\theta^2 + \theta_0^2\right)^2} \, , \quad \theta_0 = \frac{1}{k_0 R} \, . \tag{3.27}$$

By performing the integration over the full angular range, we obtain the result

$$\sigma_{\text{el}} = \frac{4\pi\,\gamma^2}{k_0^2} \, \frac{Z^2 R^2}{a_H^2} \tag{3.28}$$

for the total elastic scattering cross section. This approximation agrees quite well with the result of more accurate calculations and represents a very useful rule of thumb [2].

According to the results derived in first–order Born approximation from the Wentzel–Yukawa potential, elastic scattering is confined to a cone with half angle θ_0 which is called the characteristic angle of elastic scattering. The more the atom potential is extended the more the scattering is peaked about the forward direction. For large scattering angles $\theta \gg \theta_0$ the scattering amplitude decreases proportional to $1/\theta^2$. As an example we consider 60 keV electrons scattered by Silicon ($Z = 14$). In this case the characteristic scattering angle is $\theta_0 = 18$ mrad and about 50 percent of the incident electrons are scattered into angles smaller than θ_0.

For a more realistic treatment of electron scattering by single atoms, we must take into account the exact interaction potential

$$U(\mathbf{r}, \mathbf{R}_0, \ldots, \mathbf{R}_Z) = -\frac{2\gamma}{a_H} \left(\frac{Z}{|\mathbf{r} - \mathbf{R}_0|} - \sum_{\nu=1}^{Z} \frac{1}{|\mathbf{r} - \mathbf{R}_\nu|} \right) \tag{3.29}$$

between a scattered electron and a single atom with atomic number Z. The first term in this expression results from the charge of the atomic nucleus located at the position

$\mathbf{R}_0$. The other terms describe the interaction of the incident electron with the electrons of the atom at the positions $\mathbf{R}_\nu$, for $\nu = 1, \ldots, Z$. The distribution of the atomic electrons is determined by the Z–particle electron wave functions $\phi_n = \phi_n(\mathbf{R}) = \phi_n(\mathbf{R}_1, \ldots, \mathbf{R}_Z)$ of the free atom. The index n denotes the energy eigenstate of the atom.

Inelastic scattering mainly results from an interaction of the incident electron with the electrons of the object except for thermally diffuse or phonon scattering. If we neglect such non–electronic excitations the position of the nucleus remains fixed $\mathbf{R}_0 = 0$. Inelastic scattering due to electronic excitations is confined to small scattering angles. The energy loss and the scattering angle are related to each other. The closer the electron passes the nucleus the higher the excitation energy becomes which must be transferred to the atomic electron in order to make a transition since the probability to hit a tightly bound electron increases with decreasing distance from the atomic nucleus. In first–order Born approximation we can validate this intuitive argument more quantitatively.

By inserting the interaction potential (3.29) into the expression (3.17) for the scattering amplitude in first–order Born approximation, we can perform the integration with respect to $\mathbf{r}$ analytically. We find the approximation

$$\begin{aligned} f_{n0}^B(\mathbf{K}_n) &= -\frac{1}{4\pi}\int \exp\left(-i\mathbf{K}_n\mathbf{r}\right) U_{n0}(\mathbf{r}) d^3\mathbf{r} \\ &= \frac{2\gamma}{a_H}\,\frac{1}{|\mathbf{K}_n|^2}\left(Z\,\delta_{n0} - \sum_{\nu=1}^{Z}\int \phi_n^*(\mathbf{R})\phi_0(\mathbf{R})\,\exp\left(-i\mathbf{K}_n\mathbf{R}_\nu\right)\,d^{3Z}\mathbf{R}\right) \end{aligned} \tag{3.30}$$

for the scattering amplitudes for elastic and inelastic scattering.

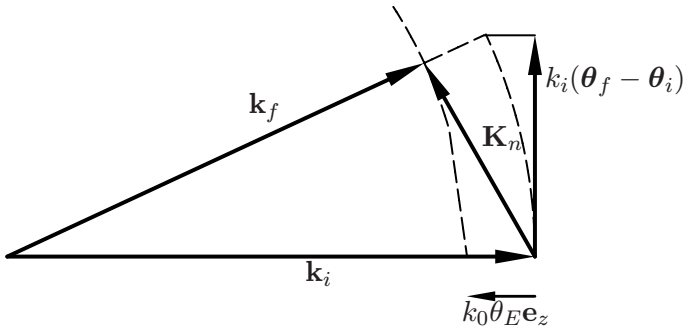

Figure 3.2: *The scattering vector $\mathbf{K}_n$ is the difference vector between the final $\mathbf{k}_f$ and initial $\mathbf{k}_i$ wave vectors of the scattered electron wave. The scattering vector beaks down into a lateral component $\mathbf{q}$ perpendicular to the optic axis and a longitudinal component parallel to the optic axis. For small energy losses and small scattering angles the longitudinal component is given by $-k_0\theta_E\mathbf{e}_z$. Within the frame of validity of this small–angle approximation the lateral component is not affected by the energy loss.*

The scattering vector $\mathbf{K}_n$ is a function of the energy loss $\varepsilon_n = E_n - E_0$ of the scattered electron. For sufficiently small energy losses $|\varepsilon_n| \ll eU$ the scattering vector is approximately given by [37, 26]

$$\mathbf{K}_n = \mathbf{q} - k_0\theta_E \mathbf{e}_z \ , \quad \theta_E = \frac{\varepsilon_n}{2eU} \ \frac{eU + mc^2}{eU/2 + mc^2} \ . \tag{3.31}$$

The relations between the scattering vector $\mathbf{K}_n$, the initial and final wave vector and the characteristic angle for inelastic scattering θ_E are depicted in figure 3.2. The relation (3.31) between the energy loss ϵ_n and the angle θ_E follows from the energy relation (2.10) if we assume $k_n \approx k_0$ for small energy losses.

Within the frame of validity of the small–angle approximation (3.26) the vector $\mathbf{q}$ in equation (3.31) denotes the lateral component of the scattering vector. The characteristic scattering angle for inelastic scattering θ_E equals one half of the relative energy loss up to a relativistic factor. Hence the momentum transfer between the scattered electron and the object is always non–zero, for inelastic scattering. The minimum momentum transfer $\hbar k_0 \theta_E$ occurs for forward scattering ($\theta = 0$).

The differential cross section for inelastic scattering is a function of the energy loss. Using the equation (3.30) and the definition (3.14), we obtain the expression

$$\begin{aligned} \frac{d^2\,\sigma}{d\Omega d\varepsilon} &= \left(\frac{2\gamma}{a_H}\right)^2 \sum_{n=0}^{\infty} \frac{1}{|\mathbf{K}_n|^4} \ \frac{k_n}{k_0} \delta(\varepsilon - E_n + E_0) \\ &\times \left| Z\ \delta_{n0} - \sum_{\nu=1}^{Z} \int \phi_n^*(\mathbf{R})\phi_0(\mathbf{R}) \ \exp\left(-i\mathbf{K}_n\mathbf{R}_\nu\right) \ d^{3Z}\mathbf{R} \right|^2 \end{aligned} \tag{3.32}$$

for the double–differential scattering cross section. Owing to the delta functions on the right–hand side, the double–differential scattering cross section is non–zero only if the energy loss ε matches one of the possible excitation energies $\varepsilon_n = E_n - E_0$ with $n = 0, 1, \ldots$. The first term ($n = 0$) of the sum accounts for elastic scattering. Accordingly, the elastic scattering amplitude in first–order Born approximation is described by the Bethe–Mott [38] formula

$$f_{00}^B(\mathbf{K}_0) = \frac{2\gamma}{a_H} \ \frac{Z - F(\mathbf{K}_0)}{\mathbf{K}_0^2} \ . \tag{3.33}$$

The electronic form factor

$$\begin{aligned} F(\mathbf{K}) &= \int \phi_0^*(\mathbf{R})\phi_0(\mathbf{R}) \ \left(\sum_{\nu=1}^{Z} \exp\left(-i\mathbf{K}\mathbf{R}_\nu\right)\right) \ d^{3Z}\mathbf{R} \\ &= \int \varrho(\mathbf{r}') \ \exp\left(-i\mathbf{K}\mathbf{r}\right) \ d^3\mathbf{r} \end{aligned} \tag{3.34}$$

is the Fourier transform of the electron density of the atom

$$\varrho(\mathbf{r}) = \int \phi_0^*(\mathbf{R}) \left(\sum_{\nu=1}^{Z} \delta(\mathbf{r} - \mathbf{R}_\nu) \right) \phi_0(\mathbf{R}) \, d^{3Z}\mathbf{R} \tag{3.35}$$

in the ground state. This form factor represents the x–ray scattering amplitude. The electron scattering amplitude and the atomic form factor in first–order Born approximation are closely connected by the Bethe–Mott formula (3.33) which is a reformulation of Poissons equation of electrodynamics in reciprocal space.

If equation (3.33) is evaluated numerically, care must be taken for small scattering angles due to the vanishing nominator. For very small scattering vectors $|\mathbf{K}| \ll k_0$ and spherically symmetric charge density the expansion of (3.33) in a power series with respect to $|\mathbf{K}|$ yields

$$f_{00}^B(\mathbf{K}) = \frac{2\gamma Z}{a_H} \left(\frac{\langle r^2 \rangle}{6} - \frac{\langle r^4 \rangle}{120} \mathbf{K}^2 + \mathcal{O}(\mathbf{K}^4) \right) . \tag{3.36}$$

Here $\langle r^2 \rangle$ denotes the mean square radius of the atomic electron density and $\langle r^4 \rangle$ its next higher moment. The comparison of the small–angle behavior of the electron scattering amplitude with the corresponding result for the less accurate Wentzel–Yukawa potential suggests the choice $R^2 = \langle r^2 \rangle$ in order to improve the Wentzel–Yukawa approximation. This justifies the ad hoc assumption for the shielding radius of the Wentzel–Yukawa potential in (3.24).

A much better approximation for the elastic scattering amplitude in first–order Born approximation can be obtained by Hartree–Dirac–Fock–Slater methods. These numerical computations yield the charge density of a single atom in its ground state. The scattering amplitudes obtained by means of these data are tabulated in the literature [39]. It is convenient to parameterize the numerical data by appropriate fit functions. For analytical calculations it is crucial to find a representation in terms of a small number of simple basis functions that provide sufficient accuracy and have the correct asymptotical behaviour for large scattering angles. To describe the atomic form factor a Gaussian fit introduced by Doyle and Turner is very useful. The corresponding parameterization has the form [39]

$$F_{DT}(\mathbf{K}) = \sum_{n=1}^{N_{DT}} A_n \, \exp\left(-B_n \, \mathbf{K}^2\right) . \tag{3.37}$$

The real and positive parameters $A_n, B_n > 0$, $n = 1, \ldots, N_{DT}$, must be determined for each element by a least–squares fit to the numerically obtained form factors. From the representation (3.37) it becomes clear that these parameters must fulfill the relation

$$F(\mathbf{K} = 0) = Z = \sum_{n=1}^{N_{DT}} A_n \tag{3.38}$$

and the mean–square diameter of the atomic charge distribution has the form

$$\langle r^2 \rangle = \frac{6}{Z} \sum_{n=1}^{N_{DT}} A_n B_n \ . \tag{3.39}$$

The Bethe–Mott formula (3.33) relates the atomic form factor with the elastic scattering amplitude in first–order Born approximation

$$F(\mathbf{K}) = Z - \frac{a_H}{2\gamma} \mathbf{K}^2 \ f_{00}^B(\mathbf{K}) \ . \tag{3.40}$$

This relations suggests a parameterization of the elastic scattering amplitudes in first–order Born approximation by a modified set of basis functions [40]

$$f_{00}^B(\mathbf{K}) = \frac{2\gamma}{a_H} \sum_{n=1}^{N_{KW}} a_n \frac{1 - \exp\left(-b_n \mathbf{K}^2\right)}{\mathbf{K}^2} \tag{3.41}$$

with real and positive parameters $a_n, b_n > 0$, $n = 1, \ldots, N_{KW}$. This fit has been introduced by Kohl and Weickenmeier and provides the correct asymptotic behaviour for small and large scattering vectors. If the number of fitting functions $N_{DT} = N_{KW}$ for both fits are equal we could use one set of parameters to describe both, the atomic potential and the atomic charge distribution via the Kohl–Weickenmeier or the Doyle–Turner approximation, respectively. However, to obtain a more accurate approximation different sets of parameters a_n, b_n, for $n = 1, \ldots, N_{KW}$ and A_n, A_n, for $n = 1, \ldots, N_{DT}$ are required.

Even in the case of the parameterization (3.41) the total elastic scattering cross section can be expressed analytically. To perform the integration with respect to the spatial angle it is convenient to use the formal relation

$$\frac{1 - \mathrm{e}^{-b_n \mathbf{K}^2}}{\mathbf{K}^2} = \int_0^{b_n} \mathrm{e}^{-b \mathbf{K}^2} db \ . \tag{3.42}$$

Accordingly, the total elastic scattering cross section adopts the form

$$\sigma_{el} = \frac{\pi}{k_0^2} \left(\frac{2\gamma}{a_H} \right)^2 \sum_{m=1}^{N_{KW}} \sum_{n=1}^{N_{KW}} a_m a_n \left\{ b_m \ln \left(\frac{b_m + b_n}{b_m} \right) + b_n \ln \left(\frac{b_m + b_n}{b_n} \right) \right\} \ . \tag{3.43}$$

Although the results of the first–order Born approximation are totally inadequate for a reliable image simulation in electron microscopy, the first–order Born approximation of the atomic scattering amplitude is still important even for more accurate approximation methods used for image simulation. Since the first–order Born approximation is related to the atomic potential by the Fourier transformation it can be used as a convenient parameterization of the real object potential as far as the effects of the bounding charge are negligible and the independent atom approximation is sufficiently accurate.

The differential cross section of inelastic scattering is given by the terms $n > 0$ in expression (3.32). These terms can also be calculated numerically in a quite realistic approximation. Unfortunately, these calculations require a large amount of expenditure. Moreover, the inelastic scattering factors obtained by this method depend on the element type in a non–trivial way [41].

Fortunately, it is possible to achieve a simple approximation for the inelastic contribution to the total scattering cross section in the case of high–energy scattering by making use of the completeness relation of the atomic wave functions. For this purpose we neglect the details of the electronic excitation and approximate the energy transfer between the scattered electron and the atom by a mean energy loss $\varepsilon \approx \bar{\varepsilon}$. A reasonable choice [37] for the mean energy loss is $\bar{\varepsilon} = ZE_H/2$, where $E_H = 13.6\text{eV}$ denotes the Rydberg energy. This value is proportional to the atomic number Z and roughly equals one half of the excitation energy of the atomic resonance line. Within the frame of validity of this approximation the inelastic scattering vectors $\mathbf{K}_n$, $n = 1, 2, \ldots$ are replaced by an average scattering vector $\bar{\mathbf{K}}$. The characteristic scattering angle θ_E due to the mean energy loss has the effect of a shielding radius which limits the range of interaction between the scattered electron and the atomic electrons. This spatial cut–off of the Coulomb interaction prevents a divergence of the total inelastic cross section [7].

With these assumptions the summation over the final states ϕ_n in the expression (3.32) for the double differential cross section of inelastic scattering can be performed. The additional integration over the energy loss eventually yields

$$\frac{d\sigma_{\text{in}}}{d\Omega} = \left(\frac{2\gamma}{a_H}\right)^2 \frac{1}{|\bar{\mathbf{K}}|^4} \sum_{n=1}^{\infty} \left| \sum_{\nu=1}^{Z} \int \phi_n^*(\mathbf{R})\phi_0(\mathbf{R}) \exp\left(-i\bar{\mathbf{K}}\mathbf{R}_\nu\right) d\mathbf{R}^{3Z} \right|^2 \tag{3.44}$$

$$= \left(\frac{2\gamma}{a_H}\right)^2 \frac{1}{|\bar{\mathbf{K}}|^4} \left\{ \int \sum_{\mu,\nu=1}^{Z} \exp\left(i\bar{\mathbf{K}}(\mathbf{R}_\mu - \mathbf{R}_\nu)\right) |\phi_0(\mathbf{R})|^2 d^{3Z}\mathbf{R} - \left| \sum_{\nu=1}^{Z} \int |\phi_0(\mathbf{R})|^2 \exp\left(i\bar{\mathbf{K}}\mathbf{R}_\nu\right) \right|^2 d^{3Z}\mathbf{R} \right\} . \tag{3.45}$$

The expression in parentheses is the Fourier transformation of the variance of the mixed electron density of the atom averaged over its ground state. Assuming that the electrostatic correlations between the electrons of the atom are negligibly small, we may approximate the mixed term in expression (3.44) by the square of the ground state electron density or, equivalently, by the electron form factor (3.34). This yields an approximation of the differential inelastic scattering cross section

$$\frac{d\sigma_{\text{in}}}{d\Omega} = \left(\frac{2\gamma}{a_H}\right)^2 \frac{Z - \frac{1}{Z}F^2(\bar{\mathbf{K}})}{|\bar{\mathbf{K}}|^4} , \tag{3.46}$$

where $F(\mathbf{K})$ denotes the electronic form factor defined in equation (3.34). The last expression is equivalent to that derived classically by Raman and Compton [42] for

x-ray scattering. It has been successfully used to describe inelastic electron scattering by Lenz [36] and Rose [26]. Therefore, equation (3.46) is called the modified Raman–Compton approximation with mean energy loss.

In order to derive a simple analytic expression for the inelastic scattering cross section it is advantageous to employ the Wentzel–Yukawa potential (3.24). This potential yields the expression

$$\frac{d\sigma_{\text{in}}}{d\Omega} = 2\pi \left(\frac{2\gamma}{k_0^2 a_H}\right)^2 \frac{Z}{(\theta^2+\theta_E^2)^2}\left(1 - \frac{\theta_0^4}{(\theta^2+\theta_0^2+\theta_E^2)^2}\right) \tag{3.47}$$

for the small–angle approximation of the differential inelastic scattering cross section. Expression (3.47) shows that the characteristic energy loss strongly influences the Lorentzian factor in front of the parentheses but has very little influence on the Wentzel term inside the parentheses, since the relation $\theta_0 \gg \theta_E$ always holds true.

The integration of the differential scattering cross section over the full solid angle is performed by the same method as in (3.28) with the result

$$\begin{aligned} \sigma_{\text{in}} &= 2\pi \left(\frac{2\gamma}{a_H k_0^2}\right)^2 Z \left\{\frac{\ln\left(1+\frac{\theta_0}{\theta_E}\right)}{\theta_0^2} - \frac{1}{2\left(\theta_0^2+\theta_E^2\right)}\right\} \\ &\approx 2\pi \left(\frac{2\gamma}{a_H k_0^2}\right)^2 \frac{Z}{\theta_0^2}\left\{\ln\left(\frac{\theta_0}{\theta_E}\right) - \frac{1}{2}\right\}, \end{aligned} \tag{3.48}$$

where the second expression presupposes $\theta_0 \gg \theta_E$.

The comparison of the last result with the relation (3.28) for the elastic scattering cross section shows that their ratio is proportional to $1/Z$ and depends only logarithmically on the acceleration voltage. More elaborate calculations based on the modified Raman–Compton approximation (3.46) using the Doyle–Turner fit (3.37) for tabulated x–ray scattering amplitudes confirm this behaviour. The relation

$$\sigma_{\text{in}}/\sigma_{\text{el}} \approx 20/Z \tag{3.49}$$

may serve as a useful rule of thumb in many cases. This formula agrees surprisingly well with experimental results [2]. It shows that inelastic scattering is predominant for light elements. Hence the contrast in electron micrographs of biological specimens is strongly affected by inelastically scattered electrons if no energy filter is used.

Even in the case of the Doyle–Turner approximation for the atomic form factor the total inelastic scattering cross section with respect to the modified Raman–Compton model can be calculated analytically in terms of the first integral exponential function

$$\mathrm{E}_1(x) = \int_x^\infty \frac{\mathrm{e}^{-t}}{t} dt\ . \tag{3.50}$$

Using this definition a short calculation yields

$$\sigma_{in} = \frac{\pi}{Z\theta_E^2 k_0^4}\left(\frac{2\gamma}{a_H}\right)^2 \left\{ Z^2 - \sum_{m,n=1}^{N_{DT}} A_m A_n \left[1 - \mathrm{e}^{-(B_m+B_n)k_0^2\theta_E^2} - (B_m+B_n)\,\theta_E^2 k_0^2\,\mathrm{E}_1((B_m+B_n)k_0^2\theta_E^2)\right]\right\} . \tag{3.51}$$

Alternatively the integral can by approximated by more simple functions if we employ a Lorentz–Gauss fit [9] for the Lorentzian function occuring in expression (3.46). The Lorentz–Gauss fit has the representation

$$\frac{1}{\bar{\mathbf{K}}} = \frac{1}{k_0^2\theta_E^2}\frac{1}{1+\frac{\mathbf{q}^2}{k_0^2\theta_E^2}} = \frac{1}{k_0^2\theta_E^2}\sum_{j=1}^{N_{LG}} C_j \mathrm{e}^{-D_j\frac{\mathbf{q}^2}{k_0^2\theta_E^2}} . \tag{3.52}$$

It yields an alternative but less accurate formula for the inelastic scattering cross section

$$\sigma_{in} = \frac{\pi}{Z}\left(\frac{2\gamma}{a_H}\right)^2 \frac{1}{k_0^4\theta_E^2}\sum_{i,j=1}^{N_{LG}} C_i C_j \left[\frac{Z^2}{D_i+D_j} - \sum_{m,n=1}^{N_{DT}} \frac{A_m A_n \mathrm{e}^{-\theta_E^2 k_0^2(B_m+B_n)}}{D_i+D_j+k_0^2\theta_E^2(B_m+B_n)}\right] . \tag{3.53}$$

It should be noted that the number of terms in the equations (3.51) and (3.53) can be reduced considerably if we do not fit the atomic form factor $F(\mathbf{K})$ and/or the Lorentzian function $1/\bar{\mathbf{K}}^2$ by a sum of Gaussian function, but fit their squares. The results of this modification are very similar to the formulas presented above, only the number of terms is reduced at least from N_{DT}^2 to N_{DT} and from $N_{LG}^2 N_{DT}^2$ to $N_{LG}N_{DT}$, respectively.

Owing to the factor $1/(\theta^2+\theta_E^2)^2$ in the expression (3.47), the inelastic scattering cross section is significantly more peaked in forward direction than the elastic scattering cross section. The effect of the spatial delocalization d_i in an electron micrograph due to inelastic scattering is often discussed in terms of the characteristic angle θ_E of inelastic scattering. However, it should be emphasized that the simple conclusion $d_i = 0.6\,\lambda/\theta_e$ is erroneous. From (3.47) we find that only about 50 percent of the inelastically scattered electrons are actually contained in a forward cone with half–angle θ_E. The other half contains spatial information with much higher resolution and, therefore, diminishes the delocalization considerably [26].

Chapter 4

Mutual object spectrum

The illumination in a real electron microscope is never perfectly coherent. Coherent illumination would require a monochromatic point source. A modern field–emission gun equipped with a monochromator fulfills these requirements only to a certain extent. The finite energy width, the lateral extension of any real source, and the incoherent perturbations resulting from electromagnetic and mechanical instabilities during the time of exposure reduce both the degree of coherence of the electron wave and the information limit of the instrument.

The inelastic interaction between the imaging electrons and the object poses another source of incoherence but this must not be considered as a factor limiting the retrievable information. On the contrary, the inelastically scattered electrons provide very sensitive analytical information about the chemical composition and even the local electronic structure of the object. Moreover, the inelastically scattered electrons also carry some spatial information because they form low–resolution images. Electrons which are scattered elastically and inelastically even contain high–resolution spatial information. This fundamental fact is often termed as the conservation of the elastic contrast in inelastic electron imaging.

In chapter 2 we have shown that the quantum–mechanical state of the scattered electron is not completely described by the wave function of a pure quantum state. Accordingly, we have to consider the total state of the imaging electron and of the object as a mixed quantum state. This situation is to some extent similar to that encountered for partially coherent imaging in light optics. Therefore, the concept of the light–optical mutual coherence function is very suitable to also account for the influence of inelastic scattering and partially coherent illumination in electron microscopy [28, 26, 43].

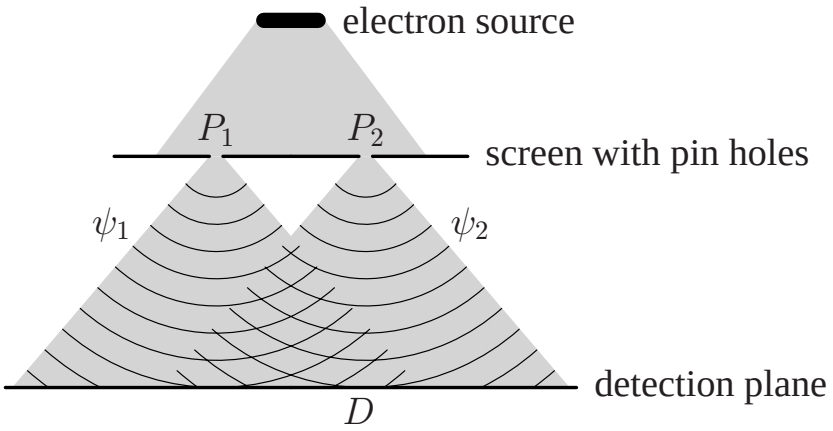

Figure 4.1: *Schematic arrangement illustrating the formation of partial coherence. The pinholes P_1 and P_2 are illuminated by an extended, incoherent source. The partial waves emanating from both pin holes form a partially coherent wave field. The interference patterns resulting from different points of the source superimpose incoherently. The lateral extension of the source can be used to adjust the degree of coherence of the wave field behind the screen.*

4.1 Mutual coherence function

The physical quantity recorded by the detector in an electron microscope is neither the quantum–mechanical wave function nor the scattering amplitude of the object but the z–component of the probability current density at the plane of detection perpendicular to the optic axis. The detector integrates the measured signal over the time of detection T. Therefore, the recorded image intensity is a time average. The probability current is related to a time–independent wave function only in the ideal case of elastic scattering and fully coherent illumination. In reality microscopic fluctuations within the object, the source, and the optical instrument during the time of exposure have influence on the detected image signal. The frequency of these fluctuations is much higher than the reciprocal time of detection $1/T$. If we neglect subsidiary effects like object damage and object heating, the time variation of the current density can be described by a stationary stochastic process. The probability amplitudes at two points $\mathbf{r}_1$ and $\mathbf{r}_2$ in free space are given by the time–dependent functions $\psi_1 = \psi(\mathbf{r}_1, t)$ and $\psi_2 = \psi(\mathbf{r}_2, t)$, respectively. The time averaged signal at another point $\mathbf{r}_D$ results from the superposition of the partial waves emanating from the points $\mathbf{r}_1$ and $\mathbf{r}_2$ as illustrated in figure 4.1. To account for the propagation of the partial waves between their points of origin $\mathbf{r}_1$ and $\mathbf{r}_2$ and the point of detection $\mathbf{r}_D$ we introduce the complex constants C_1 and C_2. The recorded intensity at the point of detection $\mathbf{r}_D$ is then given by

$$I_D = |C_1|^2 \langle \psi_1^* \psi_1 \rangle_T + |C_2|^2 \langle \psi_2^* \psi_2 \rangle_T + 2\, Re\, \{ C_1^* C_2 \langle \psi_1^* \psi_2 \rangle_T \} \ . \tag{4.1}$$

The symbol $\langle \ldots \rangle_T$ indicates the time average taken over the time of detection T and Re denotes the real part of the expression. The third term in expression (4.1) is propor-

tional to the correlation of the temporal variations of the probability amplitude at the positions $\mathbf{r}_1$ and $\mathbf{r}_2$. It disappears for sufficiently long detection times for completely uncorrelated sources in $\mathbf{r}_1$ and $\mathbf{r}_2$ and becomes maximal for full correlation between the partial waves emanating from the two pin holes [35].

The setup discussed above represents a largely simplified version of an electron imaging experiment. It demonstrates that the concept of partial coherence accounts for the correlation between distinct points in the wave field. This correlation is described most conveniently by the mutual coherence function

$$\Gamma = \Gamma(\mathbf{r}, \mathbf{r}', \tau) = \langle \psi^*(\mathbf{r}, t)\psi(\mathbf{r}', t-\tau)\rangle_T \ . \tag{4.2}$$

This function allows the calculation the time–averaged image intensity in the plane of detection. Owing to the stationarity of the imaging process, Γ depends only on the time difference $\tau = t - t'$ and not on the absolute time. Quantum–mechanically the time average corresponds to an average over the internal degrees of freedom of the total system and simultaneously to an ensemble average over differently prepared initial states.

The complex–valued mutual coherence function (4.2) is a bilinear, and hermitian time average of the wave function evaluated at two different points in space and time. Hence, the physical laws governing the propagation and the transmission of the mutual coherence function are closely related to that of ordinary wave functions. Although the mutual coherence function does not contain the complete information about the wave function $\psi = \psi(\mathbf{r}, t)$, it carries all information necessary to describe the image formation. Accordingly, the time averages of both the electron intensity and the z–component of the probability current can be expressed in terms of the mutual coherence function

$$\begin{aligned} j_z(\mathbf{r}) &= \frac{\hbar}{m}\, Im \left\{ \frac{\partial}{\partial z'} \Gamma(\mathbf{r}, \mathbf{r}', \tau = 0) \right\} \Bigg|_{\mathbf{r}=\mathbf{r}'} \ , \\ I(\mathbf{r}) &= \langle \psi(\mathbf{r}, t)\psi^*(\mathbf{r}', t)\rangle_T = \Gamma(\mathbf{r}, \mathbf{r}' = \mathbf{r}, \tau = 0) \ , \end{aligned} \tag{4.3}$$

where Im denotes the imaginary part. The Fourier transform of the mutual coherence function

$$\Gamma(\mathbf{r}, \mathbf{r}', \omega) = \frac{1}{\sqrt{2\pi}} \int \Gamma(\mathbf{r}, \mathbf{r}', \tau)\ \mathrm{e}^{i\omega\tau} d\tau \tag{4.4}$$

with respect to the time lag τ is called the mutual spectral density of the wave field.

4.2 Free–space propagation

The free–space propagation of the mutual coherence function is governed by the stationary Schrödinger–equation. The relative energy width of the electrons in a high–resolution electron microscope is very small, even if inelastic scattering is taken

into account. Therefore, we consider a quasi–monochromatic wave field emanating from an extended incoherent source. The corresponding mutual coherence function $\Gamma(\mathbf{r}_A, \mathbf{r}'_A, \tau)$ is assumed to be known for all pairs of points $(\mathbf{r}_A, \mathbf{r}'_A)$ in a plane $z = z_A$ perpendicular to the optic axis. In this case the mutual coherence function at any subsequent plane $z = z_B$ in the field–free region behind the plane z_A can be determined by employing Sommerfeld's diffraction formula [35]

$$\begin{aligned}\Gamma(\mathbf{r}_B, \mathbf{r}'_B, \tau) &= \left(\frac{k}{2\pi}\right)^2 \int\int \Gamma(\mathbf{r}_A, \mathbf{r}'_A, \tau) \\ &\times \frac{\exp\left(ik|\mathbf{r}_B - \mathbf{r}_A|\right)}{|\mathbf{r}_B - \mathbf{r}_A|} \frac{\exp\left(-ik|\mathbf{r}'_B - \mathbf{r}'_A|\right)}{|\mathbf{r}'_B - \mathbf{r}'_A|}\, d^2\mathbf{r}_A d^2\mathbf{r}'_A\,.\end{aligned} \tag{4.5}$$

The wave number k corresponds to the mean energy of the imaging electrons. This integral equation neglects retardation effects caused by different geometrical distances and the consequences of large inclination angles. Nevertheless, this approximation describes the propagation of the mutual coherence function sufficiently accurate within the field–free region. In an electron microscope the electron beam is confined to a narrow region about the optic axis. In this case we can expand the distance

$$\begin{aligned}|\mathbf{r}_B - \mathbf{r}_A| &= \sqrt{(\rho_B - \rho_A)^2 + (z_B - z_A)^2} \\ &\approx |z_B - z_A| \left(1 + \frac{1}{2}\frac{(\rho_B - \rho_A)^2}{(z_B - z_A)^2} + \ldots\right)\end{aligned} \tag{4.6}$$

in a power series with respect to the lateral distance of $|\rho_B - \rho_A|$. Since the planes z_A and z_B are parallel to each other, we only need information about the correlation between different lateral positions. Therefore, Γ reduces to a four–dimensional correlation function $\Gamma(\rho, \rho', \tau; z) = \Gamma(\mathbf{r}, \mathbf{r}', \tau)|_{z=z'}$ with the z coordinate as a parameter. The dependence of $\Gamma(\rho, \rho', \tau; z)$ on ρ and ρ' accounts for the lateral coherence and the dependence on the time difference τ describes the longitudinal or temporal coherence of the wave field. The definition of the axial coordinates is sketched in figure 4.2.

Considering only terms up to second order in the expansion (4.6), we obtain an approximation for the free–space propagation between the two parallel planes, a distance $d = z_B - z_A$ apart

$$\begin{aligned}\Gamma(\rho_B, \rho'_B, \tau; z_B) &= \left(\frac{k}{2\pi d}\right)^2 \int\int \Gamma(\rho_A, \rho'_A, \tau; z_A) \\ &\times \exp\left(\frac{ik}{2d}\left((\rho_B - \rho_A)^2 - (\rho'_B - \rho'_A)^2\right)\right)\, d^2\rho_A\, d^2\rho'_A\end{aligned} \tag{4.7}$$

in complete analogy to the Fresnel approximation in light optics. However, due to the quantum nature of the electrons, we cannot directly apply the light–optical theory of image formation under partially coherent illumination conditions to imaging with electrons.

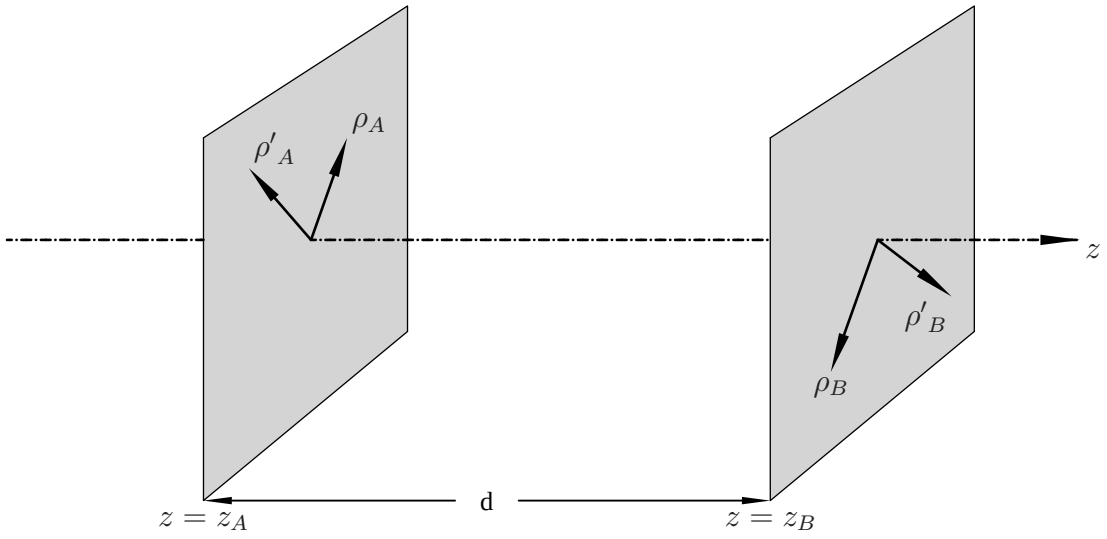

Figure 4.2: *Sketch of the axial coordinate system used for the definition of the paraxial propagation of the mutual coherence function along the optic axis.*

The right–hand side of equation (4.7) describes a linear mapping of the mutual coherence function from the plane $z = z_A$ onto the plane $z = z_B$. It can be read as a convolution of a propagator function P_F with the mutual coherence function at the initial plane A. The four–dimensional free–space propagator

$$P_F(\rho, \rho'; d) = \left(\frac{k}{2\pi d}\right)^2 \exp\left(i\frac{k}{2d}\left(\rho^2 - \rho'^2\right)\right) \tag{4.8}$$

breaks down into a product of two two–dimensional Fresnel propagators.

The Fresnel approximation describes the real free–space propagation in electron imaging surprisingly well even for small distances d. To understand this behaviour, we consider a high–energy electron moving in the direction of $\mathbf{k}$. Its spatial wave function fulfills the three–dimensional Helmholtz equation

$$\Delta\,\psi + \mathbf{k}^2\,\psi = 0. \tag{4.9}$$

The z dependence of ψ can be expressed as a slightly distorted plane wave

$$\psi(\rho, z) = \exp(ikz)\;\tilde{\psi}(\rho, z)\;. \tag{4.10}$$

Inserting this ansatz into the differential equation (4.9) and considering that $\tilde{\psi}(\rho, z)$ changes only slowly over a distance of several wave lengths, we obtain the approximation

$$\Delta_\rho\,\tilde{\psi} + 2ik\;\partial_z\,\tilde{\psi} = 0\;. \tag{4.11}$$

This differential equation is the high–energy approximation of the Schrödinger equation. It neglects backscattering and corresponds to the two–dimensional diffusion equation with a complex diffusion coefficient. By employing the Green function technique, we find the solution

$$\begin{aligned} \psi(\rho_B, z_B) &= -\frac{ik}{2\pi d}\, \exp\left(ik(z_B - z_A)\right) \\ &\quad \times \int \psi(\rho_A, z_A)\, \exp\left(i\frac{k}{2d}\left(\rho_B - \rho_A\right)^2\right)\, d^2\rho_A \ . \end{aligned} \tag{4.12}$$

The comparison of this result with equation (4.7) shows that the Fresnel approximation is an exact solution of the Schrödinger equation in high–energy approximation.

If $\Gamma = \Gamma(\rho_A, \rho'_A, \tau; z_A)$ vanishes in the plane z_A outside the central region with maximum diameter D_A, the Fresnel approximation of the mutual coherence function at distances $d > D_A^2/\lambda$ from the initial plane z_A can be replaced by the Fraunhofer approximation [35, 33]

$$\begin{aligned} \Gamma(\rho_B, \rho'_B, \tau; z_B) &= \left(\frac{k}{2\pi d}\right)^2 \exp\left(i\frac{k}{2d}\left(\rho_B^2 - \rho'^2_B\right)\right) \\ &\quad \times \int\int \Gamma(\rho_A, \rho'_A, \tau; z) \exp\left(-i\frac{k}{d}\left(\rho_B\rho_A - \rho'_B\rho'_A\right)\right)\, d^2\rho_A\, d^2\rho_A \ . \end{aligned} \tag{4.13}$$

Apart from a phase factor this approximation relates the mutual coherence function at the successive planes by a Fourier transformation with respect to both lateral coordinates. This approximation becomes exact if the distance d between the successive planes effectively approaches infinity.

4.3 Characterization of the source

A real electron source is characterized by an extended region of emission and a finite energy width. The energy distribution can be measured by the half width of full maximum (hwfm) δE. Each real electron source emits electrons from an extended region of its surface. Since the wave of an outgoing electron extends over a finite region of this surface, we cannot consider the individual points of the real surface of the cathode as incoherent point sources. Instead of the physical source the virtual or real crossover is considered as the effective source. In the case of a field–emission source the effective source is the smallest spot formed by the asymptotes of the trajectories which the electrons have in front of the anode. The effective source is roughly located at the center of curvature of the tip. The individual points $\mathbf{r}_S$ of this effective source can be considered as incoherent with respect to each other. Moreover, we assume that the energy distribution of the emitted electrons does not depend on the position $\mathbf{r}_S$ of the

source point. Accordingly, the correlation function Γ_S can be written as

$$\Gamma_S(\mathbf{r}_S, \mathbf{r}'_S; \omega) = \Gamma(\mathbf{r}_S, \mathbf{r}'_S)\; p(\omega)\;. \tag{4.14}$$

From equation (4.4) we find that under this assumption $\Gamma_c(\mathbf{r}, \mathbf{r}', \tau) = \Gamma(\mathbf{r}, \mathbf{r}')\; g(\tau)$ also factorizes, where the first factor depends on the spatial coordinates and the second solely on τ. The function $g(\tau)$ is the Fourier–transform of the spectral density $p(\omega)$ with respect to ω. The spectral density function $p(\omega)$ of most cathodes can be approximated with a sufficient degree of accuracy by a Gaussian distribution

$$p(\omega) = \frac{1}{\sqrt{2\pi}\Delta\omega}\; \mathrm{e}^{-\frac{(\omega-\omega_a)^2}{2\Delta\omega^2}}\;, \tag{4.15}$$

where $\hbar\Delta\omega = \delta E/(2\sqrt{2\ln 2})$. The mean energy $\hbar\omega_a = eU$ is defined by the nominal acceleration voltage U.

Since partial waves emanating from different points of the effective source are considered incoherent with respect to each other, the mutual intensity function on the surface of the effective source is given by the relation

$$\Gamma(\mathbf{r}_S, \mathbf{r}'_S) = I_S(\mathbf{r}_S)\; \delta(\mathbf{r}_S - \mathbf{r}'_S)\;. \tag{4.16}$$

The function $I_S(\mathbf{r})$ is the normalized intensity of the effective source. By employing formula (4.5) with $\Lambda = \Lambda' = 1$ for the propagation of the mutual intensity and neglecting retardation effects, we obtain the mutual intensity at an arbitrary plane behind the effective source

$$\Gamma(\mathbf{r}, \mathbf{r}') = \left(\frac{k}{2\pi}\right)^2 \int_S I(\mathbf{r}_S)\, \frac{\exp ik(|\mathbf{r} - \mathbf{r}_S| - |\mathbf{r}' - \mathbf{r}_S|)}{|\mathbf{r} - \mathbf{r}_S||\mathbf{r}' - \mathbf{r}_S|}\; d^2\mathbf{r}_S\;. \tag{4.17}$$

The light–optical analogue of this formula is known as the Van–Cittert–Zernike theorem.

For most applications it suffices to assume a plane effective source with a Gaussian spatial distribution

$$I(\mathbf{r}_S) = I(\rho_S) = \frac{I_0}{2\pi\sigma^2}\mathrm{e}^{-\frac{\rho_S^2}{2\sigma^2}}\;. \tag{4.18}$$

The variance σ^2 defines the mean area of emission of the effective source. Using this assumption together with the Fresnel approximation, we eventually find from (4.17) for the mutual intensity at the plane $z = z_s + d$ the analytical expression

$$\Gamma(\rho, \rho') = I_0\; \left(\frac{k}{2\pi d}\right)^2 \mathrm{e}^{-\frac{k^2\sigma^2}{2d^2}(\rho-\rho')^2} \mathrm{e}^{i\frac{k}{2d}(\rho^2 - \rho'^2)}\;. \tag{4.19}$$

In this approximation the intensity $I(\rho) = \Gamma(\rho, \rho)$ is constant within the paraxial domain about the optic axis and decreases quadratically with the axial distance d. From equation (4.19) we find that the mutual intensity of an incoherent source is sharply peaked for $\rho = \rho'$. Only in the borderline case of a very small effective source with $k\,\sigma \ll 1$ is the wave field coherent in the paraxial region.

4.4 Mutual object spectrum

The four–dimensional Fresnel propagator cannot be used to describe the propagation of the electron wave through the lens system or through the object since the electromagnetic field acts as an inhomogeneous and anisotropic refracting medium on the imaging electrons. Nevertheless, the mutual coherence function behind the object is linearly connected to the mutual coherence function in front of the object. The map between the entrance and the exit plane can be described quite generally by the mutual object spectrum $T = T(\mathbf{q}_i, \mathbf{q'}_i, \mathbf{q}_f, \mathbf{q'}_f, z_i, z_f, \tau)$. This function depends mutually on the primed and unprimed coordinates and connects the mutual coherence function in front of the object with that behind the object via the relation

$$\Gamma(\mathbf{q}_f, \mathbf{q'}_f, \tau; z_B) = P_F(\mathbf{q}_f, \mathbf{q'}_f; D/2) \int T(\mathbf{q}_i, \mathbf{q'}_i, \mathbf{q}_f, \mathbf{q'}_f, \tau) \times P_F(\mathbf{q}_i, \mathbf{q'}_i; D/2)\, \Gamma(\mathbf{q}_i, \mathbf{q'}_i, \tau; z_A)\, d^2\mathbf{q}_i\, d^2\mathbf{q'}_i\ . \tag{4.20}$$

The functions

$$\Gamma(\mathbf{q}, \mathbf{q}', \tau) = \frac{1}{(2\pi)^2} \int \Gamma(\rho, \rho', \tau)\ \exp\left(-i\mathbf{q}\rho + i\mathbf{q}'\rho'\right)\ d^2\rho\, d^2\rho'\ , \tag{4.21}$$

and

$$P_F(\mathbf{q}, \mathbf{q}'; d) = \exp\left(-\frac{id}{2k}\left(\mathbf{q}^2 - \mathbf{q}'^2\right)\right) \tag{4.22}$$

denote the four–dimensional Fourier transforms of the mutual coherence function and of the Fresnel propagator (4.8), respectively.

The relation (4.20) is based on the assumption that the object is situated between the planes $z = z_A$ and $z = z_B$, as depicted in figure 4.3. For a thick object it is crucial to differentiate between the object plane $z = z_O$, the entrance plane $z = z_A$, and the exit plane $z = z_B$. For simplicity we choose the central plane of the object as the object plane. For a very thin object the thickness $D = z_B - z_A$ is negligibly small and hence the three planes are approximately equivalent.

Equation (4.20) only holds true within the frame of validity of the small–angle approximation. For large scattering angles the mutual object spectrum depends on the three–dimensional incident and the final scattering vectors $\mathbf{k}_i$, $\mathbf{k}'_i$, $\mathbf{k}_f$, and $\mathbf{k}'_f$ and not only on their lateral projections. In this more general case the mutual object spectrum $T = T(\mathbf{k}_i, \mathbf{k}'_i, \mathbf{k}_f, \mathbf{k}'_f, \tau)$ considers backscattering and connects the full six–fold spatial Fourier transform of the mutual coherence function behind the object with that in front of the object. Accordingly, the theory of image formation described in terms of the mutual object transparency is, at least in principle, not restricted to small scattering angles [8].

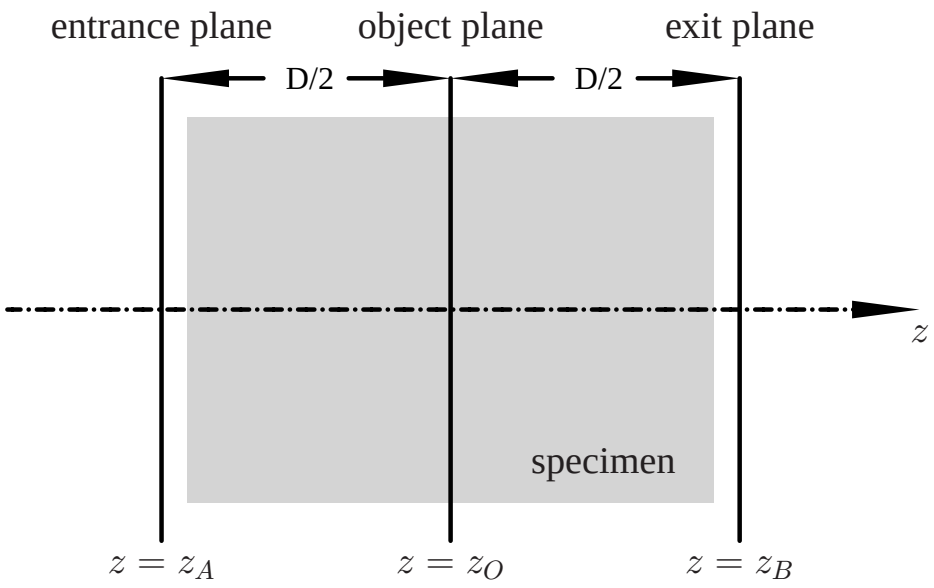

Figure 4.3: *Definition of the object plane $z = z_O$, the entrance plane $z = z_A$, and the exit plane $z = z_B$ for an object with thickness $D = z_B - z_A$. The object plane is situated in the center of the object $z_O = (z_A + z_B)/2$.*

If the influence of partial coherence and inelastic scattering is neglected the transfer function (4.20) decomposes into a product of two functions, such that one depends only on the primed and the other only on the unprimed coordinates. It should be noted that equation (4.20) is only applicable if the stochastical fluctuations of the wave function in front of the object and those of the object state are uncorrelated. Fortunately, this is the case in high–resolution electron imaging where backscattering can be neglected.

In order to derive an explicit expression for the mutual object spectrum in terms of the scattering amplitudes of the object we assume that the object is illuminated by a coherent superposition of slightly tilted plane waves. Accordingly, the initial mutual coherence function in front of the object adopts the simple form

$$\Gamma(\rho, \rho', \tau, z_A) = \exp(i\omega\tau)\ \exp(-i\mathbf{q}_i(\rho - \rho'))\ , \quad \tau = t - t'\ , \tag{4.23}$$

where $\omega = eU/\hbar$ is determined by the mean acceleration voltage U.

In the case of parallel illumination with direction of incidence $\mathbf{k}_i = \mathbf{q}_i + k_0(1 - \frac{\mathbf{q}_i^2}{2k_0^2})\mathbf{e}_z$, $|\mathbf{k}_i| \approx k_0$ for the z–component of the probability current density at a distance far

behind the object is given by

$$j_z(\mathbf{r}) = \frac{\hbar k_0}{m}\left\{1 + 2\ Re\left\{f_{00}(\mathbf{k}_i, \frac{\mathbf{r}}{r})\ \frac{\exp i(k_0 r - \mathbf{k}_i\mathbf{r})}{r}\right\} + \sum_{n=0}^{\infty}\frac{k_n}{k_0}\ \frac{|f_{0n}(\mathbf{k}_i, \frac{\mathbf{r}}{r})|^2}{r^2}\right\} . \tag{4.24}$$

This representation can be derived by using the expression (4.3) and the definition (3.1) of the scattering amplitude. The origin of the coordinate system is situated at the object plane on the optic axis. Within the paraxial domain the spherical wave in the second and third term of equation (4.24) may be approximated by the Fresnel propagator (4.7). Moreover, the wave number k_0 can be substituted for k_n, $n = 1, 2, \ldots$, because the relevant energy losses are small compared to the mean beam energy eU. Within the frame of validity of this approximation the z–component of the current density (4.3) is proportional to the diagonal elements of the mutual coherence function

$$j_z(\rho, \tau; z) \approx \frac{\hbar k_0}{m}\Gamma(\rho, \rho' = \rho, \tau; z) . \tag{4.25}$$

This result and the Fresnel approximation (4.13) for the wave function at a far distance from the object allow the calculation of the mutual coherence function at the object plane $z = z_O$ for a thick object. Using the expression (4.23) for the mutual coherence function in front of the object and the assumption that the object is in its ground state before the scattering takes place, we eventually find for the Fourier transform of the mutual coherence function at the object plane

$$\begin{aligned}\Gamma_f(\mathbf{q}, \mathbf{q}', \tau; z_O) \;=\; & \exp(i\omega\tau)\Big[\delta(\mathbf{q} - \mathbf{q}_i)\delta(\mathbf{q}' - \mathbf{q}_i) \\ & -\frac{1}{2\pi i k_0}\delta(\mathbf{q}' - \mathbf{q}_i) f_{00}^*(\mathbf{q}, \mathbf{q}_i) + \frac{1}{2\pi i k_0}\delta(\mathbf{q} - \mathbf{q}_i) f_{00}(\mathbf{q}', \mathbf{q}_i) \\ & +\frac{1}{4\pi^2 k_0^2}\sum_{n=0}^{\infty} f_{n0}^*(\mathbf{q}, \mathbf{q}_i) f_{n0}(\mathbf{q}', \mathbf{q}_i)\ \exp(-i\omega_{n0}\tau)\Big] .\end{aligned} \tag{4.26}$$

The rather lengthy calculation leading to this equation is outlined in appendix C. In the case of partially coherent illumination, we must replace the hermite product of the initial wave function (4.23) by a more general initial mutual coherence function.

If backscattering is neglected the stochastical fluctuations of the wave function in front of the object and within the object are uncorrelated and the thermal average over different initial object states can be performed independently. Hence the resulting expression

for the mutual object spectrum can be written as

$$\begin{aligned} T(\mathbf{q}_A, \mathbf{q'}_A, \mathbf{q}_B, \mathbf{q'}_B, \omega) &= \sum_{m=0}^{\infty} P_m \Big[\delta(\mathbf{q}_B - \mathbf{q}_A)\delta(\mathbf{q'}_B - \mathbf{q'}_A)\delta(\omega) \\ &- \frac{1}{2\pi i k_0}\delta(\mathbf{q'}_A - \mathbf{q'}_B) f^*_{mm}(\mathbf{q}_A, \mathbf{q}_B)\delta(\omega) + \frac{1}{2\pi i k_0}\delta(\mathbf{q}_A - \mathbf{q}_B) f_{mm}(\mathbf{q'}_A, \mathbf{q'}_B)\delta(\omega) \\ &+ \frac{1}{4\pi^2 k_0^2}\sum_{n=0}^{\infty} f^*_{nm}(\mathbf{q}_A, \mathbf{q}_B) f_{nm}(\mathbf{q'}_A, \mathbf{q'}_B)\delta(\omega - \omega_{nm}) \Big] \, . \end{aligned} \tag{4.27}$$

This result is obtained by comparing equation (4.26) with the more general equation (4.20) and then taking the thermal average with respect to the initial state of the object. Thereafter we performed the Fourier transformation with respect to the time lag τ. The argument of the resulting delta functions considers the discrete energy losses of the scattered electron caused by specific excitations of the object.

The representation (4.20) of the mutual object transparency elucidates the different nature of the two averaging processes. The thermal average over the possible initial states with probability P_m is an incoherent average and the summation over all final states of the object is a coherent average. The mutual object spectrum completely describes the influence of a thick object on the coherence function. It depends on the position coordinates at the object plane and on the direction of incidence. The latter dependence is caused by the strong dynamic effects in electron imaging due to multiple scattering. Equation (4.27) clearly demonstrates that a factorization of the mutual object transparency is impossible because partial coherence causes time correlations between different off–axial points. Primarily this correlation carries the information about the inelastic interaction between the imaging electrons and the object.

The mutual object spectrum (4.27) can be written as a sum of four different contributions

$$T = T_0 + T_1 + T_{2,el} + T_{2,in}. \tag{4.28}$$

The first term, which accounts for the unscattered part of the wave function forms the central spot in the diffraction pattern. In the absence of an object this is the only non–vanishing contribution

$$T = T_0 = \delta(\mathbf{q}_f - \mathbf{q}_i)\ \delta(\mathbf{q'}_f - \mathbf{q'}_i)\ \delta(\omega)\ . \tag{4.29}$$

This condition guarantees that the wave vector of an outgoing plane wave coincides with that of the corresponding incident plane wave. The second term

$$T_1 = -\frac{1}{2\pi i k_0}\sum_{m=0}^{\infty} P_m \left[\delta(\mathbf{q'}_A - \mathbf{q'}_B) f^*_{mm}(\mathbf{q}_A, \mathbf{q}_B) - \delta(\mathbf{q}_A - \mathbf{q}_B) f_{mm}(\mathbf{q'}_A, \mathbf{q'}_B)\right] \delta(\omega) \tag{4.30}$$

is linear in the scattering amplitudes and results from elastic scattering at an thermally averaged object potential. Inelastic scattering does not contribute linearly to the mutual coherence function. Hence the linear theory of image formation must neglect inelastic scattering in order to be consistent in its approximations. The thermal average accounts for thermal diffuse scattering and modifies the elastic scattering amplitude by a Debye–Waller factor, even if the quadratic terms are neglected. The last two terms

$$\begin{aligned} T_{2,el} &= \frac{1}{4\pi^2 k_0^2} \sum_{m=0}^{\infty} P_m f^*_{mm}(\mathbf{q}_A, \mathbf{q}_B) f_{mm}(\mathbf{q'}_A, \mathbf{q'}_B) \delta(\omega) \\ T_{2,in} &= \frac{1}{4\pi^2 k_0^2} \sum_{m=0}^{\infty} \sum_{\substack{n=0 \\ n\neq m}}^{\infty} P_m f^*_{nm}(\mathbf{q}_A, \mathbf{q}_B) f_{nm}(\mathbf{q'}_A, \mathbf{q'}_B) \delta(\omega - \omega_{nm}) \end{aligned} \quad (4.31)$$

of the right–hand side of equation (4.20) consider the contributions which are quadratic in the scattering amplitudes. Contrary to the linear part these contributions are affected by partially coherent imaging conditions and inelastic processes.

The mutual object transparency is not invariant with respect to an exchange of the initial and final scattering vectors. This behaviour is caused by plural scattering and known from experiments as the top–bottom effect. In particular details at the exit surface of thick specimens facing the objective lens are imaged with better resolution than those located on the opposite surface. By inserting the expression (4.29) for the first term T_0 into the equation (4.20) and by considering that two consecutive Fresnel propagator are equivalent to a single propagation, we can show that in the absence of an object the entrance and the exit planes are connected by a simple Fresnel propagation.

If inelastic scattering is considered it is impossible to rewrite the mutual object transparency as a product of two factors one depending only on the primed and the other only on the unprimed lateral position vector. Unfortunately, analytical expressions for the mutual object spectrum do not exist for realistic objects. Nevertheless, in chapter 5 we will present a general and quite efficient procedure to evaluate equation (4.27) for realistic objects numerically.

4.5 Mixed–dynamic form factor

Owing to the extremely large number of internal degrees of freedom it is not possible to explicitly calculate the exact mutual object spectrum for any realistic object. Unfortunately, the representation (4.28) of the mutual object spectrum in terms of the scattering amplitudes only demonstrates its over-all structure. The numerical evaluation of this expression necessitates further approximations. For weakly scattering specimens it is possible to derive a second–order approximation with respect to the strength of the interaction potential. The linear part in the expression (4.30) is solely related to elastic scattering. Therefore, we must replace the elastic scattering amplitude by

its second–order Born approximation. Inelastic scattering does not contribute to the linear terms because the inelastically scattered partial waves cannot interfere with the unscattered wave due to the orthogonality of the final object states. Hence it suffices to use the first–order Born approximation for the inelastic scattering amplitudes in the quadratic terms of the expression (4.31). The resulting approximation of the mutual object transparency for weakly scattering objects

$$T^{(2)} = T^{(0)} + T^{(1)} + T^{(2)}_{\text{el,1}} + T^{(2)}_{\text{el,2}} + T^{(2)}_{\text{in}} \tag{4.32}$$

is consistent in second order with respect to the strength of the interaction potential [26, 8, 7].

The familiar weak phase–object approximation only explains the terms $T^{(0)}$ and $T^{(1)}$. Therefore, this approximation completely neglects the quadratic terms which contain the information about the electronic properties of the object. Hence the linear approximation can only describe the phase contrast of thin amorphous objects with a sufficient degree of accuracy. Inelastic scattering solely affects the quadratic terms $T^{(2)}_{\text{el,1}}$ and $T^{(2)}_{\text{in}}$. The second–order approximation describes the interaction of the incident electron wave with a thin object much better than the linear approximation because it considers the nonlinear dependence of the current density on the scattering amplitude. If we express the scattering amplitudes in (4.28) by the Born series and drop all terms of third– and higher–order in the interaction potential, we eventually obtain

$$\begin{aligned}
T^{(0)} &= \delta(\mathbf{K}_\perp)\,\delta(\mathbf{K}'_\perp)\delta(\omega)\;, \\
T^{(1)} &= \frac{1}{2\pi i k_0}\sum_{m=0}^{\infty} P_m\left[\delta(\mathbf{K}_\perp)\,f^{(1)*}_{mm}(\mathbf{K}') - \delta(\mathbf{K}'_\perp)\,f^{(1)}_{mm}(\mathbf{K})\right]\;\delta(\omega)\;, \\
T^{(2)}_{\text{el,1}} &= \frac{1}{2\pi i k_0}\sum_{m=0}^{\infty} P_m\left[\delta(\mathbf{K}_\perp)\,f^{(2)*}_{mm}(\mathbf{k}_f,\mathbf{k}_i) - \delta(\mathbf{K}'_\perp)\,f^{(2)}_{mm}(\mathbf{k}_f,\mathbf{k}_i)\right]\;\delta(\omega)\;, \\
T^{(2)}_{\text{el,2}} &= \frac{1}{4\pi^2 k_0^2}\sum_{m=0}^{\infty} P_m f^{(1)*}_{mm}(\mathbf{K})\,f^{(1)}_{mm}(\mathbf{K}')\;\delta(\omega)\;, \\
T^{(2)}_{\text{in}} &= \frac{1}{4\pi^2 k_0^2}\sum_{m=0}^{\infty}\sum_{\substack{n=0\\ n\neq m}}^{\infty} P_m f^{(1)*}_{nm}(\mathbf{K})\,f^{(1)}_{nm}(\mathbf{K}')\;\delta(\omega-\omega_{nm})\;,
\end{aligned} \tag{4.33}$$

where $\mathbf{K}_\perp$ denotes the lateral part of the scattering vector $\mathbf{K} = k_f - k_i$. It is important to note that the first–order Born approximation of the inelastic scattering amplitude suffices to correctly calculate the mutual object spectrum up to the second order [8, 7]. This does not hold for the elastic scattering amplitude which must be known up to the second–order Born approximation. Fortunately, the second–order contribution can readily be obtained from the integral relation (3.21).

Inelastic scattering results from electronic excitations and from thermal diffuse scattering. An electronic excitation is initiated by the scattering of an incident electron

at a bound electron of the object. Since the masses of both particles are equal, the scattering process is accompanied by a considerable energy transfer. Thermal diffuse scattering results from scattering at the potentials of the nuclei which oscillate about their positions of equilibrium. These vibrations always affect the intensity distribution in electron micrographs and diffraction patterns. The energy loss of the scattered electrons due to thermal diffuse scattering is very low. Therefore, it is not possible to separate the thermal diffusely scattered electrons from the unscattered and the elastically scattered electrons by means of an energy filter [2].

Within the frame of validity of the first–order Born approximation single inelastic scattering at an assembly of fixed atoms can conveniently be described by means of the mixed dynamic form factor. This quantity considers scattering at the electronic charge distribution of the specimen. The mixed dynamic form factor is defined by the thermal average of the Fourier transform of the electron density of the object [26]

$$S(\mathbf{K},\mathbf{K}',\omega) = \frac{1}{2\pi}\int_{-\infty}^{\infty} \langle \varrho(\mathbf{K},t)^* \varrho(\mathbf{K}',t-\tau)\rangle_T \exp(i\omega\tau)\; d\tau \; . \tag{4.34}$$

In this equation $\mathbf{K} = \mathbf{q}_f - \mathbf{q}_i - k_0\theta_E \mathbf{e}_z$ denotes the scattering vector which is connected with the energy loss ΔE via the characteristic angle θ_E for inelastic scattering (3.31). The Fourier transform of the electron density operator is given by

$$\varrho(\mathbf{K},t) = \sum_{j=1}^{Z} \exp\left(i\mathbf{K}\mathbf{R}_j(t)\right) \; , \tag{4.35}$$

where $\mathbf{R}_j(t)$, $j = 1,\ldots,Z$ denotes the time–dependent position operator in the Heisenberg representation of the jth object electron. The density operator (4.35) implicitly depends on the internal degrees of freedom of the object [4, 5].

Since the interaction between the incident particle and all constituents of the object is governed by the Coulomb potential, the quadratic contribution to the mutual object transparency can also be expressed by means of the mixed dynamic form factor. Considering that the electric potential of a point charge fulfills the Poisson equation we readily find

$$\int \frac{1}{|\mathbf{r}-\mathbf{R}|} \exp(-i\mathbf{K}\mathbf{r})\, d^3\mathbf{r} = \frac{4\pi}{\mathbf{K}^2} \exp(-i\mathbf{K}\mathbf{R}) \; . \tag{4.36}$$

for the Fourier transform of the Coulomb potential. The matrix elements of the time–dependent density operator fulfill the relation

$$\int \phi_n^*(\mathbf{R})\, \varrho(\mathbf{K},t-\tau)\, \phi_m(\mathbf{R})\, d^l\mathbf{R} = \exp(-i\omega_{nm}\tau) \int \phi_n^*(\mathbf{R})\, \varrho(\mathbf{K},t)\, \phi_m(\mathbf{R})\, d^l\mathbf{R} \tag{4.37}$$

with respect to the eigenfunctions of the object. Together with the Fourier representation of the Coulomb potential (4.36) equation (4.37) proves the relation [8]

$$\begin{aligned}
\frac{S(\mathbf{K},\mathbf{K}',\omega)}{\mathbf{K}^2\mathbf{K}'^2} &= \frac{1}{2\pi}\int_{-\infty}^{\infty}\frac{\langle\varrho^*(\mathbf{K},t)\varrho(\mathbf{K}',t-\tau)\rangle_T}{\mathbf{K}^2\mathbf{K}'^2}\,\exp\left(i\omega\tau\right)\,d\tau.\\
&= \frac{1}{2\pi}\frac{1}{\mathbf{K}^2\mathbf{K}'^2}\int_{-\infty}^{\infty}\exp\left(i\omega\tau\right)\sum_{m=0}^{\infty}\sum_{n=0}^{\infty}\\
&\int\phi_n^*(\mathbf{R})\varrho^*(\mathbf{K},t)\phi_m(\mathbf{R})\,d\mathbf{R}\int\phi_m^*(\mathbf{R}')\varrho(\mathbf{K}',t+\tau)\phi_n(\mathbf{R}')\,d\mathbf{R}'\,d\tau\\
&= \sum_{m=0}^{\infty}\sum_{n=0}^{\infty}P_m\;\delta(\omega-\omega_{nm})f_{nm}^{(1)*}(\mathbf{K})f_{nm}^{(1)}(\mathbf{K}')\\
&= \frac{k_0^2}{2\pi}T_{\text{in}}^{(2)}(\mathbf{K},\mathbf{K}',\omega)+\frac{k_0^2}{2\pi}T_{\text{el,2}}^{(2)}(\mathbf{K},\mathbf{K}',\omega)\;. \qquad (4.38)
\end{aligned}$$

With this result we can define the inelastic part of the mixed dynamic form factor by

$$\frac{2\pi}{k_0^2}\;S_{\text{in}}(\mathbf{K},\mathbf{K}',\omega)=\mathbf{K}^2\mathbf{K}'^2\;T_{\text{in}}^{(2)}(\mathbf{K},\mathbf{K}',\omega)\;. \qquad (4.39)$$

The mixed dynamic form factor is a generalization of the conventional dynamic form factor $S = S(\mathbf{K},\omega) = S(\mathbf{K},\mathbf{K}' = \mathbf{K},\omega)$. In contrast to the conventional dynamic form factor the mixed dynamic form factor is, in general, not a real quantity because it also contains information about the spatial structure of the object. Therefore, the mixed dynamic form factor is well suited to describe the image formation by the elastically and inelastically scattered electrons in the case of thin objects. Equation (4.38) shows that the mixed dynamic form factor is related to a density–density correlation function. The fact that the scattering properties of an object are determined by such a correlation function was first discovered by Van Hove [44]. The introduction of the mixed dynamic form factor generalizes this result to include the phases of the partial waves which carry the information about the atomic structure. Within the frame of validity of the second–order approximation (4.32) the result (4.38) shows that the inelastic electron scattering due to electronic excitations is proportional to the statistical fluctuation of the electron density within the specimen.

The double differential scattering cross section in first–order Born approximation can be expressed by the dynamic form factor as

$$\frac{d^2\sigma}{d\Omega\,dE}=\frac{4\gamma^2}{a_H^2}\frac{1}{\mathbf{K}^4}S(\mathbf{K},E/\hbar)\;, \qquad (4.40)$$

and hence the inelastic part of the dynamic form factor describes inelastic scattering. Starting from this relation we may derive a more descriptive interpretation of the mixed dynamic form factor. The scattering cross section only accounts for the current density

scattered into a distinct direction. The information about the relative phases and the coherence of the partial waves emanating in distinct directions is lost. Nevertheless, the correct description of the image intensity distribution relies entirely on this information. For simplicity we consider an object illuminated by a plane wave with wave vector $\mathbf{k}_i$. In addition we can decompose the scattered wave front emanating from the object into a sum of plane waves propagating in different directions. In the case of inelastic scattering these plane waves are partially coherent. The mixed dynamic form factor $S = S(\mathbf{k}_f - \mathbf{k}_i, \mathbf{k}'_f - \mathbf{k}_i, \omega)$ accounts for the degree of coherence existing between the plane waves which propagate in the directions $\mathbf{k}_f$ and $\mathbf{k}'_f$, respectively.

For a single atom we can approximately calculated the mixed dynamic form factor for inner shell excitations. To perform this task we need the matrix elements of the interaction potential (3.29) with respect to the electron eigenfunctions of the atom. It is possible to obtain these data by employing the central field approximation for electronic eigenfunctions. A less accurate but more efficient approach is to calculate the mixed dynamic form factor for a mean energy loss $\bar{E} = \hbar\bar{\omega}$. Although this approach cannot differentiate between different energy losses it describes the overall effect of inelastic scattering on the image intensity surprisingly well. This method is a generalization of the Raman–Compton approximation introduced in section 3.2. Within the frame of validity of this approximation the inelastic part of the mixed dynamic form factor of a single atom can be expressed by the atomic form factor $F = F(\mathbf{K})$ of the ground state electron density [26] as

$$S_{\text{in}}(\mathbf{K}, \mathbf{K}', \omega) = \left(F(\mathbf{K} - \mathbf{K}') - \frac{F(\mathbf{K})F(\mathbf{K}')}{Z} \right) \delta(\omega - \bar{\omega}) \; . \tag{4.41}$$

This approximation is reasonable as long as the resolution limit of the electron microscope exceeds the diameter of an atom. In the special case $\mathbf{K} = \mathbf{K}'$ the relations $F(0) = Z$ and (4.40) show that the expression (4.41) is consistent with the differential inelastic scattering cross section (3.46) for the Raman–Compton model. Since this approximation considers the atoms of the object as statistically uncorrelated, it does not account for collective excitations correctly. Nevertheless, the generalized Raman–Compton approximation is very suitable for the simulation of the image formation by inelastically scattered electrons.

For the Wentzel–Yukawa potential (3.24) we can derive an explicit formula for the inelastic part of the mixed dynamic form factor for a mean energy loss $\bar{\omega}$ in small angle approximation. By substituting the atomic form factor of the Wentzel Potential into (4.41) we find

$$\begin{aligned} S_{\text{in}}(\mathbf{q}, \mathbf{q}', \omega) \;\; &= \;\; \left(\frac{2\gamma}{a_H} \right)^2 Z \frac{1}{\mathbf{q}^2 + k_0^2\theta_E^2} \frac{1}{\mathbf{q}'^2 + k_0^2\theta_E^2} \, \delta(\omega - \bar{\omega}) \\ &\times \left[\frac{k_0^2\theta_0^2}{(\mathbf{q} - \mathbf{q}')^2 + \theta_0^2 k_0^2} - \frac{k_0^2\theta_0^2}{\mathbf{q}^2 + k_0^2\theta_0^2 + k_0^2\theta_E^2} \, \frac{k_0^2\theta_0^2}{\mathbf{q}'^2 + k_0^2\theta_0^2 + k_0^2\theta_E^2} \right] , \end{aligned} \tag{4.42}$$

where $\mathbf{q}$ denotes the two–dimensional lateral scattering vector. For a small energy loss the relation $\theta_E \ll \theta_0$ holds and equation (4.42) adopts the form

$$S_{\text{in}}(\mathbf{q},\mathbf{q}',\omega) = \left(\frac{2\gamma}{a_H}\right)^2 Z \frac{1}{\mathbf{q}^2+k_0^2\theta_E^2}\frac{1}{\mathbf{q}'^2+k_0^2\theta_E^2}\,\delta(\omega-\bar{\omega}) \times\left[\frac{\theta_0^2}{(\boldsymbol{\theta}-\boldsymbol{\theta}')^2+\theta_0^2}-\frac{\theta_0^4}{(\boldsymbol{\theta}^2+\theta_0^2)(\boldsymbol{\theta}'^2+\theta_0^2)}\left[1-\theta_E^2\,\frac{\boldsymbol{\theta}^2+\boldsymbol{\theta}'^2+2\theta_0^2}{(\boldsymbol{\theta}^2+\theta_0^2)(\boldsymbol{\theta}'^2+\theta_0^2)}\right]\right]\,.$$

This result illustrates that a small finite value of θ_E prevents the differential scattering cross section

$$\left.\frac{d\sigma}{d\Omega}\right|_{\mathbf{q}=0} = \int_{-\infty}^{\infty} S(0,0,\omega)\,d\omega = \left(\frac{2\gamma}{a_H k_0^2}\right)^2 \frac{2Z}{\theta_E^2\theta_0^2} \tag{4.43}$$

from diverging in forward direction.

Chapter 5

Coherence function multislice

The first–order Born approximation assumes that each layer of the object is illuminated by the undistorted initial wave. However, in the case of electron scattering this assumption proves invalid for most relevant specimens.

The initial energy of the imaging electrons in transmission electron microscopy is well above 60 keV. The average energy loss resulting from single electronic excitations is below 1 keV. Moreover, backscattering effects can be neglected because the electrons are dominantly scattered in forward direction. The propagation of the electron wave through a very thin object can be described with a sufficient degree of accuracy by means of the Glauber high–energy approximation [6]. The range of validity of this approximation is larger than that of the first–order Born approximation because the high–energy approximation satisfies the optical theorem. In order to include inelastic scattering we must generalize the conventional Glauber formalism by considering objects with internal degrees of freedom [8]. By combining this approach with the multislice formalism, we obtain an explicit representation of the mutual object spectrum for a thick object in terms of the object potential. Since this formulation accounts for multiple scattering, it correctly describes the influence of elastic and inelastic scattering on the image formation.

5.1 High–energy approximation

To determine the coherence function we employ the quantum–mechanical interaction representation and assume that the dynamics of the object is completely known. The interaction representation is well suited for handling interacting systems if only the properties of one of the systems are of interest. In our case this is the probability current of the transmitted electrons behind the object. This quantity is completely determined by the mutual coherence function of the scattered electron, as we have shown in chapter 4. To describe inelastic scattering and partial coherence correctly, we

have to account for all internal degrees of freedom of the object. Within the frame of the interaction representation the object state is described by a time–dependent position operator $\hat{\mathbf{R}} = \hat{\mathbf{R}}(t) = (\hat{\mathbf{R}}_1(t), \ldots, \hat{\mathbf{R}}_l(t))$. The total wave function in the interaction representation is given by

$$\Psi_I = \Psi_I(\mathbf{r}, \mathbf{R}, t) = \mathrm{e}^{\frac{i}{\hbar}\hat{\mathbf{H}}_O t}\Psi(\mathbf{r}, \mathbf{R}, t) \;, \tag{5.1}$$

where $\hat{\mathbf{H}}_O$ denotes the Hamiltonian (2.12) of the undisturbed object. The time evolution of the position operator of the object then has the form

$$\hat{\mathbf{R}}_i(t) = \mathrm{e}^{\frac{i}{\hbar}\hat{\mathbf{H}}_O t}\, \mathbf{R}_i\, \mathrm{e}^{-\frac{i}{\hbar}\hat{\mathbf{H}}_O t} \;, \qquad i = 1, \ldots, l \;. \tag{5.2}$$

By substituting the transformations (5.1) and (5.2) into the Schrödinger equation (2.1) we eventually obtain the interaction representation

$$\left\{ \frac{\hbar^2}{2m}\nabla^2 + i\hbar\,\partial_t \right\} \Psi_I = \gamma \hat{V} \Psi_I \;, \tag{5.3}$$

where

$$\hat{V} = V(\mathbf{r}, \hat{\mathbf{R}}(t)) = \sum_{i=0}^{l} V_i(\rho + z\mathbf{e}_z - \hat{\mathbf{R}}_i(t)) \tag{5.4}$$

denotes the interaction operator. The relation (5.4) is based on the assumption of a two particle interaction between the incident electron and each constituent particle $\mathbf{R}_i$, $i = 0 \ldots l$, of the object.

The interaction operator is obtained by introducing the time–dependent Heisenberg operator $\hat{\mathbf{R}} = \hat{\mathbf{R}}(t)$ for the object coordinates $\mathbf{R}$ in the interaction potential. The resulting expression is an operator–valued function of the position $\mathbf{r}$ of the scattered electron and of the time t. The object coordinates do not occur explicitely in the equation (5.3) anymore. The electron wave function interacts with the object by means of the interaction operator. To determine this interaction we must solve the differential equation (5.3) with an operator–valued right–hand side [9, 10].

Considering that the energy of the incident particle is much higher than the interaction energy and that the wave length of the incident electron is much smaller than the range of the interaction potential V, we can solve the differential equation (5.3) by the ansatz

$$\Psi_m(\mathbf{r}, \mathbf{R}, t) = \mathrm{e}^{i\mathbf{k}_i\mathbf{r} - i\omega t}\; \hat{\varphi}(\mathbf{r}, t)\phi_m(\mathbf{R}) \tag{5.5}$$

for any initial energy eigenstate ϕ_m of the object. The operator–valued function $\hat{\varphi}(\mathbf{r}, t)$ describes the interaction between the incident electron and the object. It acts only on the $\mathbf{R}$ coordinates of the object and depends on the position of the scattered electron $\mathbf{r}$ and on the time t. This function varies slowly within the range of the potential V and depends implicitly on the internal degrees of freedom of the object. With these

assumptions the differential equation (5.3) can be replaced by its high–energy approximation

$$(\frac{1}{\gamma v}\,\partial_t + \partial_z)\;\hat{\varphi}(\mathbf{r},t) = -\frac{i}{\hbar v}\;\hat{V}\;\hat{\varphi}\;, \qquad v = \frac{\hbar k_i}{\gamma m}\;. \tag{5.6}$$

Since this equation neglects all second–order partial derivatives of $\hat{\varphi}$ with respect to x, y, and z, it can only be used in the case of very thin objects. Moreover, this approximation ignores the interference between partial waves originating from different lateral points within the object. The first–order equation (5.6) can be solved analytically by integration along its characteristics. Employing the method of successive approximation, the solution is expressed by the power series

$$\begin{aligned}\hat{\varphi}(\rho,z,t) \;\; &= \;\; 1 - \frac{i}{\hbar v}\int_{-\infty}^{z}\hat{V}(z_0, t-\frac{z-z_0}{\gamma v})\;dz_0 \\ &+ \left(\frac{i}{\hbar v}\right)^2\int_{-\infty}^{z}\hat{V}(z_0,t-\frac{z-z_0}{\gamma v})\int_{-\infty}^{z_0}\hat{V}\left(z_1,t-\frac{z_0-z_1}{\gamma v}\right)\;dz_1\;dz_0 \\ &- \;\ldots\;.\end{aligned} \tag{5.7}$$

This expression is also known as the Dyson series [5] of time–dependent perturbation theory. The function $\hat{V}$ acts as an operator. Therefore, its values, taken at different positions z, do not commute. Nevertheless, by using the time–ordering brackets $[\ldots]_+$ with the time replaced by the z coordinate, we can formally sum up this power series

$$\hat{\varphi}(\mathbf{r},t) = \left[\exp\left\{-\frac{i}{\hbar v}\int_{-\infty}^{z}\sum_{i=1}^{l}V_i\left(\rho + z'\mathbf{e}_z - \hat{\mathbf{R}}_i\left(t-\frac{z-z'}{\gamma v}\right)\right)\;dz'\right\}\right]_+\;, \tag{5.8}$$

where we have already inserted the definition of the operator–valued potential (5.4).

The use of the time ordering brackets accounts for the fact that the potential of the object changes during the passage of the scattered electron. The time retardation originates from the same effect because the potential at a distinct point z_0 of the trajectory must be evaluated at the time of passage $t - \frac{z-z_0}{\gamma v}$. The time dependence can be neglected for thermal diffuse scattering because the transition time of the electron is much shorter than the time of vibration of a displaced nucleus. In this case the application of the time ordering brackets is obsolete. The time retardation can always be neglected if the extension of $\hat{V}(t,z)$ in z–direction is sufficiently small. This important fact will help us find a quite simple approximation for the mutual object transparency of a thin object slice.

The expression (5.8) yields the amplitude of the scattered electron at an arbitrary point $\mathbf{r}$ behind the object at a time t after the scattering event. The probability $|\psi_{mn}|^2$ that the object state has been changed from the initial state ϕ_m to the final state ϕ_n is determined

by the function

$$\begin{aligned}\psi_{mn}(\mathbf{r},t) &= \int \phi_n^*(\mathbf{R})\hat{\varphi}(\mathbf{r},t)\phi_m(\mathbf{R})\, d\mathbf{R} \\ &= \psi_0(\mathbf{r},t) \int \phi_n^*(\mathbf{R}) \left[\exp\left\{i\,\hat{\chi}(\rho)\right\}\right]_+ \phi_m(\mathbf{R})\, e^{i\frac{E_m-E_n}{\hbar\gamma v}(z-\gamma v t)}\, d\mathbf{R}\,,\end{aligned} \tag{5.9}$$

where the observation point $\mathbf{r}$ is located outside the range of the potential V. The function $\hat{\chi}(\rho)$ denotes the operator–valued projected potential

$$\hat{\chi}(\rho) = -\frac{1}{\hbar v}\int_{-\infty}^{\infty}\sum_{i=1}^{l} V_i(\rho + z'\,\mathbf{e}_z - \hat{\mathbf{R}}_i(\frac{z'}{\gamma v}))\, dz'\,. \tag{5.10}$$

In the time–dependent case this expression is only meaningful in the context of an exponential function enclosed by time–ordering brackets, as in equation (5.8).

The mutual product of the wave function at two distinct points ρ and ρ' of an arbitrary plane behind the object can be expressed by a superposition of all final energy eigenstates of the object as

$$\begin{aligned}&\int \Psi_m(\rho,z,t,\mathbf{R})\ \Psi_m^*(\rho',z,t',\mathbf{R})\, d\mathbf{R} = \\ &\quad\int \left(\sum_{n=0}^{\infty}\psi_{mn}\ \phi_n(\mathbf{R})\right)^* \left(\sum_{n'=0}^{\infty}\psi_{mn'}\phi_{n'}(\mathbf{R})\right)\, d\mathbf{R} \\ &\quad= \psi_0^*\psi_0 \sum_{n=0}^{\infty} e^{-i\omega_{mn}\tau} \iint \phi_n^*(\mathbf{R}) \left[\exp\left\{-i\hat{\chi}(\rho)\right\}\right]_+ \phi_m(\mathbf{R}) \\ &\qquad\times\phi_m^*(\mathbf{R}') \left[\exp\left\{i\hat{\chi}(\rho')\right\}\right]_+ \phi_n(\mathbf{R}')\, d\mathbf{R}\, d\mathbf{R}'\,.\end{aligned} \tag{5.11}$$

During the time of exposure an incident electron meets the object in the initial states ϕ_m with the probability P_m. Since the product (5.11) depends only on the difference $\tau = t - t'$ the time average in the definition of the mutual coherence function (4.2) can be replaced by an average taken over all initial states ϕ_m of the object. Accordingly, the mutual coherence function behind a very thin object adopts the stationary form

$$\begin{aligned}\Gamma(\rho,\rho',\tau) &= \psi_0^*(\rho,z,t)\psi_0(\rho',z,t') \sum_{m,n=0}^{\infty} P_m\, e^{-i\omega\tau} \\ &\quad\times \int\int \phi_n^*(\mathbf{R}) \left[\exp\left\{-i\hat{\chi}(\rho)\right\}\right]_+ \phi_m(\mathbf{R})\ \phi_m^*(\mathbf{R}') \\ &\quad\times \left[\exp\left\{i\hat{\chi}(\rho')\right\}\right]_+ \phi_n(\mathbf{R}')\, d\mathbf{R}\, d\mathbf{R}'\,.\end{aligned} \tag{5.12}$$

This relation does not depend on a specific form of the incident wave. Therefore, we can replace the incident plane wave ψ_0 by a somewhat distorted plane wave. Since we have neglected backscattering, we can consistently assume that the fluctuations of the

initial wave and of the object potential are stochastically uncorrelated when performing the time average.

The mutual object transparency of a thin object slice is defined as

$$M(\rho,\rho',\tau) = \sum_{m,n} P_m\, e^{-i\omega\tau} \int\int \phi_n^*(\mathbf{R})\,[\exp\{-i\hat{\chi}(\rho)\}]_+ \times\phi_m(\mathbf{R})\;\phi_m^*(\mathbf{R}')\,[\exp\{i\hat{\chi}(\rho')\}]_+\,\phi_n(\mathbf{R}')\;.\,d\mathbf{R}\,d\mathbf{R}'\;. \tag{5.13}$$

This function connects the mutual coherence function directly behind the thin slice $\Gamma^{(f)}$ with $\Gamma^{(i)}$ at the plane directly in front of the slice via the relation

$$\Gamma^{(f)}(\rho,\rho',\tau) = M(\rho,\rho',\tau)\;\Gamma^{(i)}(\rho,\rho',\tau)\;. \tag{5.14}$$

The sum in (5.13) can be rewritten as the time average of the product of the time–dependent operator–valued phase factors:

$$M(\rho,\rho',\tau) = \left\langle [\exp\{-i\hat{\chi}(\rho,t)\}]_+\,[\exp\{i\hat{\chi}(\rho',t')\}]_+ \right\rangle_T\;. \tag{5.15}$$

The time–dependent operator–valued projected potential $\hat{\chi}$ is defined similarly to equation (5.10) as

$$\hat{\chi}(\rho,t) = -\frac{1}{\hbar v}\int_{-\infty}^{\infty} V(\rho,z,\hat{\mathbf{R}}(t+\frac{z}{\gamma v}))\;dz \tag{5.16}$$

The propagation of the electron wave through a thin slice is governed by equation (5.15). This function depends only on the two coordinates ρ and ρ', respectively. The integration over the initial plane is obsolete in the case of a thin slice. Nevertheless, the transmission function still depends mutually on the primed and unprimed lateral coordinates. This property guarantees the validity of the generalized optical theorem.

The successive application of the formula (5.14) allows the calculation of the mutual coherence function for a thick object by iteration [10]. The mutual object transparency for a sufficiently thin slice of the object represents a generalization of the well–known transmission function used in the theory of purely elastic scattering. In this case the double sum in (5.13) reduces to a single sum since the transition matrix is diagonal. If in addition the object is in its ground state the mutual dynamic object transparency $M(\rho,\rho',\tau)$ reduces to the product $M_{el}(\rho,\rho',\tau) = T^*(\rho)\;T(\rho')\exp(i\omega\tau)$, where $T(\rho) = \exp\{i\chi(\rho)\}$ is the complex transmission function for a static potential. We obtain this special case from the definition (5.13) by choosing $P_m = \delta_{m0}$, where δ_{mn} denotes the Kronecker symbol.

5.2 Generalized multislice formalism

For thick objects the mutual object transparency is a highly complicated function of the dynamic object potential due to the multiple scattering of the electrons within the

object, as we have already discussed in chapter 4. The conventional multislice algorithm [17, 45, 20, 11] neglects inelastic scattering and the transmission of the electron wave through a thin object slice is described by the elastic transmission function. In this case the propagation of the electron wave through a thick object is solved iteratively by subdividing the object potential into a sequence of N thin slices. Each step in the iteration consists of a multiplication with the transmission function and a convolution with the free–space propagator, as illustrated in figure 5.1.

In order to incorporate inelastic scattering, we assume that (a) each object state ϕ_n is sufficiently well localized within a distinct slice of the object, (b) the ranges of the interaction potentials are not larger than the slice thickness and (c) the object is at thermal equilibrium [10]. In this case the wave function in front of each slice must be replaced by the mutual coherence function Γ, and the interaction with the object must be described by a multiplication with the mutual object transparency (5.15) for each slice.

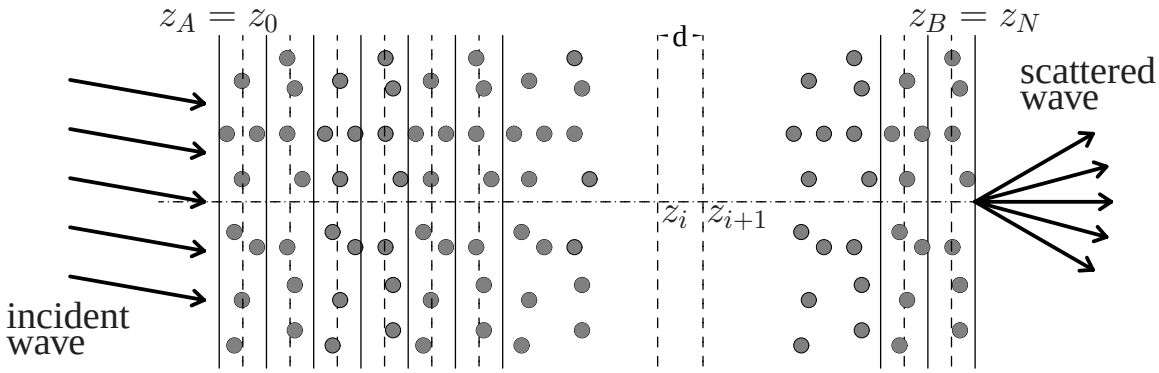

Figure 5.1: *Schematic illustration of the conventional multislice procedure. Each dot represents an atom of the object. The plane of projection is sketched for each slice by a broken line.*

The propagation of the mutual coherence function between two successive intermediate planes $z = z_i$ and $z = z_{i+1}$ is obtained by multiplying the mutual coherence function at the plane $z = z_i$ with the mutual object transparency M_i of the i-th slice and performing a four–dimensional Fresnel propagation to the plane $z_{i+1} = z_i + d$. By iteration we find the generalized multislice equation

$$\Gamma(\rho_N, \rho'_N, \tau) = \int \dots \int \Gamma(\rho_0, \rho'_0, \tau) \times \prod_{i=0}^{N-1} M_i(\rho_i, \rho'_i, \tau)\; P_F(\rho_{i+1} - \rho_i, \rho'_{i+1} - \rho'_i)\; d^2\rho_i\, d^2\rho'_i \; . \tag{5.17}$$

For the first and last step the free–space propagation must take place over one half of the thickness of the first or last slice, respectively. This behaviour is due to the fact that

the object potential is projected onto the midplane of each slice. Hence one can omit these two propagations if we define the midplane of the first slice as the entrance plane and the corresponding plane of the last slice as the exit plane.

The proposed multislice formalism for the coherence function is a five–dimensional representation of the propagation of an electron through the object. If we insert the expression (5.17) into equation (4.27) and consider the definition (5.23) of the mutual object transparency we eventually obtain the representation

$$\begin{aligned} T(\rho_0, \rho'_0, \rho_N, \rho'_N \tau) \;=\; & \int \dots \int M_0(\rho_0, \rho'_0, \tau)\; P_F(\rho_1 - \rho_0, \rho'_1 - \rho'_0) \\ & \times \prod_{i=1}^{N-1} M_i(\rho_i, \rho'_i, \tau)\; P_F(\rho_{i+1} - \rho_i, \rho'_{i+1} - \rho'_i)\; d^2\rho_i\, d^2\rho'_i \;. \end{aligned} \tag{5.18}$$

of the mutual object transparency defined in equation (4.20). This relation is valid as long as backscattering can be neglected. In equation (5.18) the ρ_0, ρ'_0 coordinates refer to the entrance plane $z = z_A$ and the ρ_N, ρ'_N coordinates refer to the exit plane $z = z_B$ of the thick object, as depicted in figure 4.3.

The iterated integral representation of the mutual object transparency in equation (5.18) is formally equivalent with a Feynman path integral representation of the propagator of the time–dependent Schrödinger equation. This correspondence becomes obvious if we consider that the high–energy approximation of the stationary Schrödinger equation has the same structure as the time–dependent Schrödinger equation apart from its lower dimension. Therefore, we can use the same mathematical formalism to solve these equations. Nevertheless, an important difference exists. The Feynman path integral approach to time–dependent quantum mechanics provides a formally exact solution of the theory, whereas the multislice method only holds true within the frame of validity of the high–energy approximation.

In the next step we have to evaluate the mutual object transparency for a thin object slice approximately. This will provide us with analytical expressions for the absorption potential and for the terms describing inelastic and elastic scattering [8, 9, 10]. Using the fact that the projected potential can be considered as a small quantity if the object slices are sufficiently thin, we can approximate the mutual object transparency (5.15) by an expression which closely resembles the transmission function with an absorption potential $T_{abs}(\rho) = \exp(i(\chi(\rho) + i\frac{1}{2}\mu_2(\rho)))$[11, 40]. The complex exponent is known as the optical potential in conventional image simulation. The term μ_2 accounts for an unrealistic absorption of the inelastically scattered electrons within the object. Obviously, this approximation violates the optical theorem of scattering theory. To avoid this discrepancy we must employ the mutual object transparency. To obtain a more realistic approximation we expand the logarithm of $M(\rho, \rho', \tau)$ in a power series. Using

the expression (5.23) and considering only terms up to second order in $\hat{\chi}$, we obtain [8]

$$\begin{aligned}
\ln M(\rho,\rho',\tau) \approx \ln \Bigg\langle & 1 + i\hat{\chi}(\rho,t) - i\hat{\chi}(\rho',t') + \hat{\chi}(\rho,t)\hat{\chi}(\rho',t') \\
& - \left(\frac{1}{\hbar v}\right)^2 \int_{-\infty}^{\infty} \hat{V}(\rho,z,t) \int_{-\infty}^{z} \hat{V}(\rho,z',t)\, dz'\, dz \\
& - \left(\frac{1}{\hbar v}\right)^2 \int_{-\infty}^{\infty} \hat{V}(\rho',z,t') \int_{-\infty}^{z} \hat{V}(\rho',z',t')\, dz'\, dz \Bigg\rangle \\
\approx\ & i\left(\langle\hat{\chi}(\rho,t)\rangle - \langle\hat{\chi}(\rho',t')\rangle\right) + \langle\hat{\chi}(\rho,t)\hat{\chi}(\rho',t')\rangle \\
& + \frac{1}{2}\left(\langle\hat{\chi}(\rho,t)\rangle - \langle\hat{\chi}(\rho',t')\rangle\right)^2 \\
& - \left(\frac{1}{\hbar v}\right)^2 \left\langle \int_{-\infty}^{\infty} \hat{V}(\rho,z,t) \int_{-\infty}^{z} \hat{V}(\rho,z',t)\, dz'\, dz \right\rangle \\
& - \left(\frac{1}{\hbar v}\right)^2 \left\langle \int_{-\infty}^{\infty} \hat{V}(\rho',z,t') \int_{-\infty}^{z} \hat{V}(\rho',z',t')\, dz'\, dz \right\rangle \\
=\ & i\left(\mu_1(\rho) - \mu_1(\rho')\right) - \frac{1}{2}\left(\mu_2(\rho) + \mu_2(\rho')\right) + \mu_{11}(\rho,\rho',\tau)\ . \qquad (5.19)
\end{aligned}$$

Here we have used the definitions

$$\begin{aligned}
\mu_1(\rho) &= \langle\hat{\chi}(\rho,t)\rangle\ , & (5.20)\\
\mu_2(\rho) &= \frac{2}{(\hbar v)^2}\left\langle \int_{-\infty}^{\infty} \hat{V}(\rho,z,t) \int_{-\infty}^{z} \hat{V}(\rho,z',t)\, dz'\, dz \right\rangle - \langle\hat{\chi}(\rho,t)\rangle^2 \\
&\approx \langle\hat{\chi}^2(\rho,t)\rangle - \langle\chi\rangle^2(\rho) \;=\; \langle\left(\hat{\chi}(\rho,t) - \mu_1(\rho)\right)^2\rangle\ , & (5.21)\\
\mu_{11}(\rho,\rho',\tau) &= \langle\hat{\chi}(\rho,t)\hat{\chi}(\rho',t')\rangle - \mu_1(\rho)\mu_1(\rho')\ . & (5.22)
\end{aligned}$$

The second relation in equation (5.21) is obtained by considering that the slices are very thin. In this case the double integral approximately represents $\frac{(\hbar v)^2}{2}\langle\chi^2\rangle$. With this result we find the approximation of the mutual object transparency of a thin slice

$$M(\rho,\rho',\tau) \approx \exp\left(- i\left(\mu_1(\rho) - \mu_1(\rho')\right) - \frac{1}{2}\left(\mu_2(\rho) + \mu_2(\rho')\right) + \mu_{11}(\rho,\rho',\tau)\right)\ . \qquad (5.23)$$

The same result can be obtained by a more intuitive procedure if we make a quasi–static approximation for the dynamic object potential. In this approximation the time–ordering brackets in the expression (5.8) are obsolete and the mutual object transparency of a thin slice reduces to

$$M(\rho,\rho',\tau) \approx \langle\exp\left(-i\chi(\rho,t) + i\chi(\rho',t-\tau)\right)\rangle_T\ . \qquad (5.24)$$

This average can be evaluated by the method of the stochastical cumulants [46].

Given a probability variable $\hat{A}$ obeying a probability distribution F the expected value of the exponential function of $\hat{A}$ adopts the form

$$\langle \exp(\hat{A}) \rangle = \exp(\sum_{n=1}^{\infty} \frac{1}{n!} K_n(\hat{A})) \; , \tag{5.25}$$

where $K_n(\hat{A})$, $n = 1, 2, \ldots$ denote the nth–order cumulants of $\hat{A}$ with respect to the distribution F. The first three cumulants are given by

$$K_1(\hat{A}) = \langle \hat{A} \rangle \; , \tag{5.26}$$

$$K_2(\hat{A}) = \langle \Big(\hat{A} - \langle \hat{A} \rangle \Big)^2 \rangle \; , \tag{5.27}$$

$$K_3(\hat{A}) = \langle \Big(\hat{A} - \langle \hat{A} \rangle \Big)^3 \rangle \; . \tag{5.28}$$

This terms correspond to the expected value, the variance, and the skewness of the probability distribution F, respectively [46].

In our case we can apply the relation (5.25) to calculate the average in equation (5.24) and restrict the expansion of the exponent to the first–order and the second–order terms. This yields equation (5.23).

With these results a presentive interpretation of the relation (5.23) is possible, which illustrates the relation between the conventional multislice and the coherence function approach. Elastic scattering is described by the first two terms of the exponent. Each of these terms represents a phase shift of the electron wave which is proportional to the time–averaged dynamical projected potential of the slice. The terms $\mu_2(\rho)$ and $\mu_2(\rho')$ represent a kind of absorption potential that effectively removes the inelastically scattered electron from the elastic scattering channel. The term $\mu_{11}(\rho, \rho', \tau)$ describes the contribution of the inelastically scattered electrons to the image intensity, hence it accounts for the propagation of the electrons scattered into the inelastic channels. This term is a direct consequence of the optical theorem which ensures the conservation of the number of particles:

$$\begin{aligned} M(\rho, \rho' = \rho, \tau = 0) &= 1 \; , \\ \mu_2(\rho) &= \mu_{11}(\rho, \rho' = \rho, \tau = 0) \; . \end{aligned} \tag{5.29}$$

This equation is fulfilled by our approximation since for $\rho = \rho'$ the covariance reduces to the variance of the dynamic potential owing to the definitions (5.20). We can restate the relation (5.29) in the reciprocal space. If we follow this line we obtain after a short calculation

$$\mu_2(\mathbf{q}, \omega) = \frac{1}{2\pi} \int \int \mu_{11}(\mathbf{q} + \mathbf{q}', \mathbf{q}', \omega) \; d^2\mathbf{q}' \, d\omega \; . \tag{5.30}$$

This expression is very useful to calculate the absorption potential for an interaction process described by $\mu_{11} = \mu_{11}(\mathbf{q}, \mathbf{q}', \omega)$. Conversely, for a pair of functions $\mu_2(\mathbf{q})$ and $\mu_{11}(\mathbf{q}, \mathbf{q}', \omega)$ which fulfills the relation (5.30), the validity of the optical theorem (5.29) is guaranteed. This result is of great importance for our theory.

The mutual object transparency (5.23) factorizes if $\mu_{11} = 0$. Each of the two factors then represents the transmission function with an absorption potential $T_{\text{abs}} = T_{\text{abs}}(\rho)$ for the standard multislice algorithm. The coherence function approach, therefore, is a true generalization of the conventional multislice theory.

For purely elastic scattering the transmission function for each slice of the object only depends on the static projected object potential of the particular slice. A different situation arises if inelastic scattering is considered. In this case the object potential cannot assumed as static owing to the excitation of its internal degrees of freedom. The information contained in the time averaged generalized dynamic object potential (5.20) does not suffice to calculate the spatial distribution of the inelastically scattered electrons in the image plane. To account for the complete inelastic intensity distribution we have introduced the time–dependent projected object potential through the interaction representation. This function provides the required dynamical information. Inelastic scattering contributes to the quadratic part of the mutual dynamic object spectrum for thin specimens, as shown in section 4.5. In this case we can describe the influence of inelastic scattering by the variance $\mu_2 = \mu_2(\rho)$ and the covariance $\mu_{11}(\rho, \rho', \tau)$ of the dynamic object potential. This result allows a stochastical interpretation of the terms occurring in equation (5.23). We may consider the dynamic object potential as a stochastic process in time. The effect of the inelastic scattering processes appears as the results of fast microscopic fluctuations of the object state. The intensity of the contribution of inelastic scattering to the mutual coherence function for a very thin slice is, therefore, proportional to the covariance of the fluctuations of the dynamic object potential. We can verify this conclusion if we expand the exponential function in equation (5.23) into a Taylor series and consider the fact that μ_1^2 and μ_2 have the same order of magnitude as μ_{11}.

The formulae (5.17) and (5.23) reduce the problem of image formation to the calculation of the first and second stochastical momenta of the time–dependent scattering potential of each slice of the object. With this information about a given object, we can employ the coherence function multislice procedure (5.17) to determine the mutual coherence function at the exit plane behind the object, if this function is known at the entrance plane in front of the object [10].

Unfortunately, the numerical evaluation of the five–dimensional coherence function multislice equation is not possible without further approximations using present days computers. Fortunately, we can show that the numerical expenditure for the calculation of the coherence function can be reduced drastically by decomposing the mutual coherence function into a sum of symmetric products.

The generalized multislice formula (5.17) describes the propagation of the mutual co-

herence function $\Gamma(\rho, \rho', \tau; z)$ through the object. It correctly accounts for elastic and inelastic plural scattering processes within the object. In most situations of practical importance it suffices to consider plural elastic scattering in combination with single inelastic scattering. This approximation holds true even for moderately thick specimens because partial waves originating from different inelastic scattering events are incoherent with each other and do not interfere. Hence only elastic multiple scattering generates coherent dynamical scattering effects. Neglecting inelastic multiple scattering, the image intensity resulting from single inelastic scattering

$$I_{\text{in}}^{(1)}(\rho) = \sum_{j=1}^{N} I_j(\rho) \tag{5.31}$$

is composed of the partial intensities I_j, contributed by the individual slices $j = 1, \ldots, N$. If the object thickness is comparable to the inelastic mean free path length, we must consider the contributions of multiple inelastic scattering to the sum on the right–hand side of equation (5.31). The second–order term

$$I_{\text{in}}^{(2)}(\rho) = \sum_{j=1}^{N} \sum_{i=1}^{j-1} I_{ij}(\rho) \tag{5.32}$$

accounts for inelastic double scattering. In this expression the term I_{ij} denotes the part of the image intensity, which is produced by inelastic scattering in the ith slice and subsequent inelastic scattering in slice $j > i$. Unfortunately, the numerical evaluation of the higher–order terms requires a large amount of expenditure. Since the partial waves resulting from different inelastic scattering processes cannot interfere with each other, we can express the higher–order contributions approximately by means of the single scattering intensities. This simple approximation describes the inelastic scattering cross section correctly even in the case of thick objects. Because the generalized multislice formalism fulfills the optical theorem, no intensity is lost during the propagation of the mutual coherence function through the entire object. Within the frame of validity of the single inelastic scattering approximation the sum of the total inelastically scattered intensity $\bar{I}_{\text{in}}$ and the elastically scattered intensity $\bar{I}_{\text{el}}$ is equal to the initial intensity $\bar{I}_0 = \bar{I}_{\text{el}} + \bar{I}_{\text{in}}$. The absorption term μ_2 in the exponent of the mutual dynamic object transparency for a single slice in the generalized multislice formalism effectuates a non realistic loss of intensity if we apply the single inelastic scattering approximation to objects with a thickness exceeding one half of the inelastic mean free path length. If we do not need to differentiate between single and multiple inelastic scattering we can use the relation

$$I \approx I_{\text{el}} + \frac{\bar{I}_0 - \bar{I}_{\text{el}}}{\bar{I}_{\text{in}}^{(1)}} \, I_{\text{in}}^{(1)} \tag{5.33}$$

to correct for this effect. For most specimens in high–resolution imaging this correction is not required since these objects are sufficiently thin.

5.3 Mutual object transparency

The mutual coherence function depends on the spatial coordinates ρ, ρ' and the time increment τ. This parameter distinguishes between the different energy losses within the object. Due to the chromatic aberration of the objective lens, partial waves belonging to different energy losses are transferred differently by the microscope. Therefore, it is advantageous to discuss the generalized multislice formalism in terms of the spectral density of the mutual coherence function

$$\Gamma(\rho, \rho', \omega; z) = \frac{1}{2\pi} \int \Gamma(\rho, \rho', \tau; z) \exp(i\omega\tau)\ d\tau\ . \tag{5.34}$$

If we assume a discrete set of possible excitations of the object with excitation energies ω_j, $j = 0, 1, \ldots$, the Fourier transform of the mutual dynamic object transparency with respect to τ is given by

$$\int M(\rho, \rho', \tau)\ \mathrm{e}^{i\omega\tau}\ d\tau = 2\pi\ \sum_j M(\rho, \rho', \omega_j)\ \delta(\omega + \omega_j)\ . \tag{5.35}$$

In this case the transmission of the mutual coherence function through a single slice adopts the form

$$\Gamma_f(\rho, \rho', \omega) = \sum_j M(\rho, \rho', \omega_j)\ \Gamma_i(\rho, \rho', \omega + \omega_j)\ . \tag{5.36}$$

This result has been obtained by inserting the approximation (5.35) into the Fourier transform of equation (5.14). Equation (5.36) shows that the image intensities belonging to different energy losses can be calculated separately and added up subsequently. Nevertheless, partial waves belonging to different energy losses must be propagated separately through the optical system up to the recording plane where the incoherent superposition is performed [26, 10]. This necessity results from the chromatic aberration which causes an energy–dependent transfer of the spatial frequencies. Considering the relation (5.36) and assuming single inelastic scattering, we derive the following expression for the mutual spectral density at the exit plane $z = z_B$ from the Fourier transform of formula (5.17):

$$\begin{aligned}\Gamma(\rho, \rho', \omega; z_B) \ &= \ \sum_j \sum_{k=0}^{N-1} \int \ldots \int \Gamma(\rho_0, {\rho'}_0, \omega + \omega_j; z_A) \\ &\times \prod_{i=0}^{N-1} M_i(\rho_i, {\rho'}_i, \omega = \delta_{ik}\omega_j)\ P_F(\rho_{i+1} - \rho_i, {\rho'}_{i+1} - {\rho'}_i)\ d^2\rho_i\, d^2{\rho'}_i\ .\end{aligned} \tag{5.37}$$

In this representation we have assumed that the spectral density of the mutual coherence function at the entrance plane $z = z_A$ of the object is known. If we neglect

the chromatic aberration of the illumination system, the mutual coherence function in front of the object factorizes with respect to the spatial coordinates and the energy

$$\Gamma(\rho, \rho', \omega; z_A) = \Gamma(\rho, \rho'; z_A)\; p(\omega)\;. \tag{5.38}$$

The energy distribution $p(\omega)$ is determined by the electron source. In the case of a point–like effective source the spatial term $\Gamma(\rho, \rho'; z_A)$ also factorizes such that one factor solely depends on the primed and the other solely on the unprimed coordinates. This situation is approximately realized for coherent illumination. In the general case of partially coherent illumination the initial mutual coherence does not factorize with respect to any of the variables. We find this situation for the scanning transmission microscopy where the chromatic and geometric aberrations of the probe forming lens and the finite size and energy width of the electron source cannot be neglected.

The sum over the index j in the equation (5.37) comprises all possible energy losses. For purely elastic scattering the mutual dynamic object transparency M_i of slice i reduces to $M_i(\rho, \rho', \omega = 0) = T^*(\rho)\; T(\rho')$. To include inelastic scattering we first consider a single excitation with energy loss $\hbar\omega \approx \hbar\omega_{\text{ex}}$. This assumption does not restrict the general validity of our approach.

In order to efficiently compute the convolution of the four–dimensional free–space propagator with the mutual dynamic object transparency in equation (5.37) we utilize the Fourier convolution theorem. For this purpose we introduce the Fourier transform of the four–dimensional Fresnel propagator

$$\begin{aligned} \mathcal{F}\mathcal{F}'\;[P_F(\rho, \rho')] &= \int\!\!\int P_F(\rho)\; P_F^*(\rho')\; \mathrm{e}^{i\rho\mathbf{q}}\; \mathrm{e}^{-i\rho'\mathbf{q}'}\; d^2\rho\, d^2\rho' \\ &= P_F(\mathbf{q})\; P_F^*(\mathbf{q}')\;. \end{aligned} \tag{5.39}$$

Here $\mathcal{F}$ and $\mathcal{F}'$ denote the two–dimensional Fourier transformation with respect to the primed and the unprimed coordinates, respectively. To account for the hermitian structure of the coherence function formalism, the primed Fourier transform is defined as the complex–conjugated of the unprimed transform.

In the case of elastic scattering and coherent illumination the mutual intensity $\Gamma(\rho, \rho', z_0) = \psi^*(\rho, z_0)\psi(\rho', z_0)$ factorizes into a bilinear, hermitian product of the stationary wave function ψ evaluated at the lateral positions ρ and ρ', respectively. In the general case the mutual intensity in front of the object can formally be expanded into a series of products

$$\Gamma(\rho, \rho'; z_A) = \sum_l \Phi_l^*(\rho; z_A)\Phi_l(\rho'; z_A)\;, \tag{5.40}$$

where each factor solely depends on the primed or unprimed coordinates. The expansion functions Φ_l do not need to have a distinct physical meaning. Only in the special case of an incident axial plane wave $\psi_0(z, t)$, the sum in (5.40) reduces to a single term

$l = 0$ with $\Phi_0(\rho; z_0) = \psi_0(z_0, t = 0)$. For partially coherent Köhler illumination it is convenient to decompose the initial mutual coherence function (5.40) in a product of two sums. One weighted sum is over a discrete set of energies representing the energy spread of the source. The other sum over the different directions of the incident plane waves accounts for the incoherently radiating points of the effective source. In the case of Köhler illumination each point of the effective source corresponds to a distinctly tilted plane wave in the entrance plane of the object.

Without loss of generality we restrict our further investigations by considering only a single term of the sum (5.40). In this case the mutual spectral density at the plane $z = z_A = z_0$ in front of the object has the form $\Gamma(\rho, \rho', \omega; z_A) = \Phi^*(\rho, \omega; z_A)\Phi(\rho', \omega; z_A)$ and, therefore, the mutual spectral density at the exit plane $z_B = z_N = z_0 + N\,d$ is given by

$$\begin{aligned}\Gamma(\rho_N, {\rho'}_N, \omega; z_B) \;=\; & \\ & \sum_{j=0}^{N-1} \int \dots \int \Phi^*(\rho_0, \omega + \omega_{ex}; z_A)\, \Phi({\rho'}_0, \omega + \omega_{ex}; z_A) \\ & \times \prod_{i=0}^{N-1} P_F(\rho_{i+1} - \rho_i, {\rho'}_{i+1} - {\rho'}_i; d)\; M_i(\rho_i, {\rho'}_i, \omega = \delta_{ji}\omega_{ex})\; d^2\rho_i\, d^2{\rho'}_i\;.\end{aligned} \tag{5.41}$$

Although we start from the entrance plane with a product function, the coherence function at the exit plane does not factorize. This behaviour is because the transparency $M_j(\rho, \rho', \omega)$, which describes the inelastic interaction in the jth slice, depends mutually on the primed and unprimed position vectors.

Since the mutual dynamic object transparency of the $j$the slice is a hermitian function $M_j(\rho, \rho', \omega) = M_j^*(\rho', \rho, \omega)$, it can be decomposed in a series of hermitian products

$$M_j(\rho, \rho', \omega_{ex}) = \sum_{m=0}^{\infty} T_j^{(m)\,*}(\rho, \omega)\; T_j^{(m)}(\rho', \omega)\;, \tag{5.42}$$

as it is the case for the mutual coherence function. The individual modified transmission functions $T_j^{(m)}$, $m = 0, 1, \dots$ have a physical meaning only if we neglect the mixed term $\mu_{11}(\rho, \rho', \tau)$ in the definition of the mutual dynamic object transparency (5.23). In this case the sum in (5.42) reduces to the first term $m = 0$. The remaining factor $T_i^{(0)}$ represents the conventional elastic transmission function with an absorption potential

$$T_{\text{abs}}(\rho) = \exp\left(i\mu_1(\rho) - \frac{1}{2}\mu_2(\rho)\right)\;. \tag{5.43}$$

Later on we will present a fast converging decomposition (5.42) and hence for practical computations we only need to consider the first few term of this sum.

If we insert the expansion (5.42) into the generalized multislice formula (5.41), use the factorization of the incident mutual intensity, and exchange the order of summation and integration, we find that the propagation of each term in the expansion of the final mutual intensity can be computed by means of a conventional two–dimensional multislice formalism. Since the four–dimensional Fresnel propagator $P_F(\rho,\rho') = P_F^*(\rho)\ P_F(\rho')$ decomposes into a product of two two–dimensional Fresnel propagators, the propagation of the function $\Phi(\rho;z)$ through the object is governed by the modified transmission functions $T_i^{(m)}$. At the plane $z = z_B = z_N$ behind the last slice we find

$$\begin{aligned}\Phi^{(m,j)}(\rho_N;z_N) &= \int\ldots\int \Phi(\rho_0;z_0)\prod_{i=0}^{N-1} P_F(\rho_{i+1}-\rho_i) \\ &\quad\times T_i^{(m)}(\rho_i,\omega=\delta_{ji}\omega_{ex})\ d^2\rho_i\ .\end{aligned} \tag{5.44}$$

This formulation closely resembles that of the conventional multislice formula. By substituting the stationary wave function for $\Phi^{(m)}$ and the conventional transmission function for $T_i^{(m)}$ we obtain the well–know multislice formula of elastic scattering. In the case of a single energy loss ω_{ex} the mutual intensity at the plane $z = z_B = z_N$ is given by

$$\Gamma(\rho,\rho';z_N) = \sum_{j=0}^{N-1}\sum_{m=0}^{\infty} \Phi^{(m,j)\,*}(\rho;z_N)\Phi^{(m,j)}(\rho';z_N)\ . \tag{5.45}$$

With this result it is possible to reduce the spatially four–dimensional generalized multislice formalism to an iterative two–dimensional procedure. This crucial reduction enables the numerical evaluation of the generalized multislice formula for a realistic object with present–days computers. In both cases the energy parameter $\hbar\omega$ can be considered as a further longitudinal dimension. This parameter accounts for the different mutually incoherent energy channels.

To find a sufficiently fast converging representation of the type (5.42) in terms of partial transmission functions, we start from the full mutual dynamic object transparency of a single slice

$$\begin{aligned}M(\rho,\rho',\tau) &= \exp\left[\sum_{j=1}^{M}\left\{i(\mu_1^{(j)}(\rho-\rho_j)-\mu_1^{(j)}(\rho'-{\rho'}_j))\right.\right. \\ &\quad\left.\left.-\frac{1}{2}\{\mu_2^{(j)}(\rho-\rho_j)+\mu_2^{(j)}(\rho'-\rho_j)\}+\mu_{11}^{(j)}(\rho-\rho_j,\rho'-\rho_j,\tau)\right\}\right]\ .\end{aligned} \tag{5.46}$$

The atoms are situated at the lateral positions ρ_j, $j = 1,\ldots,M$. This formula follows from equation (5.23) with the assumption that the temporal fluctuations of the projected potentials of different atoms are stochastically uncorrelated $\langle\chi_i\ \chi'_j\rangle = \langle\chi_i\rangle\ \langle\chi'_j\rangle$ for $i \neq j$. The functions $\mu_2^{(j)}$ and $\mu_{11}^{(j)}$ depend on the atomic number of the atom located

at position ρ_j. This assumption simplifies the single slice transparency function considerably. In principle the formalism can be extended in order to account for the most dominant nearest neighbour correlations. However, the evaluation requires a concise model of these correlations.

The terms $\mu_2^{(j)}$ and $\mu_{11}^{(j)}$ in the exponent of expression (5.46) are small compared to unity. For obtaining the decomposition (5.42), we expand the exponential function with respect to this quantity μ_{11}. Retaining only the first–order terms, we derive

$$\begin{aligned} M(\rho,\rho',\tau) &= \exp\left[\sum_j i\{\mu_1^{(j)}(\rho-\rho_j)-\mu_1^{(j)}(\rho'-{\rho'}_j)\}\right. \\ &\quad \left.-\frac{1}{2}\{\mu_2^{(j)}(\rho-\rho_j)+\mu_2^{(j)}(\rho'-\rho_j)\}\right] \\ &\quad + \sum_j \mu_{11}^{(j)}(\rho-\rho_j,\rho'-\rho_j,\tau)\ \exp\left[\sum_j i\{\langle\chi_j\rangle-\langle\chi_j'\rangle\}\right] \qquad (5.47) \\ &= T_{\text{abs}}^*(\rho)\,T_{\text{abs}}(\rho') + \\ &\quad \sum_j \mu_{11}^{(j)}(\rho-\rho_j,\rho'-\rho_j,\tau)\,T_{\text{abs}}^*(\rho)\,T_{\text{abs}}(\rho')\ . \end{aligned}$$

To simplify the last expression we have used the definition of the conventional transmission function (5.43). This choice of the transmission function is somewhat arbitrary because we have performed the expansion of the exponential only with respect to μ_{11} but not with respect to μ_2. Since both quantities have the same order of magnitude, the expansion is not consistent with respect to the order of the expansion parameters. However, the approximation (5.47) simplifies the decomposition of the mutual transparency, as we will show later. The approximation (5.47) violates the optical theorem with an error of fourth–order in the projected potential. This fourth–order error vanishes for the improved approximation

$$\begin{aligned} M(\rho,\rho',\tau) &= \exp\left(i(\mu_1(\rho)-\mu_1(\rho'))\right)\left[\exp\left(-\frac{1}{2}(\mu_2(\rho)+\mu_2(\rho'))\right)\right. \qquad (5.48) \\ &\quad \left.+\mu_{11}(\rho,\rho')\exp\left(-\frac{1}{4}(\mu_2(\rho)+\mu_2(\rho'))\right)\right]\ . \end{aligned}$$

The first term in each of the decompositions (5.47) and (5.48) represents a product of two transmission functions with an absorption potential, each factor solely depends on the primed or unprimed coordinates, respectively. The second term on the right–hand side of (5.47) does not decompose in this simple manner because $\mu_{11}(\rho,\rho',\tau)$ depends mutually on the primed and unprimed coordinates.

Employing the Fourier convolution theorem, we can conveniently calculate the spa-

tially shifted functions for each atom

$$\mu_{11}^{(j)}(\rho-\rho_j,\rho'-\rho_j,\tau) \;=\; \mathcal{F}^{-1}\mathcal{F}'^{-1}\left[\tilde{\mu}_{11}^{(j)}(\mathbf{q},\mathbf{q}',\tau)\;\mathcal{F}\mathcal{F}'\left[\delta(\rho-\rho_j)\;\delta(\rho'-\rho_j)\right]\right]\;, \tag{5.49}$$

where $\mu_{11}^{(j)}(\mathbf{q},\mathbf{q}',\tau)$ denotes the Fourier transform of $\mu_{11}^{(j)}(\rho,\rho',\tau)$ with respect to ρ and ρ'. Therefore, it suffices to find a decomposition of $\mu_{11}^{(j)}$ in Fourier space.

For the practical computation of diffraction patterns of crystals with small unit cells the relation (5.49) must be applied with care. To evaluate the multislice equations numerically the wave functions must sampled on an uniformly spaced grid in real space. Then it is possible to calculate the Fourier transform numerically via the Fast Fourier Transformation (FFT) method [47, 48, 49]. Since in most cases the sampling in real space is not commensurable with the interatomic spacing between the atoms of the crystal lattice the resulting slight misalignment of the atomic positions produces severe artifacts in the simulated diffraction patterns. For these cases it is, therefore, mandatory to evaluate the phase shifts in Fourier space explicitely via the complex exponential function. The point symmetry of the phase shift matrix can be exploited to reduce the numerical expenditure of this procedure.

The Fourier transformation of the mutual transparency function $M = M(\mathbf{q},\mathbf{q}',\omega)$ of a thin slice of the object is completely determined by the first and second stochastical moments of the projected object potential. Additionally the adsorbtion potential μ_2 is related to the covariance of the projected dynamic object potential via the relation (5.30). Following the equations (5.46) and (5.46) a decomposition of $M = M(\rho,\rho',\omega)$ is readily available if a decomposition of $\mu_{11} = \mu_{11}(\rho,\rho',\omega)$ is known.

In principle we can employ a decomposition of μ_{11} analogously to (5.42) to obtain the absorption potential for any arbitrary object potential. We assume a decomposition in Fourier space of the form

$$\mu_{11}(\mathbf{q},\mathbf{q}',\omega_{ex}) = \sum_{j=1}^{\infty} T^{(j)\,*}(\mathbf{q})T^{(j)}(\mathbf{q}')\;, \tag{5.50}$$

In our case the energy loss is $\omega_{ex} = 0$ for thermal diffuse scattering or $\omega_{ex} = \bar{\omega}$ for electronic excitations. For practical applications only the first terms of this decomposition can be considered. Hence the series must converge sufficiently fast. Performing the Fourier transformation of the partial transmission functions $T^{(j)}(\mathbf{q})$ results in a representation of the absorption term μ_2

$$\mu_2(\mathbf{q}) = \mathcal{F}\left[\sum_{j=1}^{\infty} T^{(j)\,*}(\rho)T^{(j)}(\rho)\right]\;. \tag{5.51}$$

In general the Fourier transformation necessary to obtain the absorption term must be performed numerically employing the discrete Fourier transformation (DFT).

Fortunately, it is possible to obtain analytical expressions for the absorption potential μ_2 if we use simple interaction models to describe the inelastic scattering contributions. For more complicated interaction models we cannot expect to find analytical expressions for μ_2. In the following we shall derive representations for the special cases of thermal diffuse scattering and inelastic scattering due to electronic excitations, respectively. We employ the Einstein model for thermal diffuse scattering [30] and the Raman–Compton approximation [42, 36, 26] for inelastic scattering. These simple models are well suited to demonstrate the feasibility of the generalized multislice method because the numerical computations do not require an unduly large amount of expenditure. This is a direct consequence of the fact that the integration in equation (5.30) can be performed analytically for both cases [40, 9].

Thermal diffuse scattering is described with a sufficient degree of accuracy by the Einstein model because the resulting image is only affected by the time average of the lattice dynamics over the time of exposure. For our purpose it suffices to consider the individual atoms of the object as independent two–dimensional harmonic oscillators. The mean square elongation $u_j^2/2$ depends on the atomic number of the j–th atom. The time average of the oscillating projected object potential has the form

$$\begin{aligned} \langle\chi\rangle(\rho) &= \frac{2\pi}{k}\,\mathcal{F}^{-1}\left[f_{el}(\mathbf{q})\,\exp\left(-\frac{u^2}{4}\mathbf{q}^2\right)\right]\,, \qquad (5.52)\\ \langle\chi\chi'\rangle(\rho,\rho') &= \left(\frac{2\pi}{k}\right)^2\mathcal{F}^{-1}\mathcal{F}'^{-1}\left[f_{el}(\mathbf{q})\,\exp\left(-\frac{u^2}{4}(\mathbf{q}-\mathbf{q}')^2\right)\,f_{el}(\mathbf{q}')\right]\,. \end{aligned}$$

Here $f_{el}(\mathbf{q})$ denotes the elastic scattering amplitude of a single atom in first–order Born approximation. To retain the analytical character of the equations (5.52) it is advantageous to use the Kohl–Weickenmeier approximation (3.41) for the elastic scattering amplitudes.

The three–dimensional Fourier transform of the object potential is proportional to the first–order Born approximation of the elastic scattering amplitude. The Fourier projection theorem connects the two–dimensional Fourier transform of the projected object potential with the scattering amplitude:

$$\chi(\mathbf{q}) = \int \exp(-i\mathbf{q}\rho)\int \phi(\rho,z)\,dz\,d^2\rho = f^B(\mathbf{q})\,. \qquad (5.53)$$

Hence we must not consider the relations (5.52) as first–order Born approximations.

The mixed exponential term in the second expression of (5.52) can be written as a sum of products by means of the generating function of the modified Bessel function

I_n [50]:

$$\begin{aligned} e^{2(\frac{u}{2})^2\mathbf{q}\mathbf{q}'} &= \sum_{|n|} I_n(2(\frac{u}{2})^2 qq')e^{in(\phi-\phi')} \\ &= \sum_{|n|,k} \frac{((\frac{u}{2})^2 qq')^{n+2k}}{k!(k+|n|)!} e^{in(\phi-\phi')} \ . \end{aligned} \tag{5.54}$$

Inserting this expansion into equation (5.52) yields the decomposition

$$\begin{aligned} \langle \chi\chi^{'} \rangle(\mathbf{q},\mathbf{q}') &= \left(\frac{2\pi}{k}\right)^2 \\ &\times \sum_{|n|,k} \{f_{el}(\mathbf{q}) \frac{\exp\{-(\frac{u}{2})^2 q^2\}(\frac{uq}{2})^{|n|+2k}}{\sqrt{k!(k+|n|)!}} e^{in\phi}\} \times \{q',\phi'\}^* \ , \end{aligned} \tag{5.55}$$

where $\{q',\phi'\}^*$ denotes the complex–conjugate of the first factor with the unprimed coordinates replaced by the primed ones. In most cases only a few terms of the sum in equation (5.55) must be taken into account because the product expansion converges sufficiently fast [10].

Inelastic scattering results in electronic excitations of the atoms. To describe this effect, we use the modified Raman-Compton approximation for the inelastic part $S_j^{(in)}(\mathbf{K},\mathbf{K}',\omega)$ of the mixed dynamic form factor $S_j(\mathbf{K},\mathbf{K}',\omega)$ of the j–th atom with atomic number Z_j. We have already discussed this approximation in the sections 3.2 and 4.5. Assuming an average excitation energy $\bar{\omega}$, we obtain

$$S_j^{(in)}(\mathbf{K},\mathbf{K}',\omega) = \delta(\omega-\bar{\omega}) \left\{ F_j(\mathbf{K}-\mathbf{K}') - \frac{F_j(\mathbf{K})F_j(\mathbf{K}')}{Z_j} \right\} \ , \tag{5.56}$$

where $\mathbf{K}$, $\mathbf{K}'$ denote the three–dimensional scattering vectors.

The X-ray scattering amplitude F_j in equation (5.56) depends on the electronic charge distribution of the j–th atom as we have already discussed in chapter 4. The numerical values of the X–ray scattering amplitude $F = F(\mathbf{q})$ are tabulated in the literature. As we have discussed in chapter 3 the Doyle–Turner Gaussian fit provides the most convenient parameterization for our application to image simulation.

The factorization of the analytical expression for $\mu_{11}^{(in,j)}$ follows from the representation

$$\begin{aligned} \mu_{11}^{(in,j)}(\rho,\rho',\tau) &= \left(\frac{4\pi\alpha}{\beta}\right)^2 \\ &\mathcal{F}^{-1}\mathcal{F}'^{-1} \left[\int \frac{S_j^{(in)}(\mathbf{q},\mathbf{q}',\omega)}{(\mathbf{q}^2+k^2\Theta_E^2)(\mathbf{q}'^2+k^2\Theta_E^2)} \ e^{-i\omega\tau} d\omega \right] \ , \end{aligned} \tag{5.57}$$

where $\alpha \simeq 1/137$ is the fine structure constant and $\beta = v/c$ denotes the normalized velocity of the incident electron. Inserting the approximation (5.56) into the equation (5.57), we eventually obtain

$$\begin{aligned} \tilde{\mu}_{11}^{(j)}(\mathbf{q},\mathbf{q}',\tau) &= \left(\frac{4\pi\,\alpha}{\beta}\right)^2 \\ &\quad \times \frac{1}{\mathbf{K}^2\mathbf{K}'^2}\,\left\{F_j(\mathbf{q}-\mathbf{q}') - \frac{1}{Z_j}\,F_j(\mathbf{q})F_j(\mathbf{q}')\right\}\,e^{-i\omega_{\rm ex}\tau}\,. \end{aligned} \tag{5.58}$$

To factorize this expression, we only need to decompose the first term in the parenthesis on the right–hand side. Employing the formula (5.54), we find

$$\begin{aligned} \frac{F(\mathbf{q}-\mathbf{q}')}{\mathbf{K}^2\mathbf{K}'^2} &= \frac{F(\mathbf{q}-\mathbf{q}')}{(\mathbf{q}^2+k\Theta_E^2)(\mathbf{q}'^2+k^2\Theta_E^2)} \\ &= \sum_{i,|n|,k}\{\frac{\sqrt{a_i}e^{-b_i\,q^2}}{(\mathbf{q}^2+k^2\Theta_E^2)}\frac{(\sqrt{b_i}\,q)^{|n|+2k}}{\sqrt{k!(k+|n|)!}}\,e^{in\phi}\}\times\{\mathbf{q}',\phi'\}^*\,, \end{aligned} \tag{5.59}$$

in close analogy to the phonon case [10].

An alternative factorization of the mutual object transparency can be obtained in real space [9]. Unfortunately, this method depends strongly on the analytical form of the scattering amplitude and necessitates restrictions for the numerical values of the fitting parameters which can not be guaranteed easily. The Fourier space factorization is more general and leads to much simpler formulas for the partial transmission functions, as we have shown above.

The result (5.59) has been obtained with the assumption of an average energy loss $\bar{\omega}$ for all atomic excitations. This excitation energy depends on the atomic number of the atom. To derive a more accurate approximation, we must consider that the electron energy loss spectrum (EELS) of each atom is a continuous function of the excitation energy. In a first approximation we describe this spectrum by a delta function $\delta(\omega - \omega_{ex})$, where the specific excitation energy $\omega_{ex} = \bar{\omega}$ is chosen as the average energy loss of the scatterer. The parameter ω_{ex} enters the expression (5.57) through the definition of the characteristic scattering angle Θ_E. The smaller the mean energy loss, the more delocalized is the scattering process. Therefore, we can drop the assignment $\omega_{ex} = \bar{\omega}$ and reinterpret ω_{ex} as a formal parameter quantifying the degree of localization of the scattering process.

This interpretation allows us to obtain an improved approximation for the term $\tilde{\mu}_{11}$ of each atom. For this purpose we use the energy loss spectrum $f_j(\omega_{ex})$ of the j-th atom which can for example be taken from the EELS atlas [51]. Moreover, we replace the average energy loss $\bar{\omega}$ by the energy loss ω_{ex}. In addition we substitute $f_j(\omega_{ex})$ for $\delta(\omega-\bar{\omega})$ in relation (5.56). By taking the Fourier transform of the resulting expression,

we obtain the improved approximation

$$\tilde{\mu}_{11}^{in,j}(\mathbf{q},\mathbf{q}',\tau) \approx \left(\frac{4\pi\,\alpha}{\beta}\right)\int f_j(\omega_{ex})\,\frac{e^{-i\omega_{\rm ex}\tau}}{\mathbf{K}^2\mathbf{K}'^2} \tag{5.60}$$

$$\times\left\{F_j(\mathbf{q}-\mathbf{q}') - \frac{1}{Z_j}\,F_j(\mathbf{q})F_j(\mathbf{q}')\right\}\,d\omega_{\rm ex}\;. \tag{5.61}$$

This formula is especially useful for simulating energy–filtered images obtained in the case of a rather large energy window.

Inelastic partial waves emanating from different atoms are incoherent with each other. To account for this incoherence we must sum up the inelastic image intensities of all atoms. The incoherent superposition of the partial waves emanating from atoms situated in different slices is guaranteed by the generalized multislice formalism. In the case of a crystalline specimen the summation over the atoms situated in the same slice reduces to a sum over all atoms of the unit cell because of the translational symmetry of the crystal lattice. For crystalline structures with a small unit cell we can perform this summation directly. For amorphous object details, like interfaces, defect structures or for biological specimens we must employ an alternative method. To efficiently implement the generalized multislice procedure, the random phase method [9, 10] can be used to compute sums of the form

$$I(\mathbf{q}) = \sum_{j=1}^{M}\Phi_j^*(\mathbf{q})\Phi_j(\mathbf{q})\;. \tag{5.62}$$

Here Φ_j, $j=1,\ldots,M$ are arbitrary complex–valued functions. We assume a set α_{jk}, $j=1,\ldots,M$ and $k=1,\ldots,N$ of equally distributed random phases within the range $0\le\alpha_{jk}<2\pi$. For each k we define the expression

$$I_k(\mathbf{q}) = \left(\sum_{i=1}^{M}\Phi_i(\mathbf{q})\;e^{i\alpha_{ik}}\right)\left(\sum_{j=1}^{M}\Phi_j(\mathbf{q})\;e^{i\alpha_{jk}}\right)^*\;. \tag{5.63}$$

The complex exponential factors $e^{i\alpha_{ik}}$ are called random phase factors. The value of $I_k(\mathbf{q})$ differs from $I(\mathbf{q})$ only by the contribution of the mixed factors originating from the product in (5.63):

$$I_k(\mathbf{q}) - I(\mathbf{q}) = \sum_{i=1}^{M}\sum_{j=1}^{i-1} 2\;Re\left\{\Phi_i(\mathbf{q})\Phi_j^*(\mathbf{q})\;e^{i(\alpha_{ik}-\alpha_{jk})}\right\}\;. \tag{5.64}$$

The terms on the right hand side cancel out if we average I_k over a series of different sets of random phases α_{jk}, $k=1,\ldots,N$. As a result we find

$$I(\mathbf{q}) \approx \frac{1}{N}\;\sum_{k=1}^{N} I_k(\mathbf{q}). \tag{5.65}$$

In the case of the generalized multislice formalism the function Φ_j represents a modified partial wave of the inelastically scattered wave emanating from the jth atom. Since we employ a linear algorithm to calculate these functions from the input data, we can calculate any linear combination of these functions by applying the generalized multislice formalism to an appropriate linear combination of the input data. Therefore, we need only a single multislice calculation to evaluate equation (5.63) for a fixed k. In this case the numerical effort for determining the intensity $I(\mathbf{q})$ is proportional to the number of sets of random phases N, which is much smaller then the number of different inelastic scattering events occurring in one slice. Therefore the random phase method is especially useful if M is large and the calculation of the functions Φ_j in (5.62) is very time consuming. This method is very advantageous for non periodic objects where the multislice algorithm requires the implementation of large super cells. The number N of sets of random phases, which is necessary to obtain a sufficient degree of accuracy must be determined by numerical experiments. For crystalline specimens the result of the exact calculation agrees very well with that obtained by means of the random phases approximation.

5.4 Characterization of the microscope

To obtain a realistic result the image simulation has to correctly account for the individual elements of the electron microscope. Hence the illumination system and the properties of the objective lens must be considered with sufficient accuracy. For both parts of the microscope the simulation has to account for the phase shifts owing to the imperfect and possibly misaligned electro–magnetic lenses. The information limit of the microscope is determined by the characteristics of the source and by other incoherent perturbations which influence the coherence of the wave field, as already discussed in chapter 4.

All electron–optical systems used in high–resolution imaging are considered as isoplanatic [54]. Hence the aberrations of the objective lens and of the condenser lenses can be described by a phase factor $\mathrm{e}^{i\gamma(\mathbf{q})}$ at the back focal plane [33, 52]. This phase factor depends predominantly on the defocus, the spherical aberration, and the chromatic aberration of the lenses. To account for these aberrations in the simulation more precisely we introduce the generalized mutual aperture function [35, 10]

$$M_A(\mathbf{q},\mathbf{q}') = A(\mathbf{q})A(\mathbf{q}')\exp\left(i\gamma(\mathbf{q},\kappa) - i\gamma(\mathbf{q}',\kappa)\right) \tag{5.66}$$

in the back focal plane. The parameter κ denotes the relative energy deviation of the imaging electron owing to the finite energy width of the source and owing to inelastic scattering. The transmission of the mutual coherence through an ideal lens with focal length f is described in the thin lens approximation by the mutual transparency

function of the lens situated in the midplane of the lens [33]

$$M_L(\rho,\rho') = \mathrm{e}^{-i\frac{k}{2f}(\rho^2-\rho'^2)} \,. \tag{5.67}$$

To calculate the mutual aperture function of a real microscope we expand the eikonal expression $\gamma = \gamma(\mathbf{q},\varepsilon)$ appearing in the exponent of equation (5.66) in a Taylor series with respect to the lateral coordinate $\mathbf{q}$ and the chromatic parameter κ. For an uncorrected microscope only a few terms in this expansion are important. In the case of a corrected microscope the higher–order terms and the parasitic aberrations due to misalignment gain importance. Table 5.1 gives an overview over the possible axial aberrations upto fifth order [54]. Considering that the axial aberration depend on a two–dimensional lateral vector a combinational calculation yields that a set of 25 real constants is required to quantify all these aberrations uniquely. The focus spread owing to the chromatic aberration and to incoherent perturbations requires further two real parameters.

Aberration	Eikonal term		
two–fold astigmatism	$\frac{1}{2}\,\vartheta\vert^2$	A_1	$\cos(2(\phi-\phi_{A_1}))$
defocus	$\frac{1}{2}\,\vartheta\vert^2$	C_1	
three–fold astigmatism	$\frac{1}{3}\,\vartheta\vert^3$	A_2	$\cos(3(\phi-\phi_{A_2}))$
second–order axial coma	$\vartheta\vert^3$	B_2	$\cos(\phi-\phi_{B_2})$
four–fold astigmatism	$\frac{1}{4}\,\vartheta\vert^4$	A_3	$\cos(4(\phi-\phi_{A_3}))$
third–order spherical aberration	$\frac{1}{4}\,\vartheta\vert^4$	C_3	
third–order star aberration	$\vartheta\vert^4$	S_3	$\cos(2(\phi-\phi_{S_3}))$
five–fold astigmatism	$\frac{1}{5}\,\vartheta\vert^5$	A_4	$\cos(5(\phi-\phi_{A_5}))$
fourth–order axial coma	$\vartheta\vert^5$	B_4	$\cos(\phi-\phi_{B_4})$
three–lobe aberration	$\vartheta\vert^5$	D_4	$\cos(3(\phi-\phi_{D_4}))$
six–fold astigmatism	$\frac{1}{6}\,\vartheta\vert^6$	A_5	$\cos(6(\phi-\phi_{A_5}))$
fifth–order spherical aberration	$\frac{1}{6}\,\vartheta\vert^6$	C_5	
fifth–order star aberration	$\vartheta\vert^6$	S_5	$\cos(2(\phi-\phi_{S_5}))$
four–lobe aberation	$\vartheta\vert^6$	D_5	$\cos(4(\phi-\phi_{D_5}))$
coherent chromatic aberration	$\vartheta\vert^2$	C_c	θ_E
chromatic focus spread	$\frac{1}{2}\,\vartheta\vert^2$	C_c	κ
perturbative focus spread	$\vartheta\vert^2$	C_ε	κ

Table 5.1: *List of the eikonal terms corresponding to the axial aberrations up to fifth order. The aberrations are due to the unavoidable imperfection of the lenses or due to misalignment. Each contribution has a characteristic multiplicity and order. The aperture coordinates are defined by $\vartheta = f|\mathbf{q}|$, where f denotes the focal length of the objective lens and by the polar angle ϕ. The parameter κ accounts for the incoherent focus spread. To obtain their contribution to the phase shift γ all terms listed in this table must be multiplied by the wave number k_0.*

Using the equations (5.67) and (5.66) together with the four–dimensional free–space propagator (4.8), the propagation of the mutual spectral density through the microscope can be separated into a free–space propagation from the exit plane $z = z_B$ of the object to the midplane z_L of the objective lens, a multiplication with the mutual transparency function of the ideal lens M_L, a Fresnel propagation from the lens to the back focal plane z_A of the lens, a multiplication with the generalized mutual aperture function M_A and finally a Fresnel propagation to the image plane z_I. In mathematical terms the image intensity in the image plane has the form

$$
\begin{aligned}
I(\rho) &= \int \Gamma(\rho,\rho,\omega;z_I)\, W(\hbar\omega)\, d\omega \\
&= \frac{1}{\lambda^6 g^2 f^4 M^2} \int \ldots \int \Gamma(\rho_O,{\rho'}_O,\omega;z_O)\, W(\hbar\omega) \\
&\quad \times \underbrace{\exp\left\{ i\frac{k}{2g}\left[(\rho_L-\rho_O)^2-({\rho'}_L-{\rho'}_O)^2\right]\right\}}_{\text{prop. from object to lens}} d^2\rho_O d^2{\rho'}_O \\
&\quad \times \underbrace{\exp\left\{ -i\frac{k}{2f}\left[\rho_L^2-{\rho'}_L^2\right]\right\}}_{\text{ideal lens}} \underbrace{\exp\left\{ i\frac{k}{2f}\left[(\rho_A-\rho_L)^2-({\rho'}_A-{\rho'}_L)^2\right]\right\}}_{\text{prop. from lens to backfocal plane}} d^2\rho_L d^2{\rho'}_L \\
&\quad \times \underbrace{A(\rho_A)\, A({\rho'}_A) \exp\left\{-i\gamma(\rho_A,E)+i\gamma({\rho'}_A,E)\right\}}_{\text{generalized mutual aperture function}} \\
&\quad \times \underbrace{\exp\left\{ i\frac{k}{2(b-f)}\left[(\rho-\rho_A)^2-(\rho'-{\rho'}_A)^2\right]\right\}}_{\text{prop. form backfocal plane to image plane}} d^2\rho_A d^2{\rho'}_A\, d\omega\ , \qquad (5.68)
\end{aligned}
$$

where M denotes the magnification of the image [33]. The two–dimensional integration with respect to ρ_L can be performed analytically. The integration with respect to the energy $E = \hbar\omega$ extends over the spectral range of the image–forming electrons. The transmitted energies are selected by the energy window function $W(E)$. In the case of an energy–filtering transmission electron microscope (EFTEM) this range is determined by the position and width of the energy window of the energy filter. Equation (5.68) can we evaluated efficiently by a Fourier transformation from the exit plane of the object onto the back focal plane, a multiplication with the generalized mutual object transparency and a subsequent Fourier transformation from the back focal plane onto the image plane [33].

The illumination mode in an electron microscope is determined by a variable condenser system. Nevertheless a realistic condenser system is quite complicated, for the theoretical investigation it is sufficient to discuss a simple two–lens condenser. The condenser is used to form the incident wave in front of the object. The field and the illumination aperture of the condenser determine the illuminated area and the area for the surface of the effective source which irradiates the object. This size of the effective

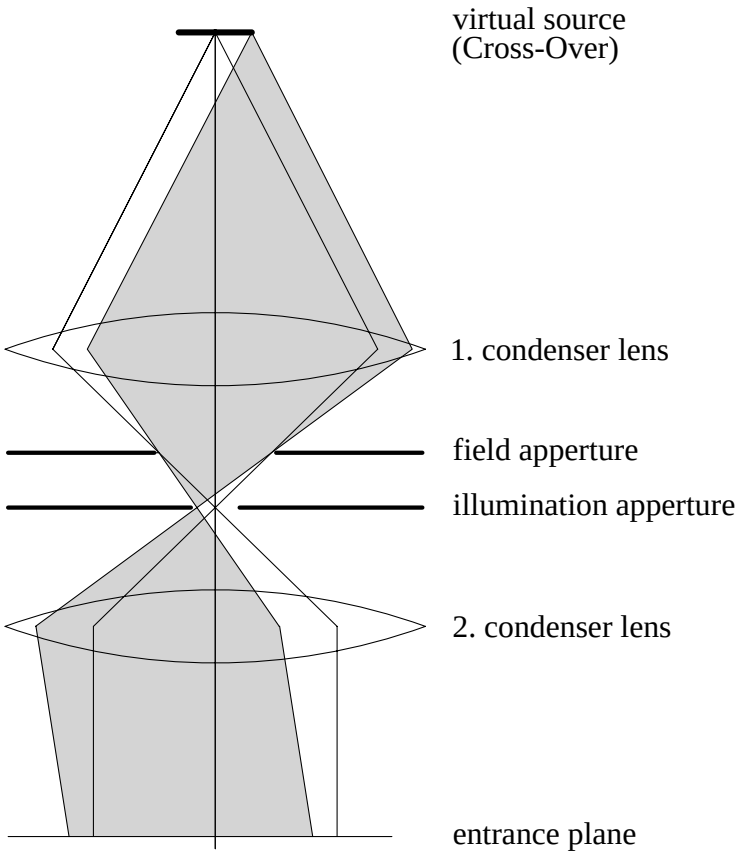

Figure 5.2: *Variable two–lens condenser system for Köhler illumination. The lateral coherence of the incident wave filed can be adjusted by the condenser aperture. For the CTEM mode the object is illuminated by a cone of mutually incoherent tilted plane waves.*

source together with the energy width of the source determine the spatial and temporal coherence of the incident wave field, respectively, as we have already discussed in chapter 4. Other incoherent perturbations of the optical transmission system decrease the temporal coherence further. Hence these effects can be described by an additional perturbative focus spread superimposed onto the chromatic focus spread. This parameter can be used to match the information limit considered in the simulation with that of the real instrument. The numerical integration over the energy spectrum of the source is performed most efficiently employing a Gauss–Hermite integration rule [50]. This method optimally accounts for the Gaussian shape of the spectral density. Hence already a five–point integration provides a highly accurate result [10].

In the conventional transmission electron microscope (CTEM) the first condenser lens images the effective source onto the front focal plane of the second condenser lens. This mode effectuates plane illumination and is called Köhler illumination. Due to the finite size of the source the object is illuminated by a cone of mutually incoherent plane

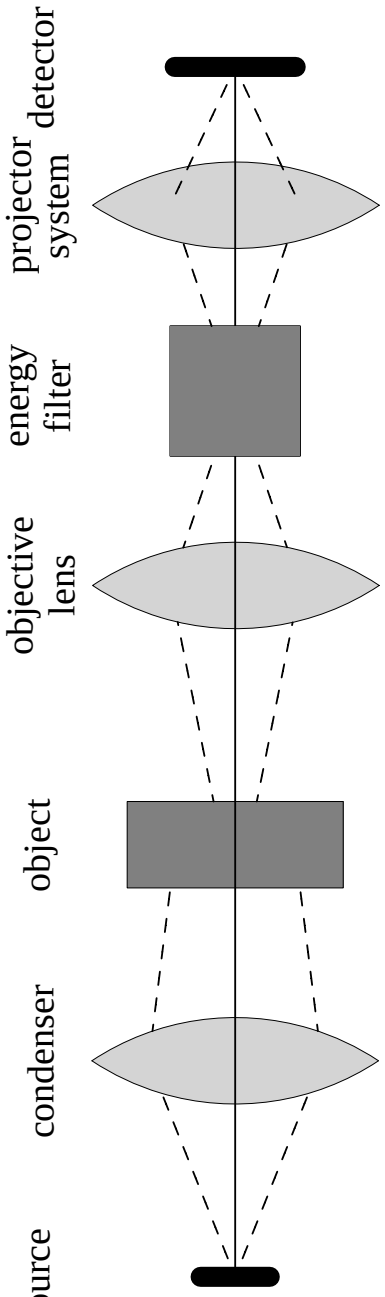

propagation processes	lateral and temporal coherence	illumination mode	elastic and inelastic scattering	imaging, phase shift	energy selection	intensity recording
parameters affecting the image	source size, energy width	illumination aperture, phase shift	atomic structure, mixed dynamic form factor	lens aberrations, defocus	width of energy window	saturation, crosstalk between detector elements
present state of simulation	monochromatic point source, incoherent superposition of images	small tilt angle, entrance wave function	transmission functions for elastic, quasi elastic and inelastic scattering	aperture function, transmission function of the optic system	restriction to specific scattering processes	nonlinear response function, point spread function

Figure 5.3: *Schematic overview of the propagation processes within an EFTEM and of the parameters affecting the image formation. The bottom row of the table lists the capabilities of the generalized multislice method.*

waves. The half angle of this illumination cone is termed the illumination semi–angle. If the first condenser lens images the effective source onto the plane conjugated to the entrance plane of the object a probe is formed on the surface of the object. This critical illumination is realized in a scanning transmission electron microscope (STEM). The finite extension of the source leads to an incoherent superposition of laterally shifted electron probes. This shows that in both cases, for CTEM and STEM simulations, the degree of coherence of the incident wave field may influence the recorded image. A simple two–lens condenser is depicted in figure 5.2.

For plane illumination in the CTEM mode the wave field at the entrance plane adopts the form

$$\Gamma(\rho,\rho',\omega;z_A) = I_S\, p(\omega) \int_{|q_S|<\theta_S} \exp(-i\mathbf{q}_S(\rho-\rho'))\, d\mathbf{q}_S \;, \tag{5.69}$$

where θ_S denotes the illumination semi–angle and I_S is a normalization constant. The axial aberrations of the condenser system can be neglected, since the semi-convergence angle is very small, typically $\theta_A < 1$ mrad and does not substantially exceed the paraxial domain. Hence to account for spatial incoherence due to the finite size of the source an integration over a set of images corresponding to different tilt angles must be performed. Since the scattering at a crystal depends critically on the tilt angle relative to the zone axis a full multislice calculation must be performed for each tilt angle. This tedious procedure also correctly considers the influence of the residual aberrations of the objective lens owing to the tilting process.

For critical illumination less numerical effort is needed. In this case each point of the source corresponds to a laterally shifted probe position at the exit plane of the specimen. The probe function at the specimen depends on the aberrations of the objective lens of the STEM — in our simplified theoretical model this lens corresponds to the second condenser lens — adopts the form

$$\Gamma(\rho,\rho',\omega;z_A) = I_S\, p(\omega) \int_{|\rho_S|<R_S} \iint M_A(\mathbf{q},\mathbf{q}')\, \mathrm{e}^{-i(\mathbf{q}(\rho-\rho'_S)-\mathbf{q}'(\rho'-\rho'_S))} d^2\mathbf{q} d^2\mathbf{q}'\, d^2\rho_S \;. \tag{5.70}$$

Again I_S denotes a normalization constant. Performing the integration with respect to ρ_S does not yield any simplification, but the integration over an appropriate set of shifted probe function is equivalent to a convolution of the resulting image with the source profile and can be performed after the multislice calculation.

The present implementation of the generalized multislice software developed during the last years is illustrated in figure 5.3. In this table the different parts of the EFTEM are depicted together with the appropriate theoretical concepts used to simulate their behaviour. From this overview it is apparent that, although the process of image formation in the electron microscope is quite complex, the information necessary for the simulation are restricted to a small set of parameters. For the correct interpretation of

simulated data it is crucial to report these parameters. The multislice calculation is performed on finite dimensional image vectors employing the FFT method [47, 11]. Hence the size of these vectors, the size of the chosen super cell, and the slice thickness are further important parameters of the calculation. They must be chosen carefully to guarantee the convergence of the multislice method and to exclude systematic errors [11]. Unfortunately, the numerical expenditure of the coherence function multislice method is still rather high for all realistic objects. Nevertheless, the ongoing improvement of high–speed computers continuously expands the range of applicability of this procedure.

5.5 Diffraction patterns of thick objects

To demonstrate the feasibility of the generalized multislice formalism we employ this calculation method to the simulation of diffraction patterns of crystalline samples. In these patterns inelastic scattering can be observed as a characteristic background. First we consider a silicon (Si, Z=14) crystal. The 110 nm thick crystal is illuminated by a plane wave in crystallographic $\langle 110 \rangle$ direction with an acceleration voltage of 200 kV. To obtain the projected potential we subdivide each unit cell of the diamond lattice into two equally thick subslices to account for the higher–order Laue zone contribution to the scattering. The dimensions of the cubic unit cell are $a_0 = 3.83$ Å , $b_0 = 5.42$ Åand $c = 3.83$ Å. Hence for the slice thickness we find $\Delta z = 1.92$ Å. Accordingly, the complete object consists of 574 slices. For the characteristic energy loss we have assumed $\Delta E = \hbar\bar{\omega} = 6ZeV = 84eV$ and for the vibration amplitude of silicon we use the literature value of $u_{Si} = 10.95$ pm. To consider the incoherence between the partial waves scattered inelastically at different atomic sites correctly a super cell of 7×5 unit cells is sufficient to avoid artefacts owing to the discrete Fourier transformation. The dimensions of the super cell in real space are $a = 26.83$ Å and $b = 27.10$ Å, respectively. Hence the calculation can be performed on a rectangular basis with a favorable aspect ratio of nearly one (a/b = 0.99). Only a slight correction of the aspect ratio is required after the calculation. To prevent aliasing effects owing to the discrete Fourier transformation the band width of the calculation must be limited to $2/3$ of the maximum sampling frequency. Hence for a 512×512 image vector the maximal scattering vector in the calculation is $|\mathbf{q}_{\max}| = 39.6/$ Å. This corresponds to an maximum scattering angle of 158 mrad for 200 kV electrons. One image vector requires 2 MByte of computer memory, For the complete calculation of the elastic and inelastic diffraction patterns about 3 days of CPU time on a modern workstation (Digital Alpha 21164A/600) have been consumed.

Figure 5.4 shows the atomic structure of a single slice of the super cell together with the result of a conventional multislice simulation of purely elastic scattering at the time–averaged object potential.

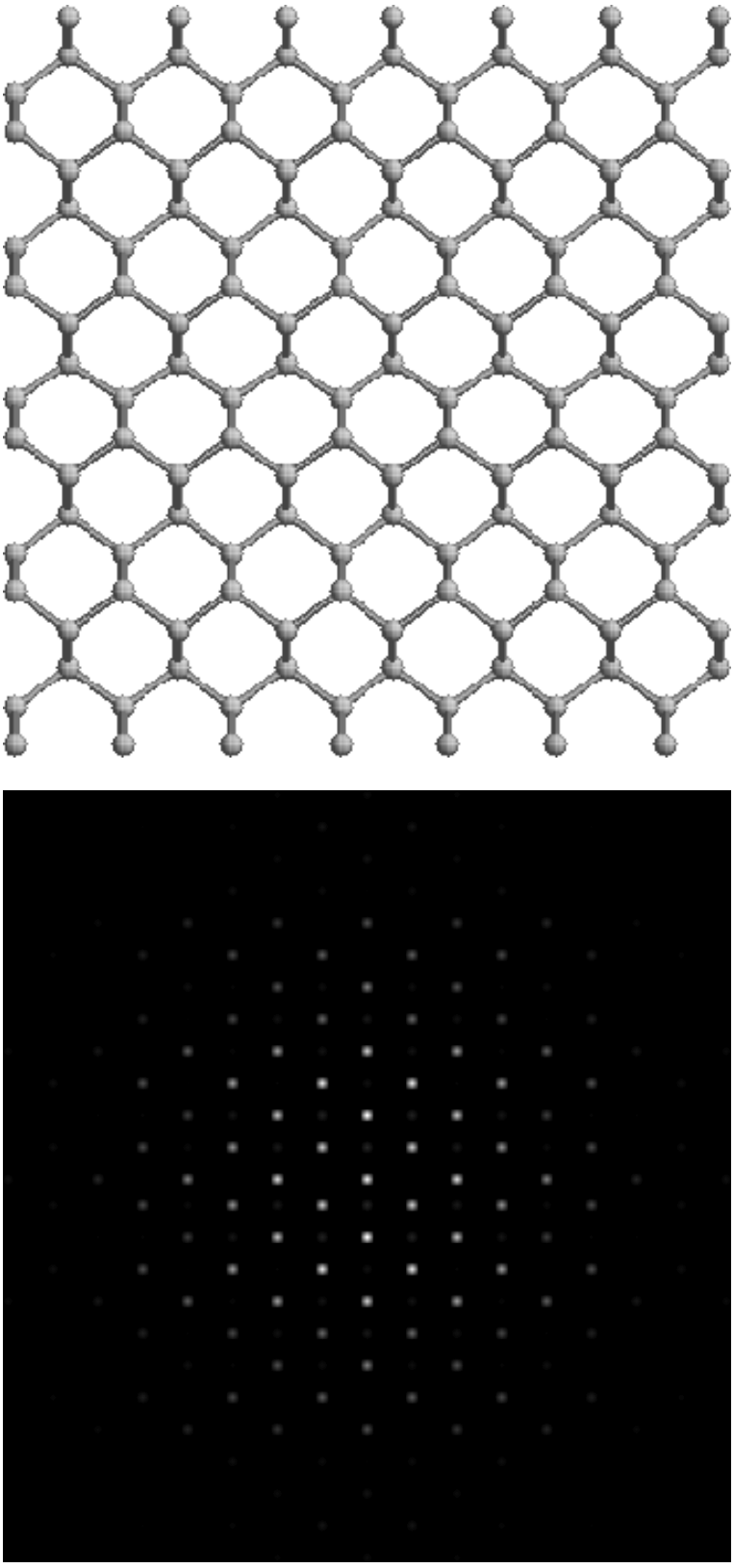

Figure 5.4: *Top image: atomic structure of a single slice of a Si* $\langle 110 \rangle$ *super cell. Bottom image: Result of a conventional multislice simulation of a* 110 *nm thick Silicon crystal considering only elastic scattering. The calculation has been performed with the appropriate Debey–Waller factor.*

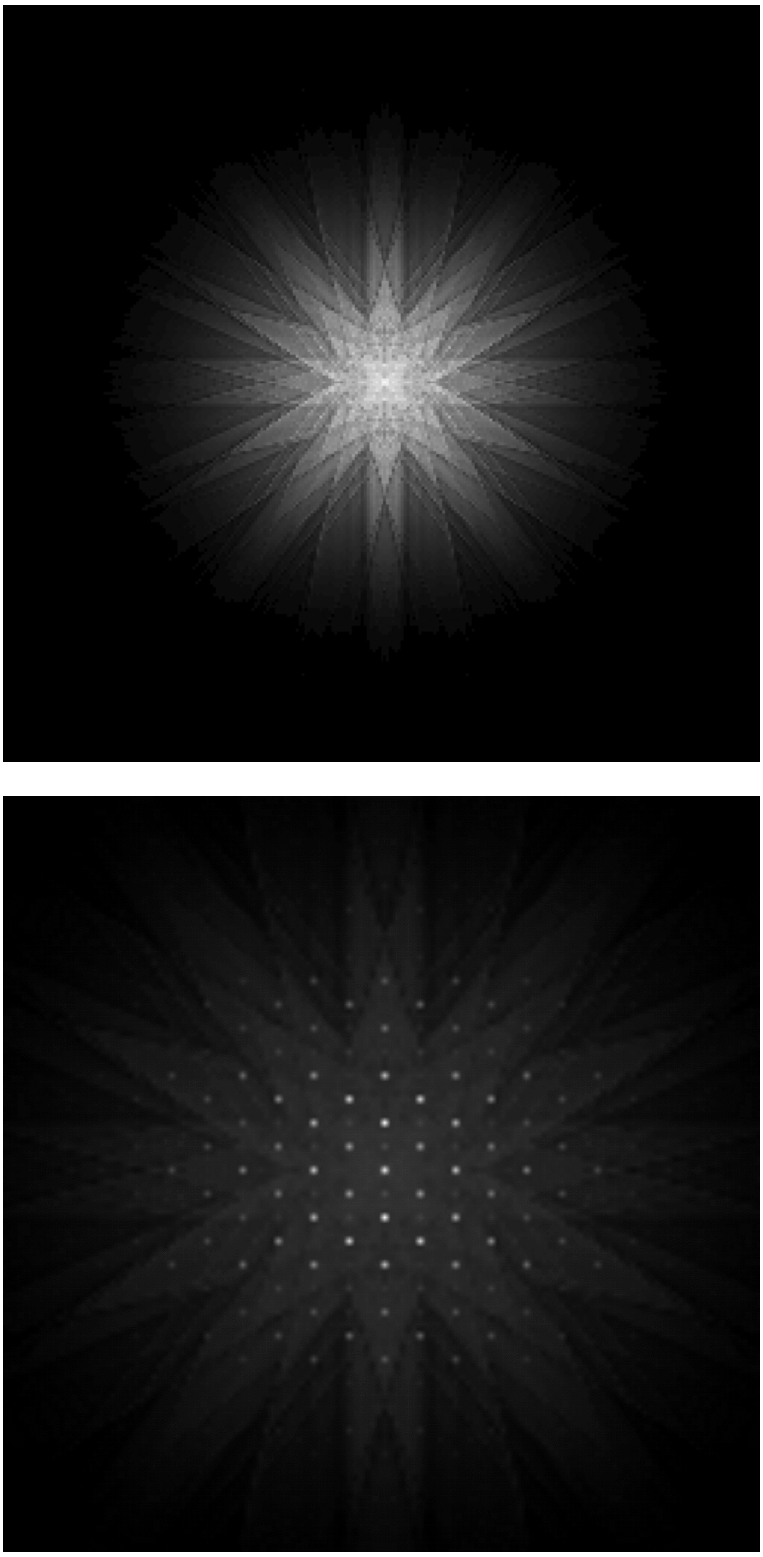

Figure 5.5: *Top Image: Simulated thermal diffuse back ground pattern for Silicon in crystallographic* $\langle 110 \rangle$ *orientation. Thermal diffuse scattering is described by the Einstein model. The Kikuchi band representing the symmetry of the specimen are clearly visible. They result from mixed thermal diffuse and elastic multiple scattering. Bottom image: Simulated zero–loss pattern with thermal diffuse background.*

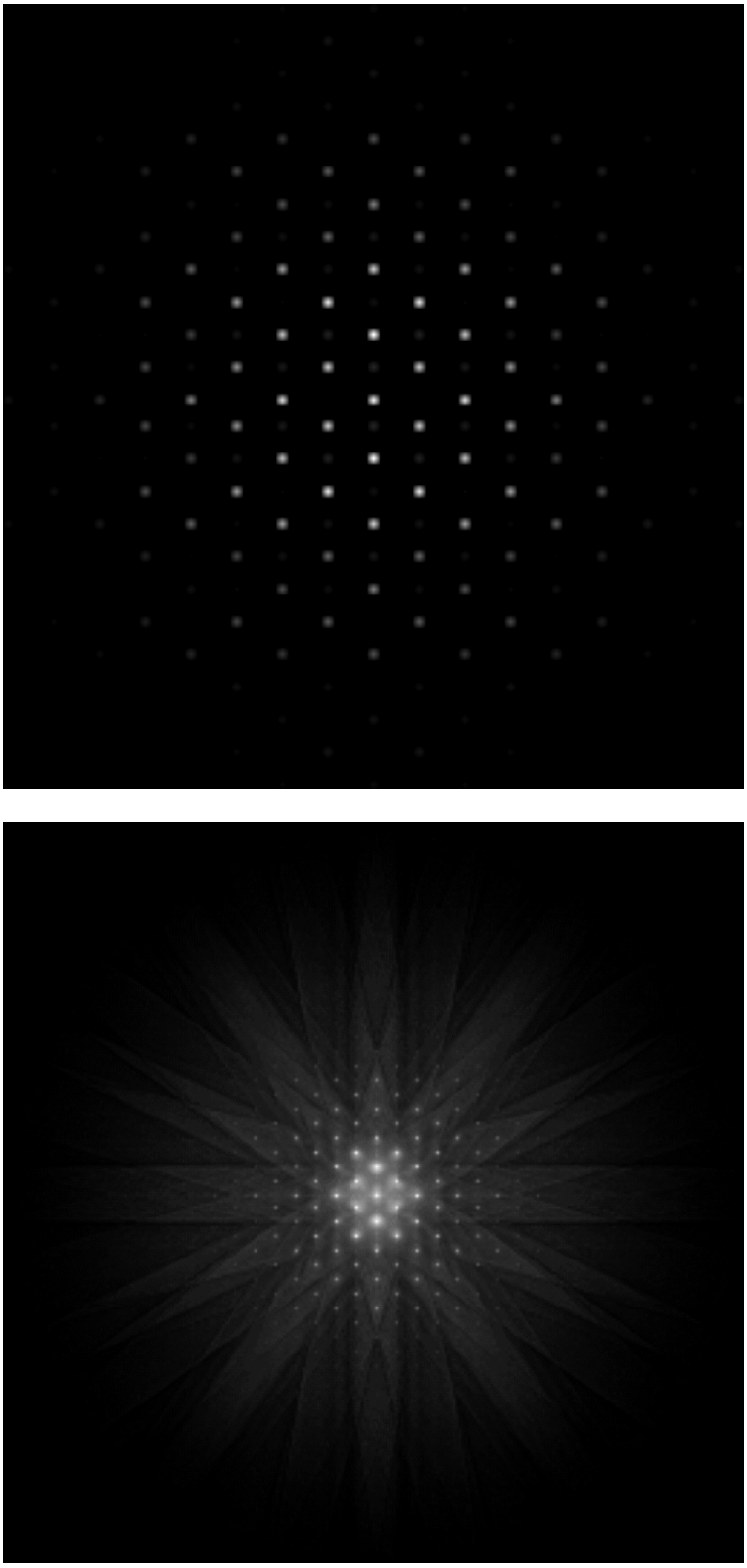

Figure 5.6: *Comparison between the results of the conventional multislice method (top image) and the coherence function method (bottom image). Both diffraction patterns are calculated for a 110 nm thick Silicon crystal in* $\langle 110 \rangle$ *direction.*

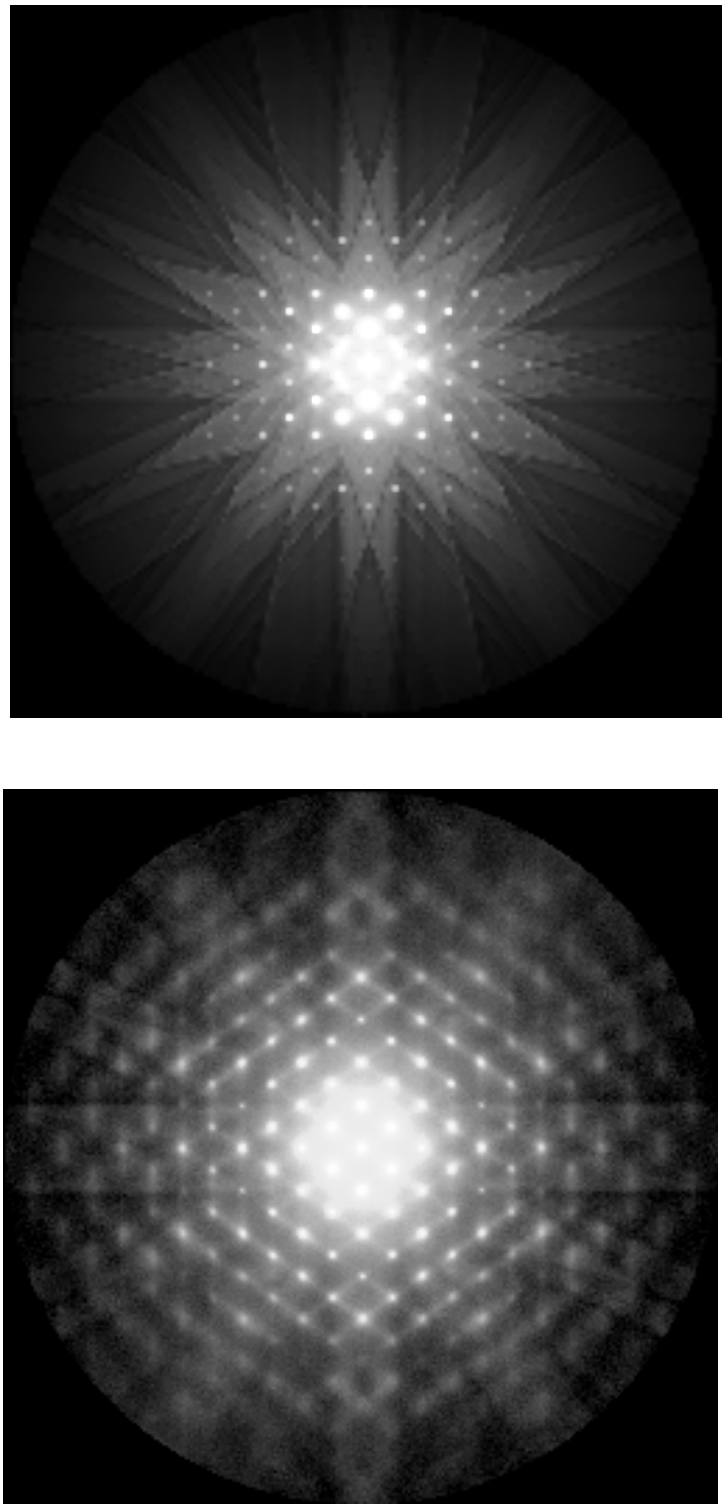

Figure 5.7: *Comparison between the results of the coherence function method (top image) and an experimental diffraction pattern of an approximately* 110 *nm thick Silicon crystal. The saturation characteristic of the detector has been considered for the simulation to make a direct comparison possible. [Experimental image courtesy of W.D. Rau and P. Schwander, IHP Frankfurt/Oder, Germany.]*

All grey scale images of diffraction patterns are scaled logarithmically

$$I' = \log(1 + C_0\, I)\ , \quad C_0 > 0\ . \tag{5.71}$$

This is required due to the enormous dynamical range of the recorded signal in electron diffraction. For elastic scattering the diffracted intensity is completely contained in sharp Bragg spots as one would expect from the kinematical theory. No intensity can be found between the spots where the diffraction condition is not fulfilled.

The mutual coherence function method can be used to calculate an unfiltered diffraction pattern employing the Einstein model and the Raman–Compton approximation. The calculation results in three different contributions to the unfiltered diffraction pattern. First the elastic diffraction pattern shown in figure 5.4, where only the Debey–Waller factor accounts for the difference between the time–averaged dynamic potential and the static potential of the object. This simply results in an exponential damping of the outer Bragg peaks. The second pattern we can obtain is the thermal diffuse background pattern. This is shown in figure 5.5. It is important that, although we can calculate a pure TDS pattern, it is not possible to separate the thermally diffuse scattered electrons from the elastically scattered electrons by a conventional energy filter due to their very small energy loss. The best experimentally obtainable result is a zero–loss filtered diffraction pattern. This pattern contains the sum of the elastically scattered and the thermal diffusely scattered electrons. The third diffraction pattern simulated is the energy–loss pattern. It contains all electrons which have made an electronic excitation in the object and, therefore, suffered a non negligible energy loss. This results in a diffuse diffraction background plus a significant broadening of the Bragg spots. For both the zero–loss and the energy–loss contribution multiple elastic scattering in combination with inelastic scattering must be considered. This conclusion is brought about by the results of the simulation since both contribution due to inelastic scattering clearly show the symmetry of the crystal lattice and hence must contain coherent information about the spatial structure of the object. This illustrates what we have already proved in chapter 4: In electron microscopy the concepts of inelastic scattering and incoherent imaging can never be used synonymously. The superposition of the zero–loss and the energy loss patterns results in an unfiltered diffraction pattern which can be recored in a high–resolution CTEM without employing an imaging energy filter. A direct comparison between the coherence function method and the conventional multislice method is given in figure 5.6.

Recording diffraction patterns experimentally is a difficult task due to the enormous dynamic range of the intensity in such patterns. One promising possibility is to use imaging plates with a dynamic range of nearly 20 bit. An ordinary CCD camera with less than 12 bit dynamic range is completely insufficient. Nevertheless, we have attempted to make at least a qualitative comparison between the simulated unfiltered diffraction patterns and experimental diffraction pattern recorded on imaging plates. In the experimental images the intensity of the central spots is obviously oversatu-

rated. Because the saturation curve of the imaging plates is approximately known we can apply the same saturation to the simulated images and then compare the double–logarithmically scaled intensities. Figure 5.7 presents the comparison between the diffraction patterns calculated with the coherence function method and an experimentally obtained image for a silicon specimen in $\langle 110 \rangle$ orientation of approximately the same thickness (110 ± 11 nm). The thickness has been determined by means of electron holography. The result of the comparison shows that the characteristic background intensity visible in the experimental image due to thermal diffuse and inelastic scattering is well reproduced by the simulation shown in the bottom image. The symmetric structuring of the diffuse background is clearly visible in the results of the coherence function method. This indicates that the combination of elastic and inelastic scattering is considered correctly by the theory. The experimental diffraction pattern clearly shows streaks between the outer Bragg spots. This feature is missing in our simulation. This is because the Einstein model does not account for nearest–neighbour correlations existing between the vibration of the atoms of a crystal lattice. Unfortunately, it must be assumed that these correlation between the atomic vibrations extend quite far over the length of five or lattice constants. This behaviour is due to the non–local characteristic of the phonon modes of a crystal lattice. Nevertheless the extension of the coherence function method to interatomic correlations is possible, at least in principle. However, the numerical effort increases enormously because of the large number of mixed terms contributing to the covariance μ_{11} of the dynamic object potential in this case.

For convergent beam electron diffraction (CBED) the background intensity due to inelastic scattering is more important. The finite convergence angle of the illumination broadens the Bragg spots and reduces the dynamics of the intensity in the diffraction patterns. We have performed simulations for a 49 nm thick Silicon (Si, $Z = 14$) crystal in crystallographic $\langle 111 \rangle$ orientation. For this specimen the dimensions of the unit cell are $a_0 = 3.83$ Å, $b_0 = 3.83$ Å, and $c_0 = 9.39$ Å. The angle enclosed by the base vectors is $\pi/3$ rad and hence it is convenient to perform the calculation on a hexagonal grid. Using a hexagonal 5×5 super cell results in the real space dimensions $a = b = 19.16$ Å. Each unit cell must be subdivided into three sub slices. Hence the slice thickness is $\Delta z = 3.13$ Å.

We have used 512×512 image vectors. Accordingly, the maximum scattering vector considered in the simulation is $|\mathbf{q}_{\max}| = 56/\text{Å}$. This corresponds to a maximum scattering angle of 330 mrad for an acceleration voltage of $U_0 = 100$ kV (wave length $\lambda = 3.70$ pm). Again the band width is limited to $2/3$. The simulation with the coherence function multislice has been restricted to zero–loss filtered diffraction patterns. In convergent beam electron diffraction the specimen is illuminated by a focused probe. Hence the axial aberrations of the probe forming lenses must be considered. We assume an uncorrected microscope with spherical aberration $C_3 = 3.3$ mm, defocus $C_1 = 135.4$ nm, and an objective aperture of 8.0 mrad. This setup approximately corresponds to Scherzer conditions [53]. Figure 5.8 shows the simulated elastic CBED

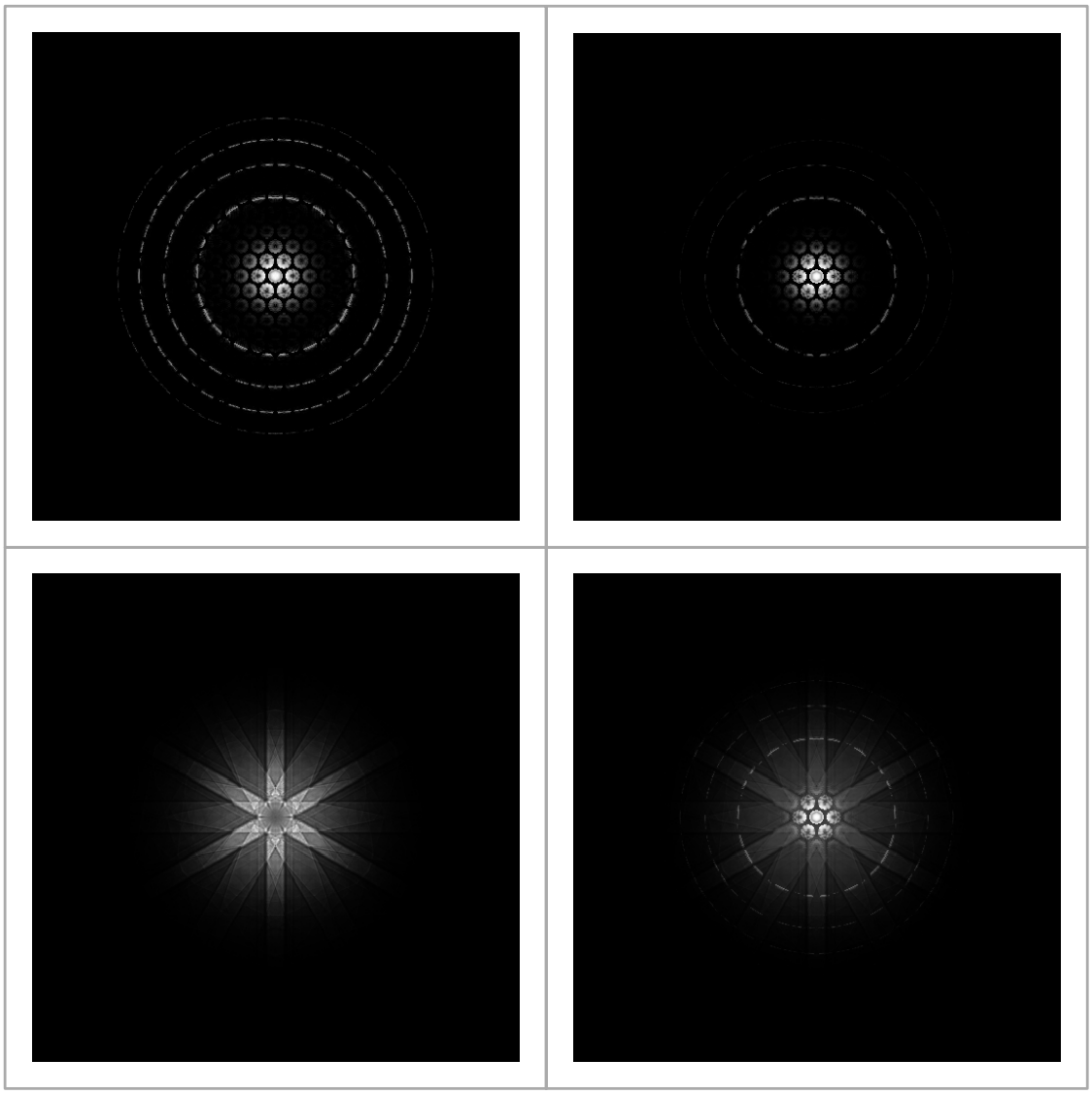

Figure 5.8: *Simulation of zero–loss filtered convergent beam electron diffraction (CBED) patterns for a* 49 *nm thick silicon crystal in* $\langle 111 \rangle$ *orientation. The imaging parameters are* $U = 100$ *kV,* $C_s = 3.3$ *mm and an objective aperture of* $\vartheta_A = 8$ *mrad. The top images show the result of a conventional multislice simulation. The left image is calculated without considering the absorption potential for thermal diffuse scattering, whereas it is included in the image on the right side. At the bottom the results of the generalized multislice method are shown. The right image shows the complete result of the simulation considering thermal diffuse scattering. The left–hand image shows only the diffuse background resulting from this scattering.*

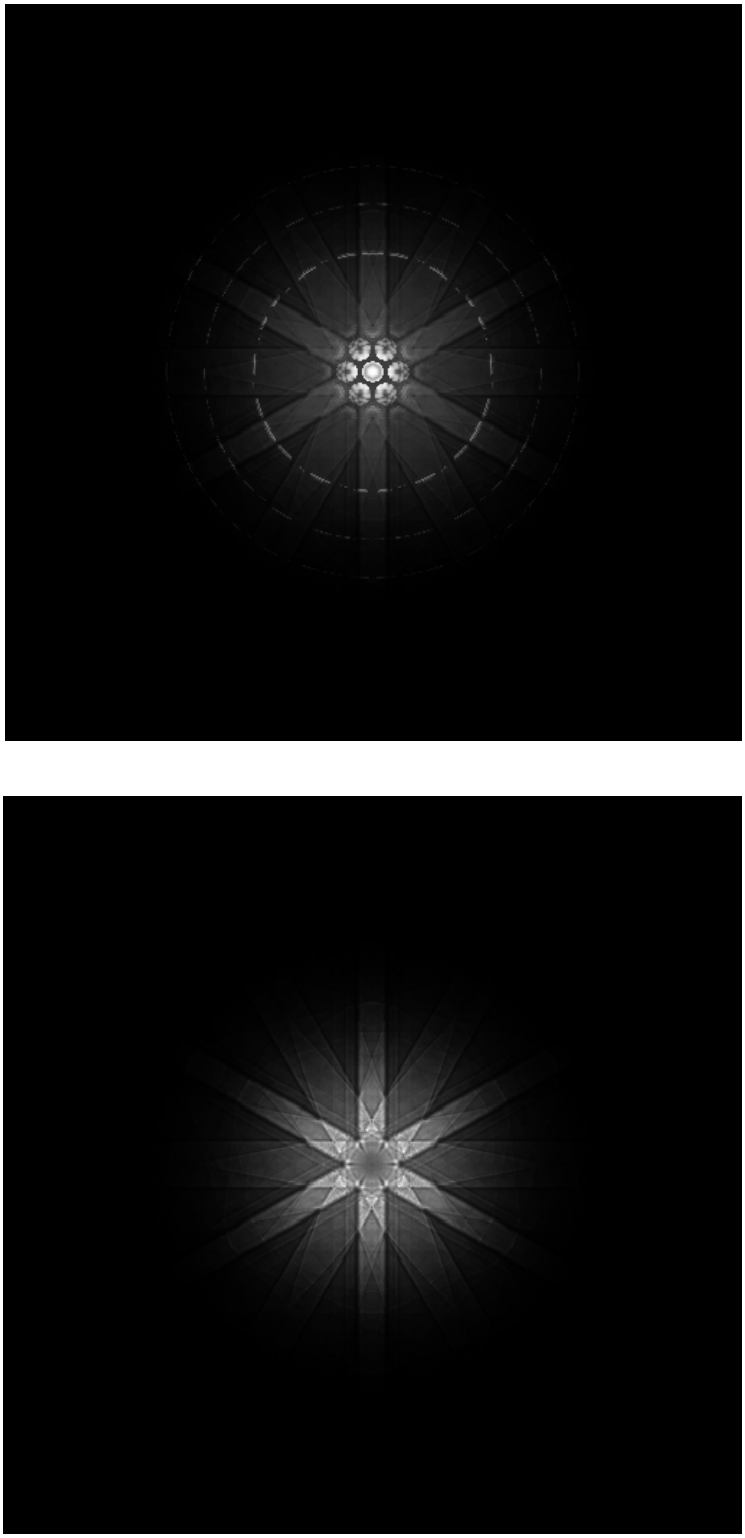

Figure 5.9: *Simulation of zero–loss filtered convergent beam electron diffraction (CBED) patterns for a* 49 *nm thick silicon crystal in* $\langle 111 \rangle$ *orientation. Top image: An enlarged version of the simulated zero–loss pattern is shown on a logarithmic scale. The structured background owing to thermal diffuse scattering is broadly visible. Bottom image: Idealized thermal–diffuse background intensity without the contribution owing to elastic scattering by the time averaged object potential.*

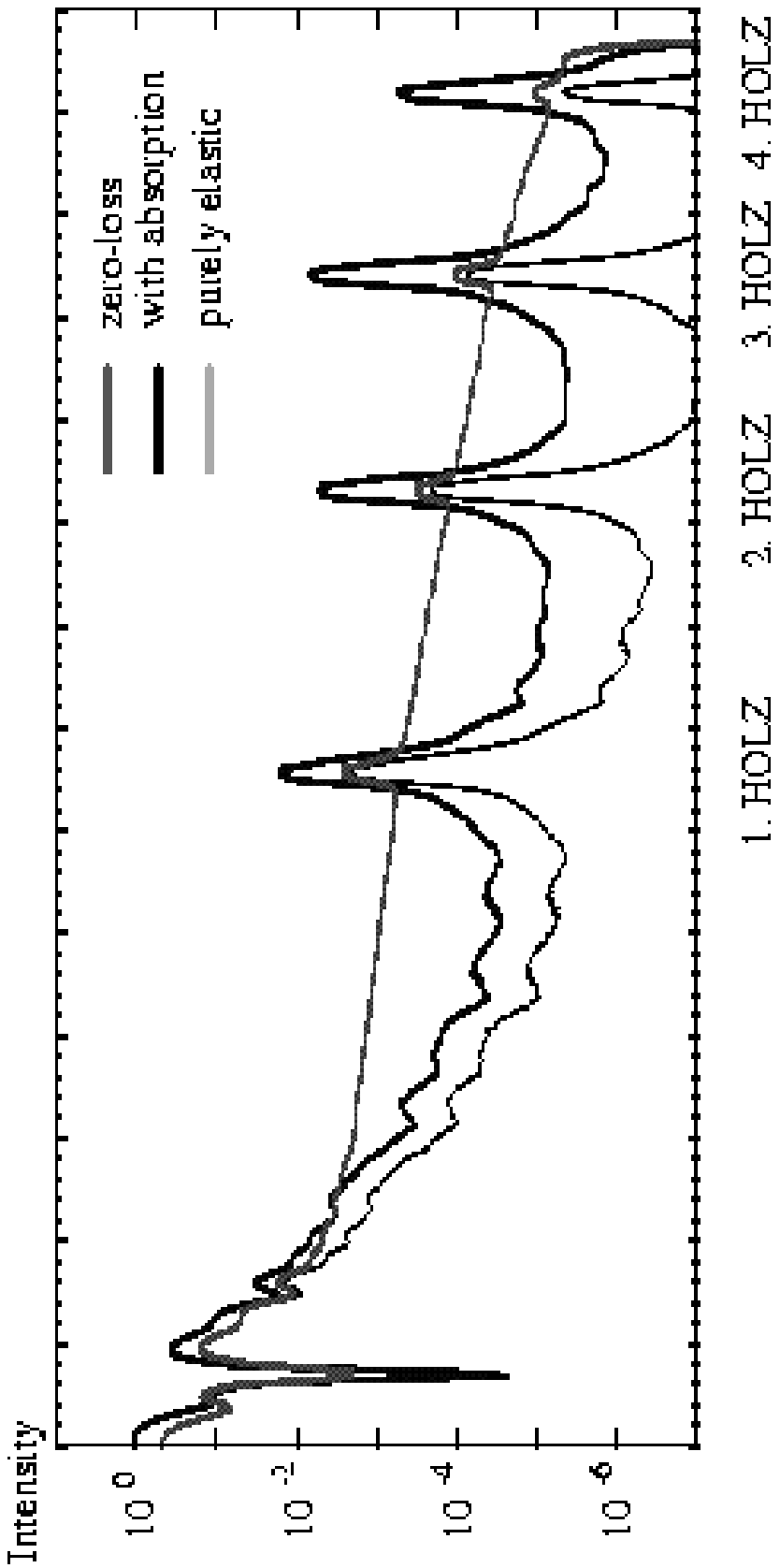

Figure 5.10: *Azimuthally integrated intensity of simulated CBED patterns. The different plots correspond to simulations obtained by the conventional multislice method with and without absorption potential and the generalized multislice method.*

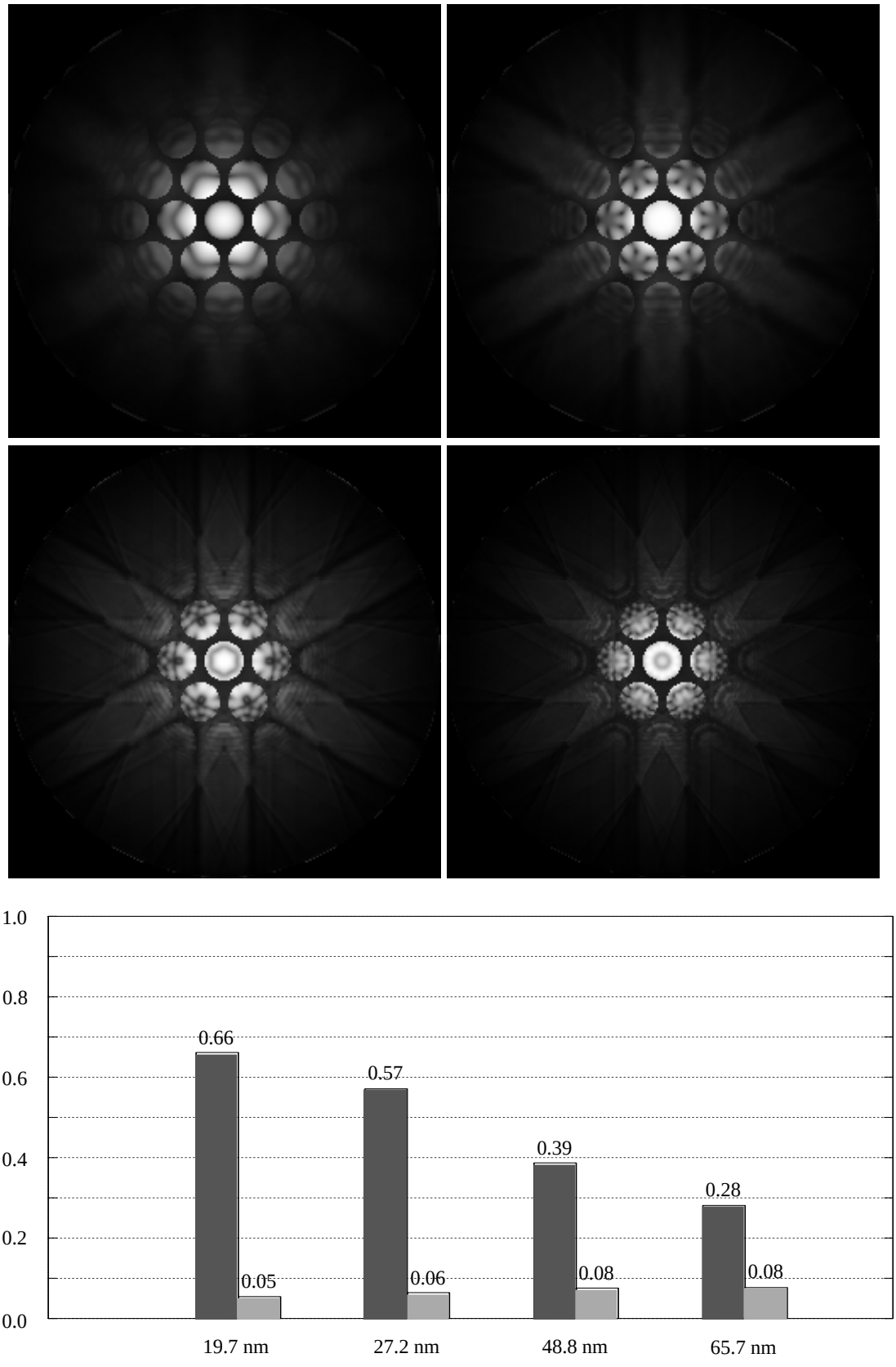

Figure 5.11: *Simulation of zero–loss filtered CBED patterns of Si* ⟨111⟩ *for different thicknesses. The integrated total intensities corresponding to elastic (left column) and thermal diffuse (right column) scattering are plotted in the histogram.*

pattern without (top left image) and with (top right image) an absorption potential for thermal diffuse scattering. The second case corresponds to a conventional multislice simulation with an absorption potential. For the view point of our theory given in chapter 4 this approximation is inconsistent with the order of magnitude of the object potential and validates the optical theorem. The left and right images at the bottom show the TDS background pattern and a zero–loss simulation accounting for elastic and thermal diffuse scattering. The investigation of the azimuthally averaged intensity plotted in figure 5.10 clearly demonstrates that the additional intensity contained in the zero–loss pattern which is not considered correctly by the conventional simulation must not be neglected in a realistic simulation. This is important for a quantitatively correct simulation on high–annular–angle darkfield STEM images where only the intensity scattered into large angles is collected by the detector. From figure 5.10 it is evident that for large scattering angles the difference between the conventional and the mutual coherence function simulation becomes significant. The ratio between the inelastic and the elastic mean free path for Silicon is approximately 1.4, hence the total intensity decreases since all electrons which have made an electronic excitation in the specimen are filtered out by the imaging energy filter. The simulation predicts, that for a thickness of about 49 nm more then 20 percent of the diffracted intensity are contained in the background.

Employing an absorption potential to account for inelastic scattering, as it has been proposed in the past [13], worsens the result and hence is totally inadequate. Inelastic scattering leads to a redistribution of the intensity in the diffraction pattern and in the image and not only to a damping of the elastic reflections as the absorption potential approach assumes. Our conclusions agree quite well with the results of the frozen phonon method [55, 11]. However, this method is less accurate, since the thermal average must be performed numerically. Accordingly, a separation of the thermal diffuse background from the elastic scattering at the time–averaged potential is not possible using this brute–force approach. Beyond this, a generalization of the frozen phonon approach to inelastic scattering due to electronic excitations is not known.

Figure 5.11 shows zero–loss filtered CBED patterns of the Si $\langle 111 \rangle$ specimen for several thicknesses. These results demonstrate that the thermal diffuse background gets more and more structured and pronounced with increasing specimen thickness. This is due to the combination of elastic multiple and TDS single scattering. The total intensity decreases due to the energy–loss scattering in combination with the energy filter.

Inelastic scattering owing to electronic excitations adds an additional background to the diffraction patterns. A comparison between the zero–loss pattern and the unfiltered pattern of Si $\langle 111 \rangle$ under CBED conditions is shown in figure 5.12. The zero beam is clearly blurred and the sharp structure in the center of the image is lost to some extend. The azimuthal average plotted in figure 5.13 illustrates that the energy–loss electrons also contribute for small scattering angles. Nevertheless, the inelastic signal contains

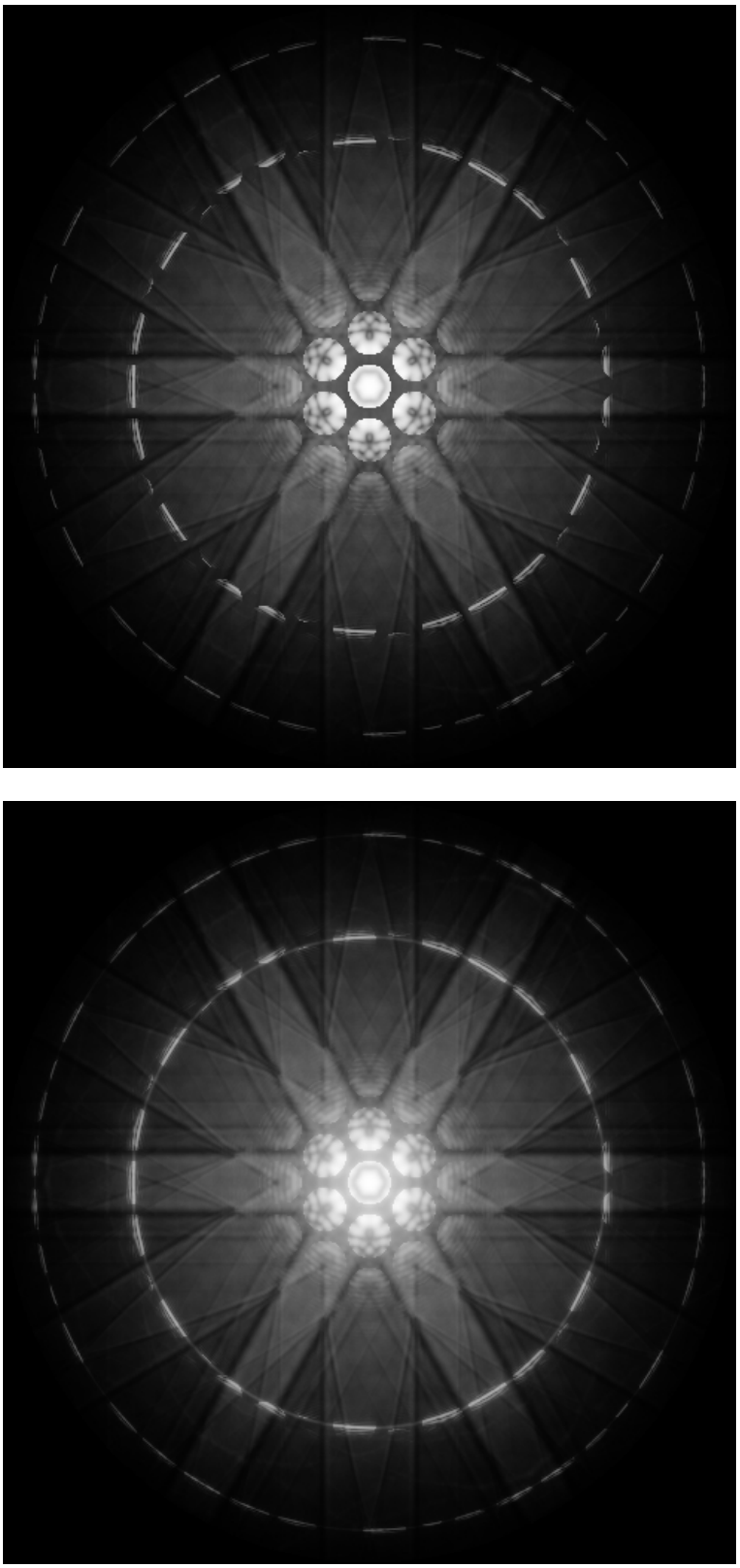

Figure 5.12: *Simulations of zero–loss (top image) and unfiltered (bottom image) convergent beam electron diffraction (CBED) patterns for a* 49 *nm thick silicon crystal in* $\langle 111 \rangle$ *orientation. A comparison between both pattern illustrates the characteristic contributions of thermal diffuse scattering and inelastic scattering owing to electronic excitations for different scattering angles.*

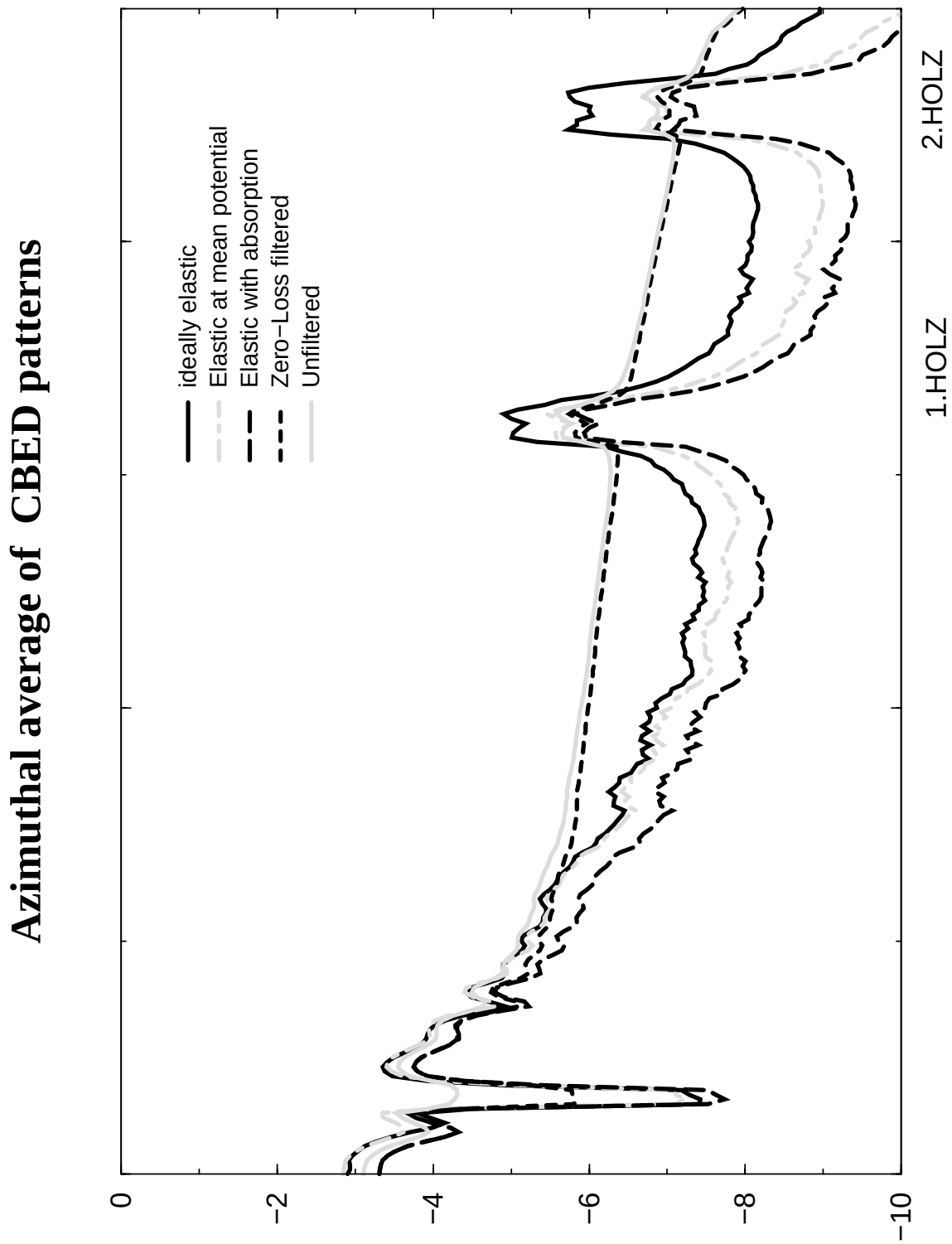

Figure 5.13: *Azimuthally integrated intensity of simulated CBED patterns. The different plots correspond to simulations obtained by the conventional multislice method with and without absorption potential and the generalized multislice method. From this presentation it becomes clear that electronic excitations effect the scattering for small and medium scattering angles, whereas thermal diffuse scattering contributes predominately to the large scattering angles.*

high–resolution spatial information. This corresponds to the difference between the zero–loss and the unfiltered intensities for large spatial frequencies in figure 5.13.

5.6 Imaging of thick objects

Inelastic scattering not only influences the diffraction pattern but also the electron micrograph. We expect the dominant effect of inelastic scattering to be the decrease of the image contrast. If the inelastic contribution were not to contain spatial information this decrease of contrast should be drastic. This is definitely not the case. We already observed several times that the image contrast with atomic resolution is almost preserved by inelastic scattering. This effect is known from experimental observations as the conservation of the elastic contrast in the inelastic image. In the following we will show that this behaviour is well reproduced by our theory. It is a consequence of mixed elastic/inelastic multiple scattering.

The diffraction pattern can be obtained from the exit wave employing the Fraunhofer approximation. To calculate the micrograph the imaging process must be considered, as we have outlined already. To illustrate the influence of inelastic scattering on the image we assume a ideal EFTEM operating at an acceleration voltage of 120 kV and an aperture of 25 mrad. Under this assumption we have calculated images corresponding to the diffraction patterns shown in the last section for of a 37.5 nm thick Silicon slab in crystallographic $\langle 111 \rangle$ orientation. For the multislice calculation on the hexagonal 512×512 grid we have used a 9×9 unit cell and 120 slices with 3 slices per unit cell. The size of the super cell is $a = b = 3.45$ nm and $c = 0.94$ nm and for the maximum scattering vector considered in the calculation we get $|\mathbf{q}_{\max}| = 46.6/$ Å. This corresponds to a maximum scattering angle of 248 mrad. Again we have used an mean atomic vibration amplitude of $u_{\mathrm{Si}} = 10.95$ pm and a mean energy loss of $\hbar\bar{\omega} = 6Z = 84$ eV. It is very important to realize that nevertheless the aperture angle of 25 mrad prevents the electrons scattered in larger angles from contributing to the image the multislice calculation must account for sufficiently large scattering angle to avoid an artificial loss of intensity during the propagation through the object. Owing to multiple scattering electrons are scattered from small to large angles and vice-verse. This behaviour is optimally illustrated by the Pendellösung in the analytical two–beam Bloch wave theory [14].

The resulting high–resolution images are shown in figure 5.14. All images clearly have atomic resolution, as we expect from the theory for ideal imaging conditions and large aperture. The thermal diffuse image, which cannot be obtained experimentally shows the characteristic doughnut–shaped structure. The intensity minimum at the positions of the atomic columns is due to the influence of the aperture. The electrons which are most affected by the thermal vibration of the atoms have passed the columns in a close vicinity of the atomic nucleis and hence are scattered with a high probability

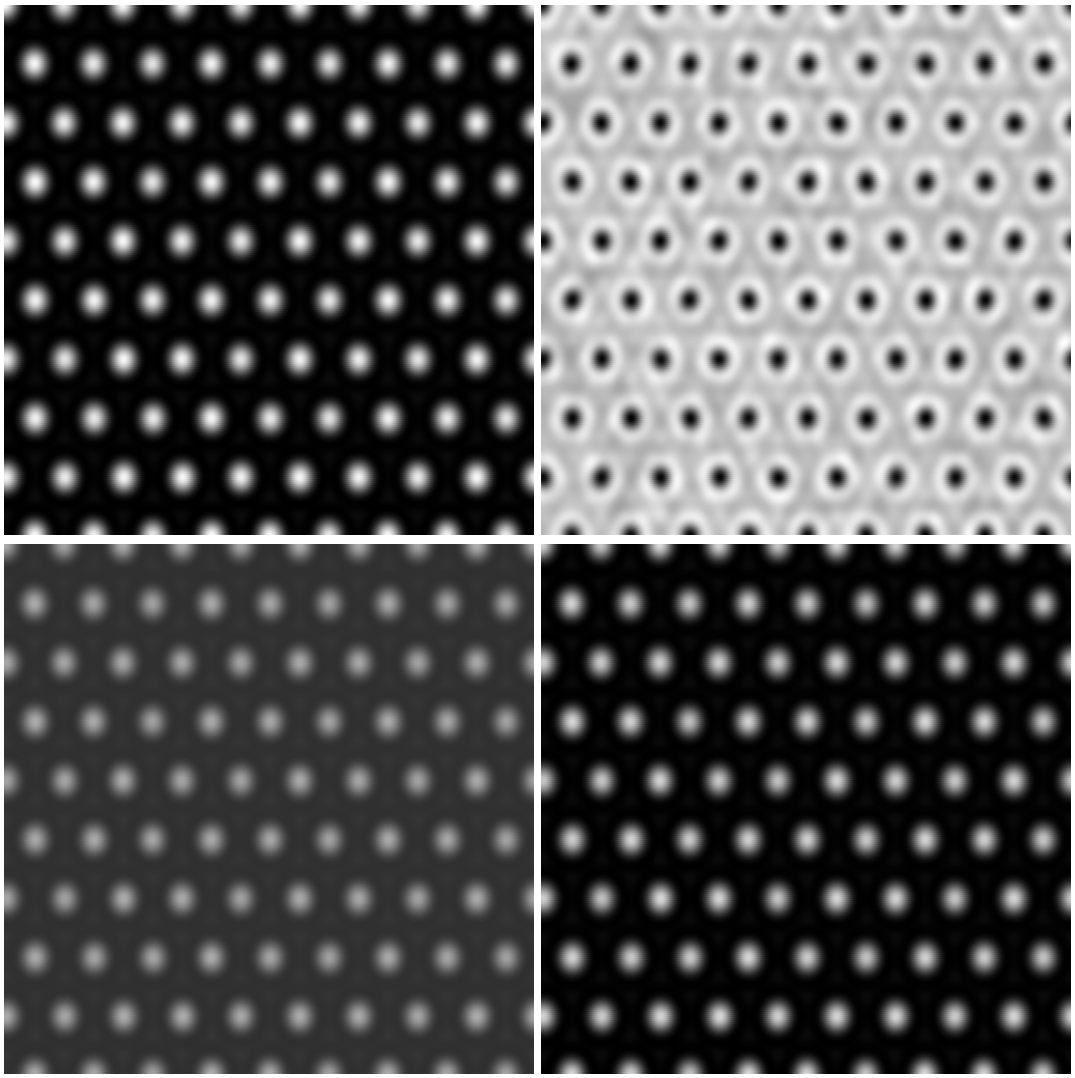

Figure 5.14: *Simulation of high–resolution images of Si in* $\langle 111 \rangle$ *orientation for a* 37.55 *nm thick silicon slab. Top left: elastic image, top right: thermal diffuse image, bottom left: energy-loss image, bottom right: unfiltered image. The unfiltered image results from a superposition of the elastic, the thermal diffuse, and the energy–loss image.*

into scattering angles larger the the aperture angle of 25 mrad. The energy–loss image is very similar to the elastic image. Only the contrast of the inelastic image is about 2.6 times lower than the contrast of the elastic image. The unfiltered image is given by the superposition of the elastic, the thermal diffuse and the energy–loss image. Accordingly, the effect of the inelastic contribution onto the contrast of the unfiltered image is small as long as the chromatic aberration of the objective lens is not taken into account. This conculsion is supported by the bottom right image in figure 5.14. For zero–loss filtered images the influence of inelastic scattering on the contrast is even smaller because in this case only the thermal diffusely scattered electrons contribute to the image.

From the point of view of high–resolution electron microscopy it seems advantageous that the image contrast of a high resolution micrograph is not heavily effected by the inelastic contribution. On the other hand the conservation of the elastic contrast has severe consequences for analytical applications in electron spectroscopy and for elemental mapping of interface structures. Since the elastic contrast is superimposed on the inelastic energy–loss image it is not always possible to relate a specific electron energy loss signal recorded at an interface to a well defined atomic location. This problem has already been addressed [56]. It should be stated that this uncertainty of the spatial origin of the spectroscopical signal is not due to the delocalization of the inelastic scattering but due to mixed elastic / inelastic multiple scattering. The same complication arises for elemental mapping with moderately thick specimens. In this case the inelastically scattered partial wave is distributed over the crystal owing to the unavoidable elastic scattering. Not only the information about the locations of the inelastic scatterers of interest is contained in the recorded energy–loss image but also the information about the spatial structure of the complete specimen. The coherence function multislice method might be well suited to contribute to these problems in the near future, when elemental mapping with atomic resolution becomes available.

Chapter 6

Conclusion

The coherence function multislice method described in the last section is a straight–forward generalization of the conventional multislice formalism. Within the context of the coherence function approach it can be used to account for the influence of partially coherent illumination and of inelastic scattering in high–resolution electron microscopy. This method provides a realistic characterization of the partially coherent process of image formation in the electron microscope. It has been demonstrated that the coherence function approach allows the extension of the frame of validity of the conventional image simulation methods considerably. Employing the coherence function multislice it is possible to describe the influence of thermal diffuse scattering and that of inelastic scattering due to electronic excitations on the degree of coherence. The most important physical aspects of the process of image formation with inelastically scattered electrons are obviously described correctly by the coherence function method. The method accounts for the linear and the quadratic contributions to the image intensity and for the non–linear relation between the scattering amplitude and the object potential in the case of thick objects. It is important to realize that apart from thin amorphous biological specimens most objects of practical importance must be considered as thick. As we have shown the generalized optical theorem of scattering theory is fulfilled by the coherence function method. This is not the case for the conventional simulation procedures as far as inelastic scattering and partial coherence are considered. Furthermore, it has been demonstrated that the conventional multislice method can be obtained from the coherence function approach as a limiting case in the absence of inelastic scattering for completely coherent illumination.

The coherence function approach provides a theoretical characterization of image formation which is consistent with the earlier formulations of Rose [26] and Rose and Kohl [7]. Furthermore, within the frame of validity of the adequately generalized high–energy approximation it is possible to calculate the transfer of the coherence function through the object numerically even for thick objects. Then the propagation process is completely determined by the first and second stochastical momenta of the time–

dependent projected potentials of the object slices. We have introduced the coherence function multislice method, which is based on a decomposition of the mutual object transparency in reciprocal space. Moreover, we have derived a mathematical procedure to obtain a suitable set of partial transmission functions required by the generalized multislice method. The form of these partial transmission functions is completely determined by the models employed to describe the dynamics of the object. For thermal diffuse scattering using the Einstein model and for electronic excitations described by the Raman–Compton approximation such sets of partial transmission functions have been calculated analytically. The feasibility of the resulting numerical method has been demonstrated and the results have been compared to experimental observations.

The results of our image simulation method clearly demonstrates that within the regime of single inelastic scattering inelastic scattering contributes high–resolution spatial information to the image. This fact has already been observed experimentally and predicted by different theoretical investigations. Unfortunately, it is still not fully accepted in the electron microscopical community. Our results based on a quite general theoretical approach should help to improve the understanding of the characteristics of the inelastic contribution to high–resolution electron micrographs and to diffraction patterns. We have developed an efficient and easy–to–use implementation of the generalized multislice method. The computer program is capable of performing TEM, STEM and CBED simulations for periodic and non–periodic specimens. The software has already been used for several investigations in the materials sciences [57] and in structural biology [59, 58].

At its current state the accuracy of our method is restricted by the numerical effort needed to evaluate the coherence function multislice procedure. To reduce this effort and to obtain numerical results within a reasonable computing time we have neglected all non local correlations of the time–dependent object potential. For thermal diffuse scattering this means that the coupling of nearest neighbour atoms due to phonon modes has been neglected. This coupling would necessitate a more complex model than the Einstein model to describe the thermal vibrations of the object correctly. Because the time of illumination in an electron microscope is very large compared to the life times of lattice excitations the Einstein model describes the overall contribution and the fundamental influence of thermal diffuse scattering quite well but fails to describe certain details of the diffraction pattern, such as streaking. The assumption that the object is composed of uncorrelated single atoms also restricts the accuracy of the computation of the inelastic contribution. Specially delocalized excitations like plasmons and the excitation of delocalized molecular orbital in biological specimens are not considered. Again, the Raman–Compton model grasps the overall influence of inelastic scattering quite well but the detailed structure of the diffraction patterns is reproduced by the simulation only to a certain extent. To investigate this in more detail accurate experiments must be performed to obtain a quantitative measure for the deviation between the experimental observations and the theoretical simulations.

The assumption that the properties of the object potential which influence the process of image formation in electron microscopy can be described completely by a superposition of potentials of single atoms is only correct to a certain extent. This conclusion is not very surprising and the further development of image simulation tools has to account for the collective phenomena more precisely. Fortunately, the effects of the collective excitations contribute predominately to the diffraction patterns and to dark field STEM imaging, where the recorded intensity directly corresponds to the integrated diffraction signal. For TEM imaging the non local effects are much less important.

For the characterization of the inelastic contribution due to electronic excitations the Raman–Compton approximation has been used. Although the Raman–Compton model reduces the complicated energy loss spectrum of the imaging electron to one single energy–loss the treatment of the chromatic aberration can be improved if a largely simplified electron–energy–loss spectrum is taken into account for the imaging process because the dominant influence of inelastic scattering on the image intensity is due to image blurring owing to the chromatic aberration of the objective lens. This more precise consideration of the chromatic aberration is of particular importance for the simulation of unfiltered images of biological specimens since inelastic scattering is the dominant scattering process for electron imaging of light atoms with atomic number below $Z \approx 20$.

Despite these restrictions the mutual coherence function method allows the treatment of image formation under partially coherent conditions including the influence of inelastic scattering from first principles. We have given definitions of the stochastical quantities μ_1, μ_2 and μ_{11} which describe the interaction between the slices of the object and the imaging electron and we have sketched how the decomposition of the mutual object transparency can be performed in general. All required information can be calculated from the fundamental models that describe the interaction process between the object and the electrons. Nevertheless, it may be more difficult to obtain these quantities for more detailed models, the coherence function approach itself does not impose any restrictions on the allowed models. Therefore, it is hoped that the coherence function multislice method method still has some potential to provide even more accurate results in the future when more powerful computers will be available. The method itself can easily be adapted to parallel computer architectures. This step surely might help to improve the results of the computer simulations in the near future.

Appendix A

Relativistically modified Schrödinger equation

The influence of the electron spin and of magnetic interaction between the scattered electron and the object on the process of image formation in electron microscopy is usually very small. Hence the time evolution of the electron wave function is described by the Klein–Gordon equation in very good approximation. This differential equation is Lorentz–invariant and, therefore, correctly accounts for the relativistic behaviour of high–energy electrons. For an electron in an electric potential $\varphi = \varphi(\mathbf{r})$ the Klein–Gordon equation has the form

$$-c^2\hbar^2\Delta\psi + m^2c^4\psi = (i\hbar\frac{\partial}{\partial t} - e\varphi)^2\psi \ . \tag{A.1}$$

In contrast to the relativistically incorrect Schrödinger equation the Klein–Gordon equation is of second order in the time derivative and, therefore, hyperbolic. To recast equation (A.1) in a Schrödinger–like form we make the local gauge transformation

$$\psi(\mathbf{r},t) \longrightarrow \mathrm{e}^{-i\frac{mc^2}{\hbar}t}\psi(\mathbf{r},t), \tag{A.2}$$

where mc^2 denotes the rest energy of the electron. After some rearrangements we obtain the result

$$\left(-\frac{\hbar^2}{2m}\Delta - \frac{e^2}{2mc^2}\varphi^2 + e\varphi\right)\psi = i\hbar\left(1 - \frac{e\varphi}{mc^2}\right)\frac{\partial}{\partial t}\Psi - i\frac{\hbar^2}{2mc^2}\frac{\partial^2}{\partial t^2}\psi \ . \tag{A.3}$$

In the non–relativistic limit $c \rightarrow \infty$ this equation is equivalent to the ordinary Schrödinger equation

$$-\frac{\hbar^2}{2m}\Delta\psi + e\varphi\psi = i\hbar\frac{\partial}{\partial t}\psi \ . \tag{A.4}$$

To solve the Klein–Gordon equation (A.3) we start with a Bernoulli product ansatz to eliminate the time dependence. The substitution

$$\psi(\mathbf{r},t) \longrightarrow \psi(\mathbf{r})\mathrm{e}^{-i\omega t} \tag{A.5}$$

yields the differential equation

$$-\frac{\hbar^2}{2m}\Delta\psi + \left(1+\frac{\hbar\omega}{mc^2}-\frac{e\varphi}{2mc^2}\right)e\varphi\psi = \hbar\omega\left(1+\frac{\hbar\omega}{2mc^2}\right)\psi \tag{A.6}$$

for the spatial part $\psi = \psi(\mathbf{r})$ of the wave function. For sufficiently weak scattering potentials $\left|\frac{e\varphi}{2mc^2}\right| \ll 1$ this equation is equivalent to the Schrödinger equation (A.4) with the real object potential multiplied by the relativistic factor $\gamma = 1 + \frac{\hbar\omega}{mc^2}$ and the modified dispersion relation

$$\hbar\omega\left(1+\frac{\hbar}{2mc^2}\right) = \frac{\hbar^2\mathbf{k}^2}{2m}\ , \tag{A.7}$$

where $\hbar\mathbf{k}$ denotes the momentum of the electron outside the range of the electric potential. Equation (A.7) corresponds to the relativistic energy–momentum relation, which relates the relativistically modified acceleration voltage U^* with the wave vector of the incident plane wave

$$\frac{\hbar^2\mathbf{k}^2}{2m} = eU\left(1+\frac{eU}{2mc^2}\right) = eU^*\ ,\ . \tag{A.8}$$

This result proves that the relativistically modified time–independent Schrödinger–equation

$$-\frac{\hbar^2}{2m}\Delta\psi + \gamma e\varphi\psi = \hbar\omega\left(1+\frac{\hbar}{2mc^2}\right)\psi \tag{A.9}$$

used in combination with the energy–momentum relation (A.8) is relativistically correct for all calculations in high–energy electron imaging and electron diffraction as long as the electron spin and the magnetic interaction are not considered.

Appendix B

Asymptotic behaviour of the scattered wave

To prove the generalized optical theorem for elastic and inelastic scattering we must evaluate the expression

$$\begin{aligned} J(\mathbf{k},\mathbf{k}') &= ir\int \mathbf{r}(\mathbf{k}+\mathbf{k}')\exp\left(-i(\mathbf{k}-\mathbf{k}')\mathbf{r}\right)\,d^2\Omega \\ &- \int f^*_{00}(\boldsymbol{\theta},\mathbf{k})\exp\left(-ik_0r+i\mathbf{k}'\mathbf{r}\right)\left(1-i\mathbf{k}'\mathbf{r}-ik_0r\right)d^2\Omega \qquad \text{(B.1)} \\ &+ \int f_{00}(\boldsymbol{\theta},\mathbf{k}')\exp\left(ik_0r-i\mathbf{k}\mathbf{r}\right)\left(1+i\mathbf{k}'\mathbf{r}+ik_0r\right)d^2\Omega \\ &+ \sum_{n=0}^{\infty}\int f_{n0}(\boldsymbol{\theta},\mathbf{k})f^*_{n0}(\boldsymbol{\theta},\mathbf{k}')\left(ik_n-\frac{1}{r}+ik_n+\frac{1}{r}\right)d^2\Omega\,. \end{aligned}$$

for arbitrary vectors $\mathbf{k}=\mathbf{k}'=k_0$ in the asymptotic limit $r\to\infty$. The integration with respect to the direction vector $\boldsymbol{\theta}=\mathbf{r}/r$ extents over the full spatial angle. The first term in equation (B.1) vanishes. Using the Gauss integral theorem we find

$$\begin{aligned} I_1 &= ir\int \mathbf{r}(\mathbf{k}+\mathbf{k}')\exp\left(-i(\mathbf{k}-\mathbf{k}')\mathbf{r}\right)\,d^2\Omega \\ &= i\int \text{div}\left((\mathbf{k}+\mathbf{k}')\mathrm{e}^{-i(\mathbf{k}-\mathbf{k}')\mathbf{r}}\right)\,d^3\mathbf{r} \qquad \text{(B.2)} \\ &= i\int(\mathbf{k}+\mathbf{k}')(\mathbf{k}-\mathbf{k}')\mathrm{e}^{-i(\mathbf{k}-\mathbf{k}')\mathbf{r}}\,d^3\mathbf{r} \;=\; 0 \qquad \text{(B.3)} \end{aligned}$$

since $|\mathbf{k}|=|\mathbf{k}'|=k_0$. The second term in (B.1) requires some more calculations. If we choose a coordinate system with one axis in $\mathbf{k}$ direction the integral

$$I_2=\int f^*_{00}(\boldsymbol{\theta},\mathbf{k})\,\mathrm{e}^{-ik_0r+\mathbf{k}\mathbf{r}}\left[1-ik_0r-\mathbf{k}\mathbf{r}\right]\,d^2\Omega\,. \qquad \text{(B.4)}$$

can be solved. In spherical polar coordinates the direction vector has the repesentation

$$\mathbf{r} = r\boldsymbol{\theta} = r \begin{pmatrix} \sin\theta\cos\phi \\ \sin\theta\sin\phi \\ \cos\theta \end{pmatrix} . \tag{B.5}$$

The scattering amplitude depends solely on the angles θ and ϕ and the integral can be rewritten as

$$I_2 = \int_0^{2\pi}\int_0^{\pi} f_{00}(\theta,\phi)\, \mathrm{e}^{-ik_0 r(1-\cos\theta)}\,[1 - ik_0 r(1+\cos\theta)]\sin\theta\; d\theta\, d\phi\; . \tag{B.6}$$

Now, we employ the transformation $u = 1 - \cos\theta$ to furtherly simplify the integration

$$I_2 = \int_0^{2\pi}\int_0^{2} f_{00}(u,\phi)\, \mathrm{e}^{-ik_0 ru}\,[1 - ik_0 r(2-u)]\; du d\phi\; . \tag{B.7}$$

For $u = 0$ the vectors $\boldsymbol{\theta}$ and $\mathbf{k}$ are parallel to each other whereas for $u = 2$ their orientation is anti–parallel. Partial integration of (B.7) with respect to u yields

$$\begin{aligned} I_2 &= \frac{1}{ik_0 r}\int_0^{2\pi}\left[f_{00}(u,\phi)\mathrm{e}^{-ik_0 ru}(1 - ik_0 r(2-u))\right]_0^2\; d\phi \\ &\quad -\frac{1}{ik_0 r}\int_0^{2\pi}\int_0^{2} \mathrm{e}^{-ik_0 ru}\frac{\partial}{\partial u}\left\{f_{00}(u,\phi)(1 - ik_0 r(2-u))\right\}\; du\, d\phi\; . \end{aligned} \tag{B.8}$$

The remaining integration of the first term can readily be performed since in this case the scattering amplitude does not depend on ϕ anymore. The second term can be simplified further by a second partial integration with respect to u. This yields

$$\begin{aligned} I_2 &= \frac{2\pi}{ik_0 r}\left[f_{00}(\mathbf{k}',\mathbf{k})(2ik_0 r - 1) - f_{00}(-\mathbf{k}',\mathbf{k})\right] \\ &+ \frac{1}{(k_0 r)^2}\int_0^{2\pi} \mathrm{e}^{-ik_0 ru}\frac{\partial}{\partial u}\left\{f_{00}(u,\phi)(1 - ik_0 r(2-u))\right\}\Big|_{u=0}^{u=2}\; d\phi \\ &- \frac{1}{(ik_0 r)^2}\int_0^{2\pi}\int_0^{2} \mathrm{e}^{-ik_0 ru}\frac{\partial^2}{\partial u^2}\left\{f_{00}(u,\phi)(1 - ik_0 r(2-u))\right\}\; du\, d\phi\; . \end{aligned} \tag{B.9}$$

Most terms in this expression vanish if we finally perform the limit $r \to \infty$ and the integral adopts the simple form

$$\lim_{r\to\infty} I_2 = 4\pi f_{00}(\mathbf{k},\mathbf{k}')\; . \tag{B.10}$$

The third integral in (B.1) can be solved using exactly the same procedure. Putting all these results together we find

$$\lim_{r\to\infty}\; J(\mathbf{k},\mathbf{k}') = 4\pi\;\left(f_{00}(\mathbf{k},\mathbf{k}') - f_{00}^*(\mathbf{k}',\mathbf{k})\right) - \sum_{n=0}^{\infty} 2ik_n \int f_{n0}(\mathbf{k},\boldsymbol{\theta}) f_{n0}^*(\mathbf{k}',\boldsymbol{\theta})\, d^2\Omega\; , \tag{B.11}$$

as stated previously in chapter 3.

Appendix C

Calculation of the mutual object spectrum

The initial mutual coherence function in front of the object has the Fourier decomposition

$$\Gamma_i(\rho,\rho',\tau) = \frac{1}{(2\pi)^2}\iiint \Gamma_i(\mathbf{q},\mathbf{q}',\omega)\mathrm{e}^{-i(\mathbf{q}\rho-\mathbf{q}'\rho')}\mathrm{e}^{i\omega\tau}\; d^2\mathbf{q}\, d^2\mathbf{q}'\, d\omega\ . \tag{C.1}$$

To calculate the mutual coherence function behind a thick object we consider only a single term of the representation. The general case of partially coherent illumination is then obtained by afterwards performing the Fourier integral in equation (C.1). The initial mutual coherence function

$$\Gamma_i(\rho,\rho',\omega) = \mathrm{e}^{-i\mathbf{q}_i(\rho-\rho')}\delta(\omega-\omega_0) \tag{C.2}$$

corresponds to tilted coherent illumination. At a plane far behind the object the asymptotic expression

$$\begin{aligned}\Gamma_{as}(\rho,\rho',\omega) \;=\;& \mathrm{e}^{-i\mathbf{q}_i(\rho-\rho')}\delta(\omega-\omega_0) \\ &+\frac{1}{z}\mathrm{e}^{-i\mathbf{q}_i\rho}\mathrm{e}^{i\frac{z}{2k}\mathbf{q}_i^2} f_{00}(\frac{k}{z}\rho',\mathbf{q}_i)\mathrm{e}^{i\frac{k}{2z}\rho'^2}\delta(\omega-\omega_0) \\ &+\frac{1}{z}\mathrm{e}^{i\mathbf{q}_i\rho'}\mathrm{e}^{-i\frac{z}{2k}\mathbf{q}_i^2} f^*_{00}(\frac{k}{z}\rho,\mathbf{q}_i)\mathrm{e}^{-i\frac{k}{2z}\rho^2}\delta(\omega-\omega_0) \\ &+\frac{1}{z^2}\sum_{n=0}^{\infty} f^*_{n0}(\frac{k}{z}\rho,\mathbf{q}_i) f_{n0}(\frac{k}{z}\rho',\mathbf{q}_i)\mathrm{e}^{-i\frac{k}{2z}(\rho^2-\rho'^2)}\delta(\omega-\omega_n)\end{aligned} \tag{C.3}$$

holds true. This result is a direct consequence of the definition of the scattering amplitude. We have used the Fresnel approximation for the spherical waves. For the asymptotic domain this approximation is exact. Since inelastic scattering events are considered the modulus of the wave vector, $k = k(\omega)$, is a function of the energy

loss. The resulting asymptotic expression (C.3) is related to the final mutual coherence function in the object plane $\Gamma_O = \Gamma_O(\rho_O, \rho'_O, \omega)$ via a four–dimensional Fresnel propagation

$$\Gamma_{as}(\rho, \rho', \omega) = \left(\frac{k}{2\pi z}\right)^2 \int \Gamma_O(\rho_O, \rho'_O, \omega) \mathrm{e}^{-i\frac{k}{2z}\left[(\rho-\rho_O)^2-(\rho'-\rho'_O)^2\right]}\, d^2\rho_O\, d^2\rho'_O\,. \tag{C.4}$$

We can perform the Fourier transformation of this expression with respect to the lateral coordinates ρ and ρ' analytically. In particular we find

$$\begin{aligned}
\Gamma_{as}(\mathbf{q}, \mathbf{q}', \omega) &= \frac{1}{(2\pi)^2}\left(\frac{k}{2\pi z}\right)^2 \iint \Gamma_O(\rho_O, \rho'_O, \omega)\, \mathrm{e}^{-i\frac{k}{2z}\left[(\rho-\rho_O)^2-(\rho'-\rho'_O)^2\right]} \\
&\qquad \times \mathrm{e}^{i\rho\mathbf{q}-i\rho'\mathbf{q}'}\, d^2\rho_O\, d^2\rho'_O\, d^2\rho\, d^2\rho' \qquad \text{(C.5)} \\
&= \frac{1}{(2\pi)^2}\left(\frac{k}{2\pi z}\right)^2 \mathrm{e}^{i\frac{z}{2k}(\mathbf{q}^2-\mathbf{q}'^2)} \int \Gamma_O(\rho_O, \rho'_O, \omega) \\
&\qquad \times \mathrm{e}^{i\mathbf{q}\rho_O-i\mathbf{q}'\rho'_O}\, d^2\rho_O\, \rho'_O \int \mathrm{e}^{-i\frac{k}{2z}(\rho^2-\rho'^2)}\, d^2\rho\, d^2\rho' \\
&= \mathrm{e}^{i\frac{z}{2k}(\mathbf{q}^2-\mathbf{q}'^2)}\, \Gamma_O(\mathbf{q}, \mathbf{q}', \omega)\,, \qquad \text{(C.6)}
\end{aligned}$$

where a Gaussian integral has been evaluated to obtain the last equation. Even for the Fourier transform of the expression (C.3) we can derive an analytic form. Some rearrangements and the substitutions $\mathbf{q}'' = \frac{k}{z}\rho$ and $\mathbf{q}''' = \frac{k}{z}\rho'$ yield

$$\begin{aligned}
\Gamma_{as}(\mathbf{q}, \mathbf{q}', \omega) &= \frac{1}{(2\pi)^2}\int \mathrm{e}^{-i\mathbf{q}_i(\rho-\rho')}\mathrm{e}^{i\mathbf{q}\rho-i\mathbf{q}'\rho'}\, d^2\rho\, d^2\rho'\, \delta(\omega-\omega_0) \qquad \text{(C.7)} \\
&\quad + \frac{1}{(2\pi)^2}\int \frac{1}{z}\mathrm{e}^{-i\mathbf{q}_i\rho}\mathrm{e}^{i\frac{z}{2k}\mathbf{q}_i^2} f_{00}(\frac{k}{z}\rho', \mathbf{q}_i)\mathrm{e}^{i\frac{k}{2z}\rho'^2}\mathrm{e}^{i\mathbf{q}\rho-i\mathbf{q}'\rho'}\, d^2\rho\, d^2\rho'\, \delta(\omega-\omega_0) \\
&\quad + \frac{1}{(2\pi)^2}\int \frac{1}{z}\mathrm{e}^{i\mathbf{q}_i\rho'}\mathrm{e}^{-i\frac{z}{2k}\mathbf{q}_i^2} f^*_{00}(\frac{k}{z}\rho, \mathbf{q}_i)\mathrm{e}^{-i\frac{k}{2z}\rho^2}\mathrm{e}^{i\mathbf{q}\rho-i\mathbf{q}'\rho'}\, d^2\rho\, d^2\rho'\, \delta(\omega-\omega_0) \\
&\quad + \frac{1}{(2\pi)^2}\int \frac{1}{z^2}\sum_{n=0}^{\infty} f^*_{n0}(\frac{k}{z}\rho, \mathbf{q}_i) f_{n0}(\frac{k}{z}\rho', \mathbf{q}_i) \\
&\qquad \times \mathrm{e}^{-i\frac{k}{2z}(\rho^2-\rho'^2)}\mathrm{e}^{i\mathbf{q}\rho-i\mathbf{q}'\rho'}\, d^2\rho\, d^2\rho'\, \delta(\omega-\omega_n) \\
&= \delta^2(\mathbf{q}-\mathbf{q}_i)\delta^2(\mathbf{q}'-\mathbf{q}_i)\delta(\omega-\omega_0) \\
&\quad + \frac{z}{(2\pi k)^2}\, \mathrm{e}^{i\frac{z}{2k}\mathbf{q}^2}\delta^2(\mathbf{q}-\mathbf{q}_i)\int f_{00}(\mathbf{q}'', \mathbf{q}_i)\mathrm{e}^{i\frac{z}{2k}\mathbf{q}''^2-i\frac{z}{k}\mathbf{q}'\mathbf{q}''}\, d^2\mathbf{q}''\delta(\omega-\omega_0) \\
&\quad + \frac{z}{(2\pi k)^2}\mathrm{e}^{-i\frac{z}{2k}\mathbf{q}'^2}\delta^2(\mathbf{q}'-\mathbf{q}_i)\int f^*_{00}(\mathbf{q}''', \mathbf{q}_i)\mathrm{e}^{-i\frac{z}{2k}\mathbf{q}'''^2+i\frac{z}{k}\mathbf{q}'\mathbf{q}'''}\, d^2\mathbf{q}'''\delta(\omega-\omega_0) \\
&\quad + \frac{1}{(2\pi)^2}\frac{z^2}{k^4}\sum_{n=0}^{\infty}\int f^*_{n0}(\mathbf{q}'', \mathbf{q}_i) f_{n0}(\mathbf{q}''', \mathbf{q}_i) \\
&\qquad \times \mathrm{e}^{-i\frac{z}{2k}\mathbf{q}''^2+i\frac{z}{k}\mathbf{q}\mathbf{q}''}\mathrm{e}^{i\frac{z}{2k}\mathbf{q}'''^2-i\frac{z}{k}\mathbf{q}'\mathbf{q}'''}\, d^2\mathbf{q}''\, d^2\mathbf{q}'''\, \delta(\omega-\omega_n)\,.
\end{aligned}$$

To evaluate the terms involving the scattering amplitude we have to consider the identity

$$\lim_{z\to\infty}\frac{z}{(2\pi k)^2}\int\int f_{n0}(\mathbf{q}'',\mathbf{q}_i)\;\mathrm{e}^{i\frac{z}{2k}(\mathbf{q}''-\mathbf{q}')^2}\;d^2\mathbf{q}''=\frac{i}{2\pi k}f_{n0}(\mathbf{q}',\mathbf{q}_i) \tag{C.8}$$

which is equivalent to the statement that the Fresnel propagator degenerates to a delta function for an infinitesimal distance of propagation. Hence in the asymptotic limit we can equate relation (C.5) and (C.7) and finally solve for the Fourier transform of the mutual coherence function in the object plane

$$\begin{aligned}\Gamma_O(\mathbf{q}_O,\mathbf{q'}_O,\omega) &= \delta^2(\mathbf{q}-\mathbf{q}_i)\delta^2(\mathbf{q}'-\mathbf{q}_i)\delta(\omega-\omega_0) \\ &+\frac{1}{2\pi ik}\delta^2(\mathbf{q}-\mathbf{q}_i)f_{00}(\mathbf{q}',\mathbf{q}_i)\delta(\omega-\omega_0) \\ &-\frac{1}{2\pi ik}\delta^2(\mathbf{q}'-\mathbf{q}_i)f^*_{00}(\mathbf{q},\mathbf{q}_i)\delta(\omega-\omega_0) \\ &+\frac{1}{(2\pi k)^2}\sum_{n=0}^{\infty}f^*_{n0}(\mathbf{q},\mathbf{q}_i)f_{n0}(\mathbf{q}',\mathbf{q}_i)\delta(\omega-\omega_n)\;.\end{aligned} \tag{C.9}$$

This result proves the relation stated in chapter 4.

Bibliography

[1] H. Müller and P. Schorsch, The YaMS Manual, Institute of Applied Physics, TU Darmstadt, unpublished. 2

[2] L. Reimer (1995), Energy–filtering Transmission Electron Microscopy, Springer, New York. 5, 6, 28, 34, 50

[3] P. Hartel, H. Rose and C. Dinges (1996) Conditions and Reasons for Incoherent Imaging in STEM, Ultramicroscopy 63: 93 - 114. 5

[4] L.D. Landau, E.M. Lifschitz (1979) Lehrbuch der theoretischen Physik Vol. 3, Akademie Verlag, Berlin. 5, 22, 27, 50

[5] J.J. Sakurai (1985) Modern Quantum Mechanics, Addison–Wesley, New York: 325–326. 5, 50, 57

[6] R.J. Glauber (1959) High–Energy Collision Theory. In: Lectures in Theoretical Physics, Boulder Vol.1, Interscience, New York: 315–414. 5, 8, 23, 55

[7] H. Kohl and H. Rose (1985) Theory of Image Formation by Inelastically Scattered Electrons in the Electron Microscope. In: Advances in Electronics and Electron Physics, Vol.65, Academic Press, Orlando: 173–227. 6, 7, 8, 9, 22, 33, 49, 49, 99

[8] H. Rose (1984) Information Transfer in Transmission Electron Microscopy, Ultramicroscopy 15: 173–192. 6, 7, 9, 26, 27, 44, 49, 49, 51, 55, 61, 62

[9] C. Dinges, A. Berger and H. Rose (1995) Simulation of TEM and STEM Images Considering Phonon and Electronic Excitations, Ultramicroscopy 6: 49–70. 6, 35, 56, 61, 72, 74, 75

[10] H. Müller, H. Rose, P. Schorsch (1998) A Coherence Function Approach to Image Simulation, J. Micr. 190: 73–88. 6, 56, 59, 60, 61, 64, 66, 73, 74, 75, 76, 79

[11] E.J. Kirkland (1998) Advanced Computing in Electron Microscopy, Plenum Press, New York: 99–129. 6, 7, 60, 61, 82, 82, 93

[12] L. Reimer (1992) Transmission Electron Microscopy, Springer, Berlin. 6

[13] J.C.H. Spence, J.M. Zuo (1982) Electron Microdiffraction, Plenum Press, New York. 6, 93

[14] H. Bethe (1938) Theorie der Beugung von Elektronen an Kristallen, Ann. Phys. 87: 55–129. 7, 96

[15] A.J.F. Metherell (1975) In: Electron Microscopy in Materials Science (U. Valdre and E. Ruedl, Eds.), Vol. 2, 297. 7

[16] L.J. Allen and C.J. Rossouw (1993) Phys. Rev. B **47**, 6673. 7

[17] J.M. Cowley and A.F. Moodie (1957) The Scattering of Electrons by Atoms and Crystalls. Acta Cryst. 10: 609–619. 7, 60

[18] M. Read and B. Simon (1975) Methods of Modern Mathematical Physics, Vol. 1+2, Academic Press, Orlando. 7

[19] R.P. Feynmann and A.R. Hibbs (1965), Quantum Mechanics and Path Integrals, McGraw–Hill, New York. 7

[20] P.A. Stadelmann (1987) EMS - A Software Package for Electron Diffraction Analysis and HREM Image Simulation in Materials Science. Ultramicroscopy 21: 131–146. 7, 60

[21] M.A. O'Keefe and P.R. Buseck (1979) Computation of high–resolution TEM images of materials. Trans. Am. Cryst. Assoc., 15: 27–46. 7

[22] K. Ishizuka (1980) Contrast transfer of crystal images in TEM, Ultramicroscopy 5: 55–65. 7

[23] M. Haider, S. Uhlemann, E. Schwan, H. Rose, B. Kabius, and K. Urban (1998), Electron microscopy image enhanced, Nature 392: 768-769. 7, 12

[24] H. Rose (1999) Prospects for realizing a sub–Åsub–eV resolution EFTEM, Ultramicroscopy 78: 13–25. 7

[25] G. Möbus (2000) In: High–Resolution Imaging and Spectrometry of Materials (M. Rühle and F. Ernst, Eds.), Springer, Heidelberg, in press. 7

[26] H. Rose (1976) Image Formation by Inelastically Scattered Electrons in Electron Microscopy. Optik 45: 139–158. 7, 8, 30, 34, 35, 37, 49, 50, 52, 66, 72, 99

[27] D. van Dyck (1985) Image calculation in high–resolution electron microscopy: Problems, progress, and prospects. In: Advances in Electronics and Electron Physics (P.W. Hawkes, Ed.), Academic Press, Orlando. 8

[28] P.W. Hawkes (1978) Coherence in Electron Optics. In: Advances in Optical and Electron Microscopy, Vol.7, Academic Press, Orlando: 101–184. 8, 37

[29] W. Glaser (1952), Grundlagen der Elektronenoptik, Springer, Wien. 14

[30] C. Kittel (1996) Introduction to Solid State Physics, Wiley, New York. 15, 72

[31] H. Yoshioka, (1957), J. Phys. Soc. Japan 12: 618. 16

[32] B.A. Lippmann, J. Schwinger (1940) Variational Principles for Scattering Processes, Phys. Rev. 79: 469–480. 17

[33] J.W. Goodman (1996) Introduction to Fourier Optics, McGraw–Hill, New York: 63–95. 20, 42, 76, 77, 78, 78

[34] R.G. Newton (1989), Inverse Schrödinger Scattering in Three Dimensions. Springer, New York. 21

[35] M. Born and E. Wolf (1975), Principles of Optics, Pergamon Press, Oxford. 21, 39, 40, 42, 76

[36] F. Lenz (1957) Zur Streuung mittelschneller Elektronen in kleinste Winkel. Z. Naturf. 9a (1957), 185–204. 27, 34, 72

[37] H.Koppe (1948) Der Streuquerschnitt von Atomen für unelastische Streuung von schnellen Elektronen, Z. Physik 124: 658–664. 30, 33

[38] N.F. Mott (1930) The Scattering of Electrons by Atoms, Proc. Royal Society A 127: 658–665. 30

[39] P.A. Doyle and P.S. Turner (1968), Relativistic Hartree-Fock X-ray and Electron Scattering Factors, Acta Cryst. A 24: 390–397. 31, 31

[40] A. Weickenmeier and H. Kohl (1991) Computation of Absorptive Form Factors for High–Energy Electron Diffraction, Acta Cryst. A 47: 590–603. 32, 61, 72

[41] R. Eusemann, H. Rose, J. Dubochet (1982) Electron Scattering in Ice and Organic Materials, J. Micr. 128: 239–249. 33

[42] A.H. Compton (1930) The Determination of Electron Distributions from Measurements of X-Rays, Phys. Rev. 35: 925–938. 33, 72

[43] J. Fertig and H. Rose (1977) A Reflection on Partial Coherence in Electron Microscopy, Ultramicroscopy 2A: 269–279. 37

[44] L.van Hove (1954) Correlations in Space and Time and Born Approximation Scattering in Systems of Interacting Particles, Phys. Rev. 95: 249–262. 51

[45] P.G. Self, M.A. O'Keefe, P.R. Buseck and A.E.C. Spargo (1983) Practical Computation of Amplitudes and Phases in Electron Diffraction, Ultramicroscopy 11: 35–52. 60

[46] C.W. Gardiner (1997) Handbook of Stochastic Methods, Springer, Berlin. 63, 63

[47] K. Ishizuka and N. Uyeda (1977) A new theoretical and practical approach to the multislice method, Acta Cryst. A33: 740–749. 71, 82

[48] E.O. Brigham (1974) The Fast Fourier Transform, Prentice Hall, New Nork. 71

[49] M. Frigo and S.G. Johnson (1998) FFTW: An adaptive software architecture for the FFT. In: Proc. of the IEEE Internat. Conf. on Acoustics, Speech, and Signal Processing, Vol. 3, Seattle. 71

[50] M. Abramowitz and I.A. Stegun (1970) Handbook of Mathematical Functions. Dover Publications, New York. 73, 79

[51] C.C. Ahn and O.L. Krivanek (1983) EELS Atlas. Center for Solid State Science, Arizona State University. 74

[52] P.W. Hawkes and E. Kasper (1989) Principles of Electron Optics. Vol. 1+2, Academic Press, San Diego. 76

[53] O. Scherzer (1949) The theoretical resolution limit of the electron microscope, J. Applied Physics 20: 20–29. 88

[54] H. Rose (2000) In: High–Resolution Imaging and Spectrometry of Materials (M. Rühle and F. Ernst, Eds.), Springer, Heidelberg, in press. 76, 77

[55] R.F. Loane, P. Xu, J. Silcox (1991) Thermal Vibrations in Convergent–Beam Electron Diffraction. Acta Cryst. A 47: 267–278. 93

[56] P. Stallknecht (1997) Simulation der Kontrastentstehung bei hoch aufgelösten elektronenmikroskopischen Elementverteilungsbildern von orientierten Kristallen, Dissertation, Univ. Münster. 98

[57] H. Müller and H. Rose (1998) A Coherence Function Approach to Image Simulation, Proc. of ICEM 14, Cancun, Mexico. 100

[58] O. Vossen, H. Müller, P. Schorsch, and R.R. Schroeder (2000) Proc. of EUREM 12, Brno, Czech Republic, *submitted*. 100

[59] E. Rietzel, H. Müller, P. Schorsch, and R.R. Schroeder (1998) Proc. of ICEM 14, Cancun, Mexico. 100

Zusammenfassung

Eine direkte Interpretation von hochaufgelösten elektronenmikroskopischen Bildern ist aufgrund der stark nichtlinearen Beziehung zwischen dem inneren elektrischen Potential der Probe, und damit der atomaren Struktur des Objekts, und der aufgezeichneten Intensitätsverteilung im Bild nur in Ausnahmefällen möglich. In der Vergangenheit sind daher Verfahren entwickelt worden, die die Berechnung von elektronenmikroskopischen Bildern und Beugungsbildern bei bekannter atomarer Struktur des Objekts ermöglichen. Mit Hilfe von Simulationsrechnungen wird so eine verlässliche Interpretation von HREM Bildern möglich. Das am universellsten einsetzbare Bildsimulationsverfahren ist das Multislice–Verfahren von Cowley und Moodie. Es erlaubt im Rahmen der Gültigkeit der Hochenergienäherung auch für dicke Objekte die Wechselwirkung zwischen abbildenden Elektronen und Objekt iterativ zu beschreiben. Bei der Anwendung dieses Verfahrens wird jedoch vorausgesetzt, dass das Objekt kohärent beleuchtet wird und keine inneren Freiheitsgrade besitzt. Die Simulation erfasst daher nur den Beitrag der elastisch gestreuten Elektronen zum Bild und Beugungsbild. Der Einfluss unelastischer Streuprozesse und partieller Kohärenz des abbildenden Elektronenwellenfelds bleiben unberücksichtigt. In einem realen Mikroskop ist aber schon die Beleuchtung niemals ideal kohärent und die unelastischen mittleren freien Weglängen für Elektronen im Energiebereich von 60 kV bis 300 kV haben die gleiche Größenordnung wie die für elastische Streuung. Für leichte Atome, wie sie in biologischen Präparaten häufig vorkommen, sind die unelastischen Wirkungsquerschnitte sogar ungefähr doppelt so groß wie die elastischen Wirkungsquerschnitte.

Da sich die Auflösung von Transmissionselektronenmikroskopen in den letzten Jahren entscheidend verbessert hat und die quantitative Auswertung von elektronenmikroskopischen Daten immer mehr an Bedeutung gewinnt, besteht Bedarf, Bildsimulationsverfahren zu entwickeln, welche eine realistischere Beschreibung der Bildentstehung unter Einbeziehung partieller Kohärenz und unelastischer Streuung ermöglichen. In der vorliegenden Arbeit wird daher untersucht, wie sich der bekannte Formalismus zur Beschreibung der Bildentstehung im Elektronenmikroskop erweitern lässt, um diese Effekte in guter Näherung berücksichtigen zu können. Es zeigt sich dabei, dass zur Berücksichtigung der unelastischen Streuung ein Verfahren verwendet werden muss, das das verallgemeinerte optische Theorem der Streutheorie erfüllt. Diese Eigenschaft ist notwendig, um die Verkopplung zwischen unelastischer und elastischer Streuung korrekt zu beschreiben. Mit Hilfe der gemischten Kohärenzfunktion lässt sich der Abbildungsvorgang im Elektronenmikroskop unter korrekter Berücksichtigung der partiellen Kohärenz zwischen den unterschiedlichen Streuwellen beschreiben. Die Wirkung des Objekts auf die gemischte Kohärenzfunktion wird für allgemeine Objekte durch das gemischte Objektspektrum erfasst. Der bezüglich der Streuamplituden quadratische Anteil des gemischten Objektspektrums lässt sich im Fall dünner Objekte in erster Bornscher Näherung durch den gemischt–dynamischen Formfaktor ausdrücken, der von Rose und Kohl erstmal

zur Beschreibung der Bildentstehung im Elektronenmikroskop eingeführt wurde.

Diese Arbeit befaßt sich mit der Behandlung dicker Objekte, für die weder die erste Bornsche Näherung noch die Phasenobjektnäherung gültig sind. Mit Hilfe einer geeigneten Verallgemeinerung der Glauberschen Hochenergienäherung auf Objekte mit inneren Freiheitsgraden ist es möglich eine dem Multislice–Verfahren ähnliche Methode zur Bildsimulation herzuleiten, die auf der Propagation der gemischten Kohärenzfunktion durch das Objekt und das Mikroskop beruht. Dieses Verfahren wird begründet und seine Anwendbarkeit wird diskutiert. Um praktische Rechnungen für realistische Objekte durchführen zu können, sind weitere Näherungsannahmen notwendig. Diese werden begründet. Das resultierende numerische Verfahren ermöglicht die Berechnung von elektronenmikroskopischen Diffraktionsbildern und Hochauflösungsbildern unter Berücksichtigung unelastischer Streuprozesse und der mit diesen verbundenen partiellen Kohärenz. Die unelastische Wechselwirkung zwischen den abbildenden Elektronen und dem atomaren Gitter (thermisch diffuse Streuung) sowie der elektronischen Ladungsdichte (elektronische Anregungen) des Objekts wird durch einfache Modelle beschrieben, die kollektive Effekte im Objekt vernachlässigen. Trotz dieser einfachen Modellannahme ergeben sich für die berechneten Diffraktionsbilder realistische Resultate. Die wesentlichen Charakteristika ungefilterter und zero–loss gefilterter Beugungsbilder werden sehr gut reproduziert, wie der visuelle Vergleich der Simulationen mit experimentellen Bildern bestätigt. Zur Berechnung von Hochauflösungsbildern müssen die optischen Eigenschaften des Transmissionsmikroskops und das Informationslimit des Instruments in der Simulation berücksichtigt werden. Es wird gezeigt, dass dies im Rahmen des Kohärenzfunktion–Multislice–Verfahrens erreicht werden kann. Dazu muss die Wirkung des Beleuchtungs– und des Abbildungssystems auf die gemischte Kohärenzfunktion beschrieben werden.

Das entwickelte Kohärenzfunktion–Multislice–Verfahren ist als Fortran Programmpaket implementiert und ermöglicht die Simulation von ungefilterten und zero-loss gefilterten Bildern allgemeiner periodischer und nicht periodischer Objekte im Ruhbild– (TEM/Abbildung) und Rasterbetrieb (STEM) und von Beugungsbildern bei paralleler (TEM/Diffraktion) und konvergenter (CBED) Beleuchtung. Das Bildsimulationsprogramm wird für Untersuchungen im Bereich der Materialwissenschaften und der Strukturbiologie eingesetzt.

THE CASE OF THE LOST ELECTRONS

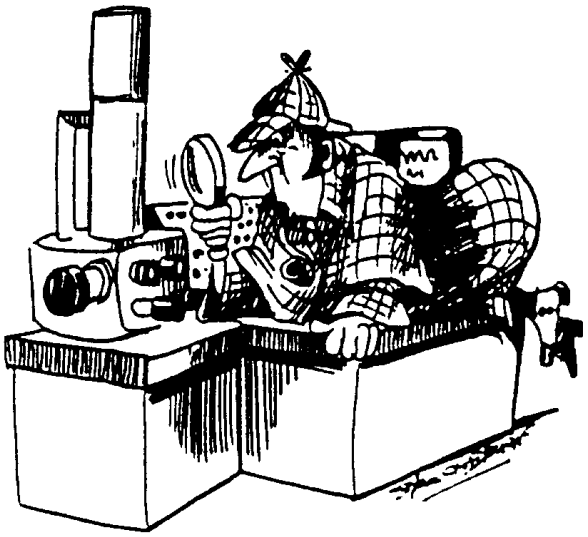

Acknowledgement

I am very grateful to Prof. Dr. Harald Rose who initiated this work. His sustained interest and his great support during my time at the light and partical optics group at Darmstadt University was crucial for the success of this work. Many thanks to my collegues Dipl. Phys. Volker Gerheim, Dipl. Phys. Peter Hartel, Dr. Frank Kahl, Dr. Dirk Preikszas, Dipl. Phys. Peter Schmid, and Dipl. Phys. Peter Schorsch for many helpful discussions and support and especially to Dr. Rainer Spehr, and Dipl. Phys. Christoph Weißbäcker for proof reading my manuscript and asking many important questions.

Financial support by the 'Volkswagen Stiftung' and the 'Deutsche Gesellschaft für Elektronenmikroskopie' is greatfully acknowledged.

I am thankful to Dr. Rasmus Schröder (MPI for Medical Research, Heidelberg) and his coworkers Dipl. Ing. Petra Behle, Dr. Eike Ritzel, and especially to Dipl. Phys. Oliver Vossen for improving my english, to Dr. Günter Möbus (Oxford University) for many discussions about illumination conditions and STEM multislice simulation, to Dr. Peter Schwander and Dr. Wolf–Dieter Rau (Institut of Semiconductor Physics, Frankfurt/Oder) for their cooperation and their attempts to improve my insufficient knowledge about experimental electron microscopy, to Dr. Rainer Ochs and Dipl. Ing. Rüdiger Künzler (DIBIS AG, Birkenfeld) for placing their imaging plate scanner at our disposal, to Prof. Dr. Hannes Lichte (TU Dresden) for many discussions about coherence and inelastic scattering and finally to all the others I have not mentioned explicitely, who helped me to work out the mysterious case of the lost electrons.

Lebenslauf

Persönliche Daten:

Name:	Heiko Müller
Geburtsdatum:	05. 05. 1970
Geburtsort:	Kassel
Familienstand:	ledig, 1 Kind
Staatsangehörigkeit:	deutsch

Ausbildung:

1976 – 1980	Grundschule in Naumburg / Hessen
1980 – 1989	König–Heinrich–Schule in Fritzlar
Mai 1989	Abitur
1989 – 1990	Grundwehrdienst
1990 – 1996	Studium an der TU Darmstadt
	Vordiplom Physik
	Vordiplom Mathematik
Februar 1996	Diplom Physik
	Diplomarbeit: “Konstruktion eines semianalytischen Feldberechnungsverfahrens und Anwendung auf einen fehlerarmen Strahlteiler”
	Betreuer: Prof. Dr. H. Rose
seit März 1996	Wissenschaftlicher Mitarbeiter am Institut für Angewandte Physik der TU Darmstadt

Darmstadt, den 17. April 2000